Fine Structure in the Alpha Decay of ^{192}Po: Shape Coexistence in ^{188}Pb

Thesis submitted in accordance with the requirements of the
University of Liverpool for the degree of Doctor in Philosophy

by

Roger Giles Allatt

Oliver Lodge Laboratory

September 1998

This thesis is dedicated to my Mum and Dad.

Abstract

Two excited $J^{\pi} = 0^{+}$ states have been established in the nuclide ^{188}Pb. The states were populated in the α decay of ^{192}Po in an experiment performed at the University of Jyväskylä, Finland. A novel technique to select the decay to the states of interest by their conversion electron signal was devised and implemented in the form of a silicon detector array mounted around the existing focal plane detector of the RITU spectrometer. The α-particle energies and half-lives have been measured, together with the branching ratios, to each level so that reduced hindrance factors may be deduced.

The $J^{\pi} = 0^{+}$ states lie close in energy and are based upon proton pair excitations across the closed Z=82 shell. The coexisting structures are attributed to spherical, oblate and prolate minima in the potential energy surface. Mixing matrix elements, mixing amplitudes and the energies of unperturbed and unobserved levels have been estimated in terms of configuration mixing calculations.

Acknowledgements

- Professor P.J. Twin OBE FRS, for allowing me to carry out this research at the University of Liverpool.
- Dr R.D. Page for his source of ideas and his helpful supervision.
- Professor R. Julin, Professor M. Leino and all of the staff at the University of Jyväskylä for providing the excellent facilities and support without which this work would not have been possible. Thanks especially to Dr Juha Uusitalo, the RITU expert, and Dr Pete Jones for ensuring that the TARDIS data acquisition system acquired data.
- Dr J.F.C. Cocks and Paul Greenlees for their assistance and skilled vacuum pump operation, on the experiment.
- Dr J.F. Smith and Dr R.D. Page for reading this thesis in its entirety. Also to Dr D.M. Cullen and Dr M.B. Smith for reading parts of it.
- Dr J.R. Cresswell, Dr. Ian Hibbert, Janet Sampson and previous members of staff for help with computing problems, to which I am prone on occasion.
- Andy Boston for his help with MCNP.
- Dr Mark Jones, Dr Paul Campbell and Daniel Grimwood for providing a welcome escape route to Manchester. The mayhem has well and truly commenced.
- Fellow group members: Alan Reed, Alex Keenan and Mike Taylor. See below.
- To all the people who have made my extended period in Liverpool so enjoyable. Especially James Cocks, Stuart Cocks, Dom Duxbury, John Smith and Martin Smith. Also to Duncan Applebe, Kev Cann, Sefa Ertük and David Joss - my fellow finalists.
- Finally, to my family and other friends who inevitably are omitted for brevity, thank you all.

Contents

Chapter 1

Introduction

The content of this thesis describes an experiment that was performed in Jyväskylä, Finland and gives the results obtained from the analysis of the data and the theory required to understand and interpret these results.

Previous studies of the light neutron-deficient lead nuclei [Wo92] [VD84] have provided information on the systematics of excited $J^{\pi} = 0^{+}$ states, mainly through β-decay studies. Further away from the line of β stability, the α-decay branching ratio becomes increasingly competitive compared to that of β decay and eventually dominates. The half-life for α decay continues to decrease for the lighter lead isotopes becoming too short for recoils to be transported to the focal plane of on-line isotope separators, given their large separation times. This prompted a new experimental technique to be devised in order to detect these 0^{+} states for the more neutron-deficient lead nuclide ^{188}Pb [Al98]. A gas-filled separator allows separation to occur prior to α decay and to select the states of interest in this work a new silicon detector array was developed.

The specifications of the new detector array are given in Chapter 3, along with its positioning relative to the existing focal plane detector. Chapter 3 also describes the existing experimental set up and its interface to the data acquisition system. The first two chapters of this thesis are devoted mainly to theoretical aspects of this work. Chapter 1 gives a brief introduction to some nuclear structure and α decay

theory. The main purpose of this chapter is to define the terminology and nuclear properties that are employed later in this thesis. Chapter 2 provides the motivation for the current work and outlines previous results and calculations that are relevant to it. Chapter 4 details early results and the corrections that have to be made to reduce background in order produce the cleanest spectra possible. The results of the analysis are then given in Chapter 5. Finally, band mixing calculations are discussed in Chapter 6 and a summary is given in Chapter 7.

1.1 The Nuclear Shell Model

It is possible to describe the nucleus in terms of a shell structure analogous to that of electrons in an atom. However, there is no equivalent central potential that compares with the potential supplied by the Coulomb field in the atomic case. So, as a starting point it is useful to consider a single nucleon which moves in an average potential or *mean field*. It is an average potential because it reflects the general shape of the nucleus without describing every single aspect of the nuclear force. The Hamiltonian is written as the sum of two terms

$$\hat{H} = \sum_{i=1}^{A} \left[\frac{\hbar^2}{2m} \nabla_i^2 + V_i(r) \right] \tag{1.1}$$

where m is the nucleon mass, $V_i(r)$ represents a potential well at a radius r and the summation is over each individual nucleon. The Pauli principle then states that nucleons should move in definite orbits. A realistic potential that can be used in this Hamiltonian will be described in section 1.1.2.

1.1.1 Axial Deformation

The nuclear surface for an axially-symmetric nucleus can be written as a series summation of the spherical harmonics, $Y_{\lambda 0}(\Omega)$, so that

$$R(\Omega) = c(\beta) R_0 \left(1 + \sum_{\lambda=2}^{\infty} \beta_\lambda Y_{\lambda 0}(\Omega) \right) \tag{1.2}$$

where β_λ are the axial deformation parameters (β_2 corresponding the dominant reflection-symmetric quadrupole shape), $c(\beta)$ is a parameter used to ensure volume conservation and R_0 the radius of a sphere having the same volume as the deformed nucleus [Na93]. An additional parameter γ is used to characterise shapes of nuclei which do not have any axes of symmetry; nuclei that are not axially-symmetric are referred to as triaxial. Nuclear shapes are depicted in the (β_2,γ) plane as shown in figure 1.1.

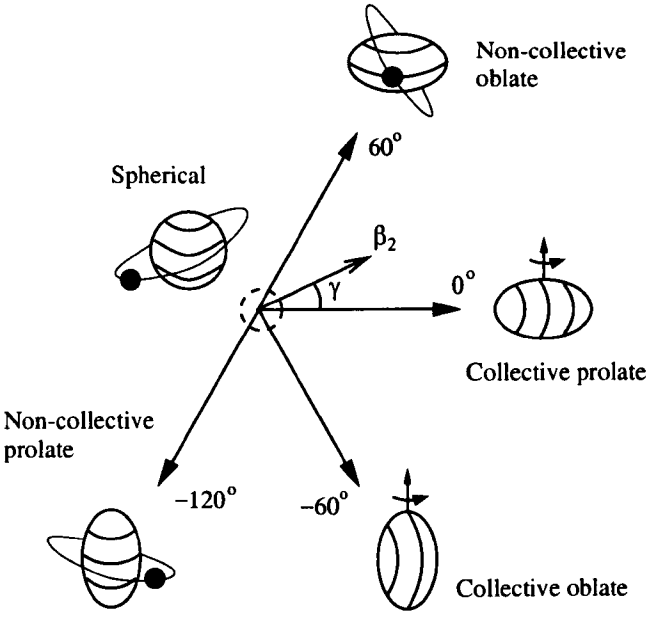

Figure 1.1: The Lund convention [An76] for nuclear deformation.

The Nilsson model, outlined in the following section, uses the deformation parameter ϵ_2 to quantify the quadrupole deformation. This is related to β_2 by the expression [NR95]

$$\epsilon_2 \approx \frac{3}{4}\sqrt{\frac{5}{\pi}}\beta_2 \approx 0.95\beta_2. \tag{1.3}$$

1.1.2 The Nilsson Model

The effect of a deformed potential on single-particle orbits can be described by the Nilsson model [Ni69]. Each orbital has the quantum numbers,

$$[\ N\ n_z\ \Lambda\ ]\ \Omega^{\pi} \tag{1.4}$$

which are shown schematically in figure 1.2; π is the parity which is equal to $(-1)^N$, N is the principal quantum number and n_z the number of oscillator quanta along the symmetry axis. The projection of the orbital angular momentum on the symmetry axis is characterized by Λ and Ω is the projection of the single-particle angular momentum on the symmetry axis. This is defined by $\Omega = \Lambda \pm \Sigma$, where $\Sigma = \pm\frac{1}{2}$ is the projection of the spin on the symmetry axis. Figure 1.2 also shows the total angular momentum $\underline{j}$ which is equal to $\underline{l} + \underline{s}$, where $\underline{l}$ and $\underline{s}$ are the orbital and spin angular momenta, respectively.

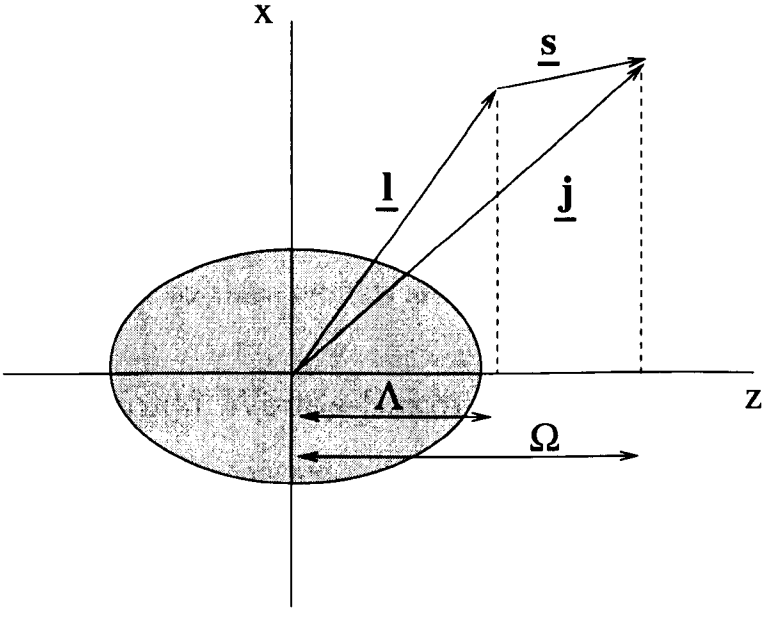

Figure 1.2: Quantum numbers used to describe states in the Nilsson model. Projections are labelled on the symmetry (z) axis.

The Nilsson potential is written as

$$V_{Nil} = V_{osc} - 2\kappa\hbar\omega_0 \left[\underline{l}.\underline{s} - \mu(\underline{l}^2 - \langle\underline{l}^2\rangle_N)\right] \tag{1.5}$$

where κ and μ are constants and ω_0, a function of β_2, is used to parameterize the one dimensional oscillator frequencies. The oscillator potential may be written as

$$V_{osc} = \frac{m}{2} (\omega_x^2 x^2 + \omega_y^2 y^2 + \omega_z^2 z^2) \tag{1.6}$$

where ω_x, ω_y and ω_z are one-dimensional oscillator frequencies in Cartesian coordinates. It can be seen from equation 1.5 that the Nilsson potential comprises a spin-orbit force ($\underline{l}.\underline{s}$) as well as a term to describe the flattening of the potential towards the centre of the nucleus ($\underline{l}^2 - \langle \underline{l}^2 \rangle_N$). A single-particle orbit is labelled by its angular momentum j. Each state with angular momentum j has $(2j+1)$-fold degeneracy, which are then split into $j+\frac{1}{2}$ two-fold degenerate levels with the introduction of deformation [RS80].

The Pauli exclusion principle forbids any two levels having the same quantum-numbers to cross. In the case of deformed nuclei the good quantum numbers are Ω and π, the others acting merely as labels. As levels approach one another they interact, in the process changing their properties and trajectories. Due to the spin-orbit interaction, nuclear orbitals can be shifted so that they become lower in energy and are forced into the oscillator shell below [NR95]. This results in them residing in a level density of opposite parity, where they do not mix and are hence very pure states. Energy levels built on these orbitals are known as *intruder* states.

1.1.3 The Deformed Woods-Saxon Potential

The term proportional to l^2 in the Nilsson potential was found to lower the energy of the high-j orbitals too much, for the heavier nuclei. An alternative is the Woods-Saxon potential [WS54] which is modified to take into account deformation and also to correct the Nilsson single-particle orbits. The deformed Woods-Saxon potential [DW78] is defined as

$$V_{\mathrm{DWS}}(r,\beta) = \frac{-V_0}{1 + exp^{\frac{dist_\Sigma(r,\beta)}{a}}} \tag{1.7}$$

where the parameter $dist_\Sigma(r,\beta)$ is a function of the distance r from the nuclear surface and a deformation parameter β, the parameter $a \approx 0.5$ fm defines the surface

diffuseness.

1.1.4 The Shell Correction Method

The liquid-drop model [My69] likens the nucleus to an incompressible liquid. Although this model describes bulk nuclear properties well, it fails to take into account shell effects. The Strutinsky shell correction method [St67] combines both the collective approach of the liquid drop model and single-particle interactions. In effect, the Strutinsky shell correction superimposes the single-particle energy oscillations onto the total energy from the liquid drop model. The total energy of the nucleus is given by the sum of both these components

$$E = E_{\mathrm{LD}} + E_{\mathrm{shell}} \tag{1.8}$$

where E_{LD} refers to the liquid-drop energy and E_{shell} to the shell energy. A more realistic Yukawa-plus-exponential macroscopic energy can be used instead of the liquid drop energy as it is more sensitive at higher order deformations. The shell correction term can be described as

$$E_{\mathrm{shell}} = \sum_{\mathrm{i}=1}^{\mathrm{A}} \epsilon_{\mathrm{i}}(\delta) - \tilde{E}_{\mathrm{shell}} \tag{1.9}$$

where $\epsilon_{\mathrm{i}}(\delta)$ denotes the eigenvalues in the Nilsson potential and $\tilde{E}_{\mathrm{shell}}$ is subtracted as the part of the total energy that has already been accounted for by the liquid drop model and leaves the shell-model fluctuations.

1.2 Alpha Decay

Alpha decay becomes energetically possible when the sum of the binding energies of the last two neutrons and protons is less than the binding energy of the α particle (28.3 MeV). Alpha particles are emitted with discrete energies and characteristic half-lives. It was in the early 1930s that Rosenblum [Ro30] realized that nuclides emit groups of α particles with distinct energies. In even-even nuclei, such as ^{192}Po, α

decay is most prominent for ground-state to ground-state transitions, rather than to excited levels in the daughter nucleus. The Q-value for α decay [Kr88] may be written in the form

$$Q_\alpha = M_P c^2 - \left(M_D c^2 + M_\alpha c^2\right) = T_\alpha + T_D \tag{1.10}$$

where M_P, M_D and M_α are the parent, daughter and alpha particle masses respectively, c is the speed of light and T_α and T_D the α-particle and daughter kinetic energies. By conservation of linear momentum equation 1.10 maybe written as

$$Q_\alpha = \frac{1}{2}M_\alpha v_\alpha^2 + \frac{1}{2}M_D v_D^2 = \frac{1}{2}M_\alpha v_\alpha^2 \left(\frac{M_D + M_\alpha}{M_D}\right) \tag{1.11}$$

assuming non-relativistic velocities. This expression can be approximated as

$$Q_\alpha \simeq T_\alpha \frac{A}{A-4}. \tag{1.12}$$

A small screening correction E_{scr}, which takes into account the influence of the atomic electron cloud, should be added to this Q-value;

$$E_{scr} = (65.3Z^{7/5} - 80Z^{2/5})eV. \tag{1.13}$$

So, the total α-decay energy for decay to ^{188}Pb is given by

$$E_\alpha = Q_\alpha + E_{scr} = Q_\alpha + 31.8 \text{ keV}. \tag{1.14}$$

The first relationship between the half-life, $\tau_{1/2}$, and the α-particle energy for even-even nuclides was developed by Geiger and Nutall [GN11];

$$\log \tau_{1/2} = a + \frac{b}{\sqrt{T_\alpha}} \tag{1.15}$$

where a and b are parameters specific to each element. This law can be derived from the quantum mechanical barrier penetration described in the following section.

1.2.1 Basic Theory

A simple treatment of α decay is briefly described, as this works sufficiently well for even-even nuclei and is the standard formalism for evaluating reduced α-decay widths [Ra59].

As nucleons condense in the diffuse nuclear surface region, α-particle clusters are formed. However, these clusters still have to penetrate through a potential barrier if they are to be emitted as α particles. A quantum-mechanical theory was developed simultaneously by Gamow [Ga28] and also by Condon and Gurney [CG28] allowing the α particle to tunnel through the high potential of the nucleus. In this model the α particle is assumed to preform within the parent nucleus with a certain preformation probability. It was also assumed that the α particle moved in a potential well determined by the α particle-daughter nucleus system, which is described as the sum of the nuclear, Coulomb and centrifugal potentials. An expression for the α-nuclear potential has been described by Igo [Ig58] through a study of the problem of optical-model analysis. The *optical* potential is complex: the real part gives the force causing elastic scattering, whereas the imaginary part represents the "disappearance" of α particles as they initiate nuclear reactions. The imaginary part yields information on how far an α particle can penetrate nuclear matter without breaking up [Pr62]. The real part of this potential, $V(r)$, is valid in the surface region for $|V| \lesssim 10$ MeV (where α-particle preformation is favoured) and represents the potential barrier which the α particle must traverse. The potential is given by the expression

$$V(r) \;=\; -1100 \exp\left[-\left[\frac{r - 1.17A^{1/3}}{0.574}\right]\right] \text{MeV} \tag{1.16}$$

where r is the distance in fm and A is the mass number.

Assuming that the Wentzel-Kramers-Brillouin approximation is valid (i.e. that the potential is a slowly varying function of the radial distance r from the centre of the nucleus) the barrier penetration factor P [Ra59] for this process is given by

$$P \;=\; \exp\; -2\left[\frac{(\,2\mu\,)^{1/2}}{\hbar} \int_{R_i}^{R_o} \kappa \,\mathrm{dr}\right], \tag{1.17}$$

where μ is the reduced mass of the α particle ($= \frac{4M_D}{4 + M_D}$), R_i and R_o are the inner and outer turning points for a classical α-particle trajectory and

$$\kappa \;=\; \left[V(r) \;+\; \frac{2Ze^2}{r} \;+\; \frac{\hbar^2}{2Mr^2} l(l+1) \;-\; E_\alpha\right]^{1/2}. \tag{1.18}$$

Here, Ze is the charge on the daughter nucleus, l is the orbital angular momentum of the emitted α particle and E_α is the total α-decay energy. The shape of the potential acting on the α particle is illustrated in figure 1.3, with the classical turning points indicated [NR95].

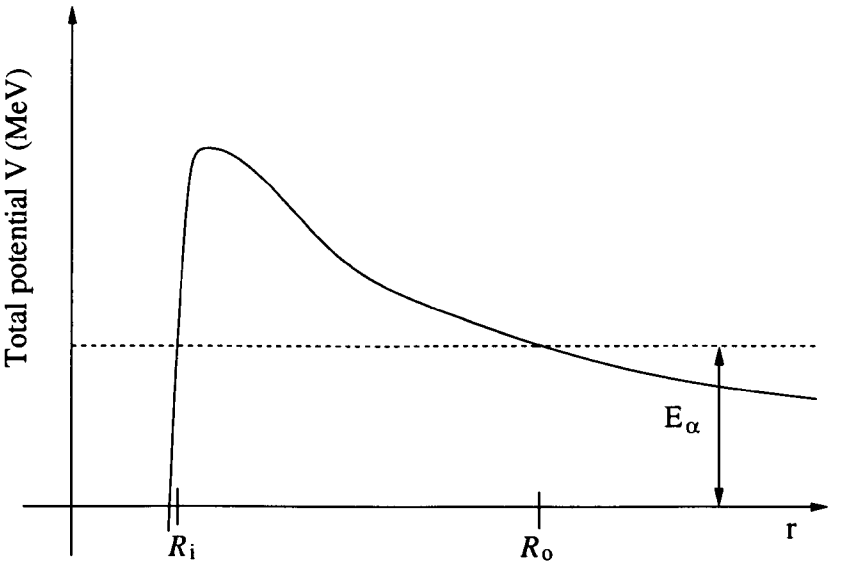

Figure 1.3: Potential acting on the α particle. The dashed line indicates the energy of the emitted α particle, which defines the inner and outer turning points R_i and R_o, respectively.

From measurements of the half-life and branching ratio, b_α, for a given decay the reduced decay width, δ^2, can be evaluated [Ra59] using

$$\delta^2 = \frac{\lambda\, h\, b_\alpha}{P}, \tag{1.19}$$

where λ is the decay constant. The reduced width is the hypothetical decay rate in the absence of a barrier and is related to the preformation probability.

The FORTRAN program BARRY [Pa90] was written to evaluate barrier penetration factors by numerical integration for a range of decay energies and orbital angular momenta. BARRY also provides estimates for the calculated partial half-lives for the decay to each 0^+ state.

1.2.2 Angular Momentum Effects

As the spin of the α particle is zero the angular momentum carried away by it is purely orbital (l). The parity change between states is then given by $(-1)^l$. In cases where the angular momentum carried away by the α particle is non-zero then the additional term $(l(l+1)\hbar^2/2Mr^2))$ from equation 1.18 contributes to the barrier penetrability. This arises from the centrifugal forces associated with the angular momentum.

Figure 1.4 shows a plot of the partial half-life for the decay of ^{192}Po against decay energy, calculated using the BARRY [Pa90] code. As an example, the ground-state to ground-state α transition from ^{192}Po has been indicated along with the expected energy for decay to the excited 0^+ oblate and prolate states and the decay to the 2^+ state observed in the γ-ray studies by Heese [He93]. The hindrance of the decay to excited states can be seen on the effect of the partial (theoretical) half-lives of these two states, remembering that the decays originate from the same state and must, therefore, have the same half-life, but not the same partial half-lives.

1.2.3 Fine Structure in Alpha Decay

When low-lying excited levels in the daughter nuclei are populated in the α decay of the parent, this gives rise to what is known as the *fine structure* of α-decay lines. In decay to excited states the Q-value for the decay will be different and the levels will be populated with different intensities, but because all the decays originate from the same original nuclear state they must all have the same half-life. This, then, contradicts the Geiger-Nutall law of α decay, so it is important to define the concept of the reduced hindrance factor,

$$\mathrm{HF} = \frac{\delta^2_{g.s.}}{\delta^2_{e.s.}} \tag{1.20}$$

where $\delta^2_{g.s.}$ and $\delta^2_{e.s.}$ are the reduced widths of the ground-state to ground-state and ground-state to excited-state α decays, respectively. The reduced hindrance factor can yield information about the nuclear structure of the daughter nucleus and a FORTRAN

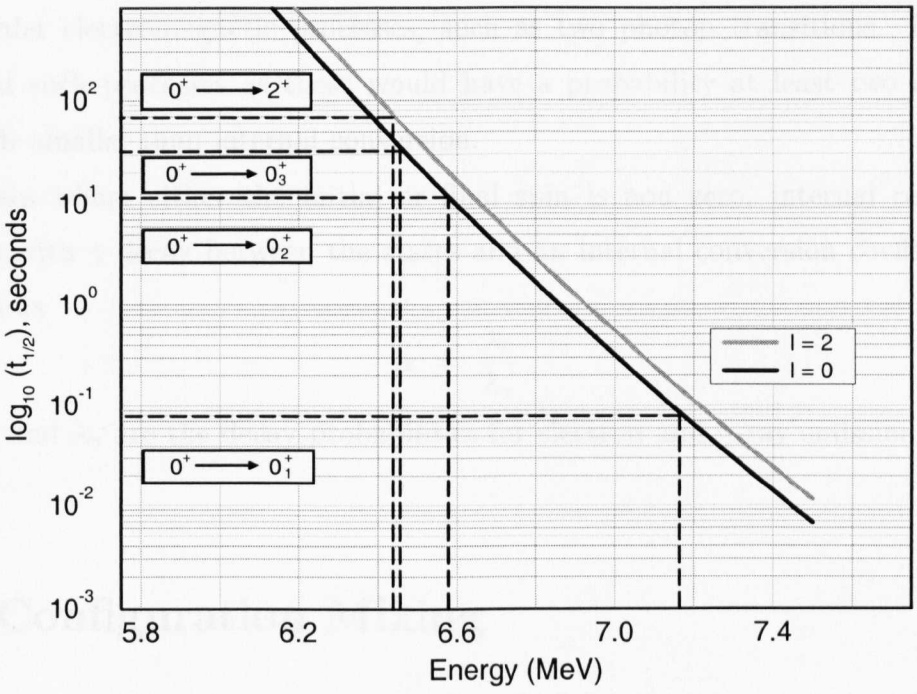

Figure 1.4: Plot of partial half-life against energy, with the α decay from the ground state of ^{192}Po to the four excited states in ^{188}Pb indicated.

program REDWID [Pa90] has been written to calculate reduced α-decay widths using equation 1.19.

1.2.4 Internal Conversion

As γ-ray transitions are forbidden between two 0^+ states, an excited state of spin zero must decay by another means. Internal conversion is a process by which the nucleus transfers its excitation energy to a bound electron, hence moving it to an unbound state. The kinetic energy, T_e, of the electron is then given by

$$T_e = E - B_n \tag{1.21}$$

where E is the transition energy and B_n the corresponding atomic electron binding energy of the electron shell n. The emitted electron is known as a *conversion electron.* As electron shell vacancies are left, they are filled by electrons from higher shells with accompanying X-ray emission. It is possible for $0^+ \rightarrow 0^+$ transitions to occur through

higher order electromagnetic processes, such as two photon transitions. However, in general such processes as these would have a probability at least two orders of magnitude smaller than internal conversion.

In cases where either the initial or final spin is non zero, internal conversion competes with γ decay between the states and an internal conversion coefficient, α, is defined as

$$\alpha = \frac{\lambda_e}{\lambda_\gamma} \tag{1.22}$$

where λ_e and λ_γ are the decay probabilities for electron and γ-ray emission respectively.

1.3 Configuration Mixing

It is very rare that a nuclear state can be described as pure, i.e., consisting of a single configuration. In general, nuclear levels will comprise complex admixtures of more than one configuration. In this section a general treatment of multistate mixing is given.

When energy levels are separated only by small energy differences the residual interaction (which reflects the fact that nucleons do not move completely independently) between the states becomes important. The energy of a pure state $\Phi^{(0)}$ is given by the sum of two terms $E = E^{(0)} + E^{(1)}$ [BG77]. The first term results from the Hamiltonian $H^{(0)}$ that describes the independent-particle motion and the second describes the residual interaction $H^{(1)}$. In the general case where there are n states $\Phi_k^{(0)}$, with $k = 1, ...n$, which have similar energies ($E_k = E_k^{(0)} + E_k^{(1)}$) it is possible that nucleons may scatter from one state to another, due to the residual interaction. Hence, the actual state is composed of a mixture of states $\Phi_k^{(0)}$ and can then be described as a linear combination of the unperturbed states

$$\Psi_p = \sum_{k=1}^{n} a_{kp} \Phi_k^{(0)} \quad (p = 1, ..., n), \tag{1.23}$$

where a_{kp} defines an amplitude, the square of which corresponds to the probability that the nucleus is in a state described by $\Phi_k^{(0)}$. Mixing between the n states is represented schematically in figure 1.5.

The eigenvalue equation to be solved is of the form,

$$H|\Psi_p> \;=\; E_p|\Psi_p> \tag{1.24}$$

where $H = H^{(0)} + H^{(1)}$. This may be rewritten, using equation 1.23, as

$$(H^{(0)} + H^{(1)})|\sum_{k=1}^{n} a_{kp}\Phi_k^{(0)}> \;=\; E_p|\sum_{k=1}^{n} a_{kp}\Phi_k^{(0)}> \tag{1.25}$$

or

$$\sum_{k=1}^{n} <\Phi_l^{(0)}|H^{(0)} + H^{(1)}|\Phi_k^{(0)}> a_{kp} \;=\; E_p a_{lp}, \tag{1.26}$$

which has the shorthand form

$$\sum_{k=1}^{n} H_{lk}a_{kp} \;=\; E_p a_{lp}. \tag{1.27}$$

The eigenvalue equation now becomes a matrix equation

$$[H][A] \;=\; [E][A]. \tag{1.28}$$

from which the eigenvalues E_p can be determined from

$$\begin{vmatrix} H_{11} - E_p & H_{12} & . & . & H_{1n} \\ H_{21} & H_{22} - E_p & . & . & H_{2n} \\ . & . & . & . & . \\ . & . & . & . & . \\ H_{n1} & . & . & . & H_{nn} - E_p \end{vmatrix} \;=\; 0 \tag{1.29}$$

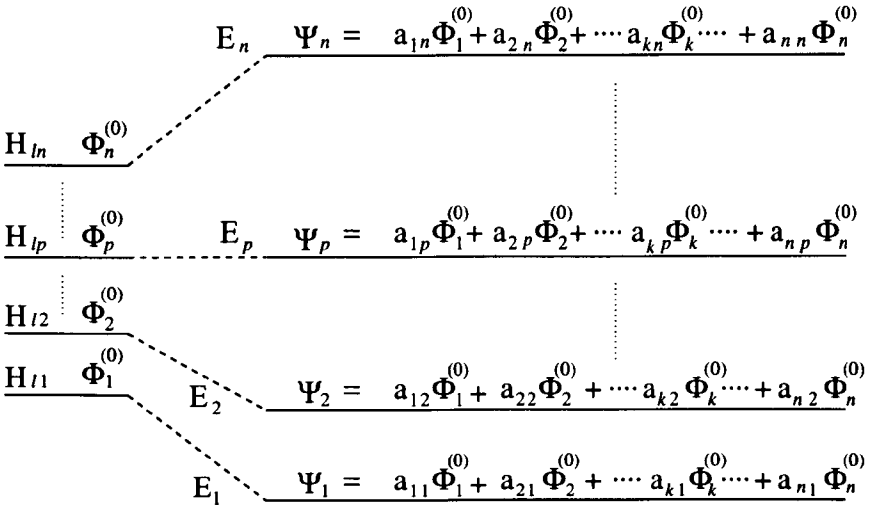

Figure 1.5: Schemetic representation of multi-state configuration mixing.

For the three predicted 0^+ levels in ^{188}Pb the general form reduces to a 3×3 matrix;

$$\begin{vmatrix} H_{11} - E_p & H_{12} & H_{13} \\ H_{21} & H_{22} - E_p & H_{23} \\ H_{31} & H_{31} & H_{33} - E_p \end{vmatrix} = 0 \qquad (1.30)$$

where the (real) cubic roots E_p correspond to the observed energy levels, H_{11}, H_{22}, H_{33} are the unperturbed energy levels and the remaining parameters are the mixing strengths between the levels. The energy matrix is Hermitian which for a real matrix means that $H_{12} = H_{21}$, $H_{13} = H_{31}$ and $H_{23} = H_{32}$. The solutions from this matrix will be presented in the discussion.

1.3.1 Configuration Mixing and Alpha-Decay Transition Probabilities

A treatment of two-level mixing is described by Wauters *et al.* [Wa94] and Bijnens *et al.* [Bi95]. This assumes that the intruder states are based on proton pair excitations through the Z=82 shell gap and that the neutrons do not interact. Two-level mixing

is represented schematically in figure 1.6 where T_1, T_2, T_3 and T_4 are the α-decay transition probabilities between the unmixed normal and intruder states of the parent ($|u>$, $|v>$) and the daughter ($|x>$, $|y>$) nuclei.

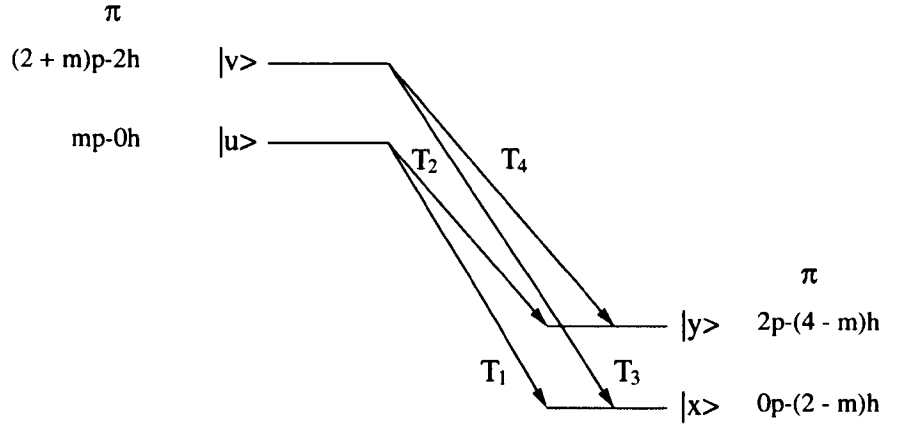

Figure 1.6: Two-level mixing described in terms of proton (particle-hole) level configurations and transition probabilities. In decay from ^{192}Po to ^{188}Pb, m = 2 and for ^{188}Pb to ^{184}Hg, m = 0.

Introducing mixing between ground and excited states in the parent and daughter nuclei the wavefunctions may be written as:

$$\begin{aligned} |u>_{mix} &= a|u> + b|v> \\ |v>_{mix} &= -b|u> + a|v> \\ |x>_{mix} &= c|x> + d|y> \\ |y>_{mix} &= -d|x> + c|y> \end{aligned} \tag{1.31}$$

where normalisation gives $a^2 + b^2 = c^2 + d^2 = 1$. The general form of the reduced hindrance factor is then defined as

$$\mathrm{HF} = \left(\frac{{}_{\mathrm{d}}<0_1^+|\mathrm{T}|0_1^+>_{\mathrm{p}}}{{}_{\mathrm{d}}<0_2^+|\mathrm{T}|0_1^+>_{\mathrm{p}}} \right)^2 = \left(\frac{\mathrm{acT_1} + \mathrm{adT_2} + \mathrm{bcT_3} + \mathrm{bdT_4}}{-\mathrm{adT_1} + \mathrm{acT_2} - \mathrm{bdT_3} + \mathrm{bcT_4}} \right)^2 \tag{1.32}$$

where the subscripts d and p denote the daughter and parent nuclei, respectively. Considering the α-decay of ^{188}Pb (m = 0), transition probabilities T_1, T_3 and T_4 can be considered as one-step processes, but T_2 would involve a two-step process; namely

the the removal of two protons from below the Z=82 shell gap and the promotion of two protons above the shell gap. Hence this transition would be strongly retarded and the assumption is made that T_2=0. The reduced decay widths in the even-even Hg (Z=80), Pb (Z=82) and Po (Z=84) nuclei do not vary significantly, allowing a second assumption that T_1=T_3=T_4. The reduced hindrance factor then simplifies to:

$$HF = \frac{|(a+b)c+bd|^2}{|-(a+b)d+bc|^2} \tag{1.33}$$

Similarly, in the α decay of ^{192}Po (m = 2), the transition T_3 can be considered a two-step process. So, in this case T_1=T_2=T_4 and the reduced hindrance factor is then given by:

$$HF = \frac{|a(c+d)+bd|^2}{|-a(c+d)+bc|^2} \tag{1.34}$$

A more refined model described by Delion *et al.* [De96] (model B) differs from that of references [Wa94, Bi95] (model A) in that it distinguishes between case where emitted α particles are formed from protons occupying levels above and below the Z=82 shell gap. The formalism will be extended to cover three level mixing in the discussion.

Chapter 2

Shape Coexistence

The term shape coexistence implies that a nucleus can exhibit features that can be attributed to different nuclear structures and shapes. This phenomenon arises far from the line of stability where the unusual combinations of neutron and proton numbers can lead to several coexisting minima occurring in the potential energy surface. In the case of the lead nuclei, the different minima that arise at higher deformation energies are interpreted as pairs of protons being promoted to orbitals above the Z=82 shell gap, leaving proton-hole pairs below the shell gap. Evidence for shape coexistence in the lead isotopes was first provided by Van Duppen *et al.* [VD84].

2.1 Theoretical Predictions of Coexisting Shapes in the Lead Nuclei

Considerable theoretical interest [May77][Wo92][Na93][Ta93][Heyd94] has been devoted to trying to describe the phenomena of spherical and deformed states coexisting at low energy and low spin in closed shell nuclei. Due to the Z=82 shell gap ^{188}Pb, consisting of 82 protons, is expected to be spherical in its ground state. However, potential energy surface (PES) calculations by May [May77] and Bengtsson and Nazarewicz [BN89] show the existence of two other minima in the PES. Figure 2.1 clearly shows the minima, one based on a prolate shape ($\gamma = 0°$) and one based on an oblate

shape ($\gamma = -60°$). The energies of these minima are predicted to lie very close to the ground state in ^{188}Pb.

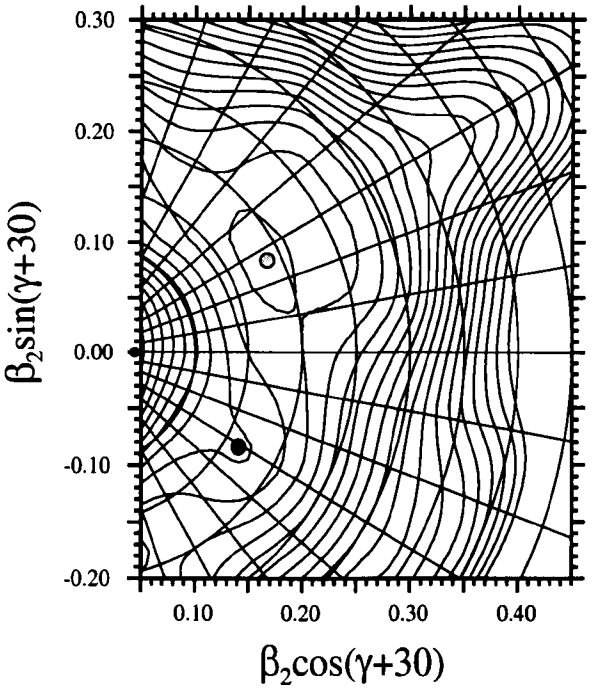

Figure 2.1: TRS calculation, at zero rotational frequency, for ^{188}Pb in the (β_2,γ) plane [Wy89][Na89]. The spherical and deformed minima are represented by the shaded circles. The lightly-shaded circle showing the prolate minimum at $\gamma \simeq 0°$, the darker circle the oblate minimum at $\gamma \simeq$ -60° and the black circle the spherical minimum.

Nilsson-Strutinsky calculations carried out by Nazarewicz [Na93] employed the macroscopic Yukawa-plus-exponential potential [MN88] with an axially-deformed single-particle Woods-Saxon Hamiltonian to describe the shell correction.

The nuclear surface is described as a function of the deformation parameters, β_2 to β_8. The energy minima are obtained performing a multi-parameter minimization of the total energy with respect to β_2 to β_8. These calculations predict oblate states in the lead isotopes with $N \lesssim 118$ at excitation energies of around 1 MeV. At non-zero excitation energies the proton core is broken and deformed configurations are present. A fairly flat minimum appears in the PES corresponding to a weakly deformed oblate configuration with $\beta_2 \simeq -0.15$ and $\beta_4 \simeq -0.01$. The structure of this oblate minimum

corresponds to a two-particle two-hole (2p-2h) proton excitation to the $1h_{9/2}$ (and/or $1i_{13/2}$) shell (the single-particle Woods-Saxon proton levels are shown in figure 2.2). In addition to the oblate states, prolate states with $\beta_2 \simeq 0.27$, $\beta_4 \simeq -0.04$, $\beta_6 \simeq -0.02$ and $\beta_8 \simeq -0.002$ are predicted to occur in the lead isotopes with $N \lesssim 110$. These arise from a well developed minimum formed in the PES, which is not apparent for $A \geq 190$. The energy difference between the prolate and oblate 0^+ states is predicted to be minimum in ^{188}Pb [May77][BN89][Na93].

2.2 Experimental Observations in the Lead Nuclei

Prior to the experiment that forms the basis of this thesis, excited states have been observed in the lead nuclei from mass A=190 to A=208. The first evidence for the existence of excited $J^\pi = 0^+$ states in even-even lead nuclei arose through the population of ^{206}Pb via direct two-neutron pick-up and stripping reactions [Ig70]; the nature of the reaction providing strong evidence for the 2p-2h character of the observed state. Further evidence was provided by studying the β decay of mass-separated bismuth isotopes [VD84][VD85][VD87]. The observed low-lying $J^\pi = 0^+$ energy levels in the even-even neutron-deficient ^{190}Pb to ^{200}Pb nuclei were also attributed to 2p-2h configurations. A collective band based on the excited $J^\pi = 0^+$ state in ^{196}Pb was observed by Penninga [Pe87], who deduced the 2p-2h character of these states from the measured g-factors of two isomeric states within the band. The energy deficit usually associated with the promotion of two protons across the Z=82 shell gap is largely recouped through the residual pairing energy of the two particles and two holes and the proton-neutron quadrupole correlation energy in the excited 2p-2h configuration. In-beam γ-ray studies [He93] of the light lead isotopes ^{186}Pb and ^{188}Pb, have provided strong evidence for rotational structures in those nuclei although excited 0^+ states were not observed due to the decay out of the band to the ground state. The observed levels were assigned to have a prolate deformed configuration due to similarities with states in the isotones ^{184,186}Hg. The dynamic moments of inertia of these bands are

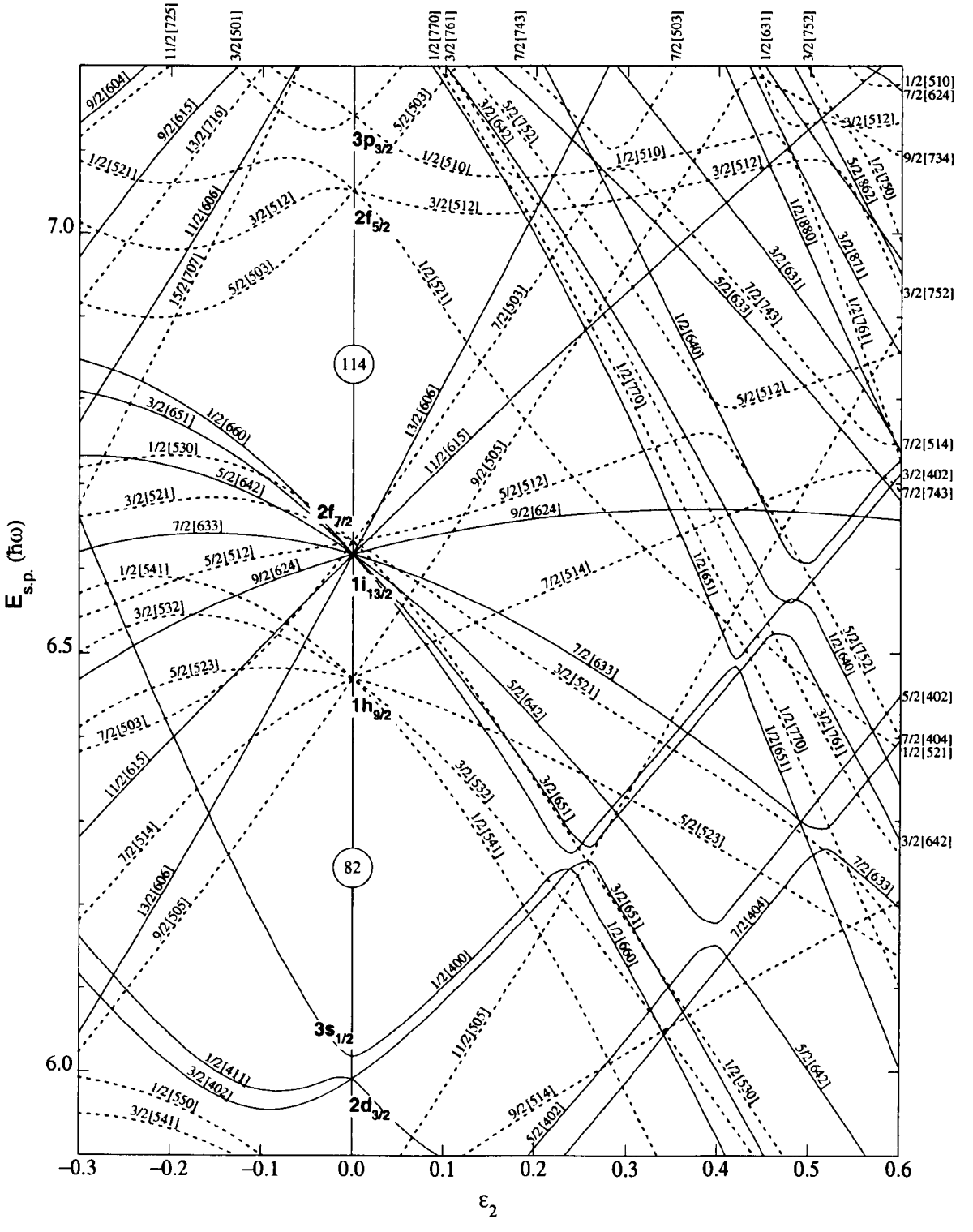

Figure 2.2: Single-particle Woods-Saxon proton levels versus the quadrupole deformation ϵ_2.

in agreement with a prolate deformation $\beta_2 \simeq 0.26$ [Ma86][Ja83].

2.2.1 Systematics of the Low-lying 0^+ Oblate States

All of the excited $J^\pi = 0^+$ states already observed in the even-even lead isotopes, $^{190-208}$Pb, have been attributed to oblate shapes [BN89]. With increasing oblate deformation (negative β_2) it becomes increasingly energetically possible for a pair of protons to be excited across the Z=82 shell gap. The protons can be excited into the down-sloping $[505]\frac{9}{2}^-$ ($h_{9/2}$) or $[606]\frac{13}{2}^+$ ($i_{13/2}$) Nilsson orbitals, leaving a proton-hole pair in the up-sloping $\frac{1}{2}^+[400]$ ($3s_{1/2}$) orbital (see figure 2.2). Exciting the nucleus into a spherical 2p-2h configuration costs almost twice the energy gap at Z=82 ($E_x = 2(\epsilon_p - \epsilon_h) \approx$ 7MeV). Therefore, deformed intruder configurations can become competitive with the regular configurations. The excitation energies of these intruder states decreases towards neutron mid-shell as shown in figure 2.3. It has been predicted [Na93] that the excitation energy will reach its minimum for ^{188}Pb. Performing a quadratic fit to the observed data points it is possible to extract an excitation energy of approximately 590 keV for the state in ^{188}Pb. However, due to the mixing between states of the same spin and parity in this nucleus the observed value may be shifted from this extrapolated value.

More quantitatively, it has been shown that these level energies could be predicted well from the positions of the $\pi h_{9/2}[505]\frac{9}{2}^-$ and $\pi s_{1/2}[400]\frac{1}{2}^+$ bandheads in the Tl and Bi isotopes [VD87][Hey88], using the equation

$$E(0_2^+, {}^A\mathrm{Pb}) = E(9/2^-, {}^{A-1}\mathrm{Tl}) + E(1/2^+, {}^{A+1}\mathrm{Bi}) + \Delta_c \qquad (2.1)$$

where E is the excitation energy and Δ_c is a correction to allow for residual particle-hole interactions. The correction is expected to be independent of neutron number and has been calculated, from the positions of the intruder levels in ^{187}Tl [Co85] and ^{189}Bi [Wa97], as $\Delta_c = 190 \pm 8$ keV. Using this method for ^{188}Pb the expected value is 667 keV, after allowing for residual particle hole interactions [VD90]. Alternatively, Brenner [Br92] has suggested that the excitation energies of the 0_2^+ states varied

linearly with the factor

$$P = \frac{N_p N_n}{(N_p + N_n)} \tag{2.2}$$

where $N_p(= 4)$ and $N_n(= 208 - A)$ are the valence nucleon numbers. Using this method the excitation energy may be obtained from the equation

$$E(0_2^+, {}^A\mathrm{Pb}) = 6.504 - 1.789P \text{ MeV} \tag{2.3}$$

where the coefficients have been obtained from a fit to heavier lead nuclei ($^{190-198}$Pb). This method predicts that the 0_2^+ excitation energy will be 540 keV above the ground state.

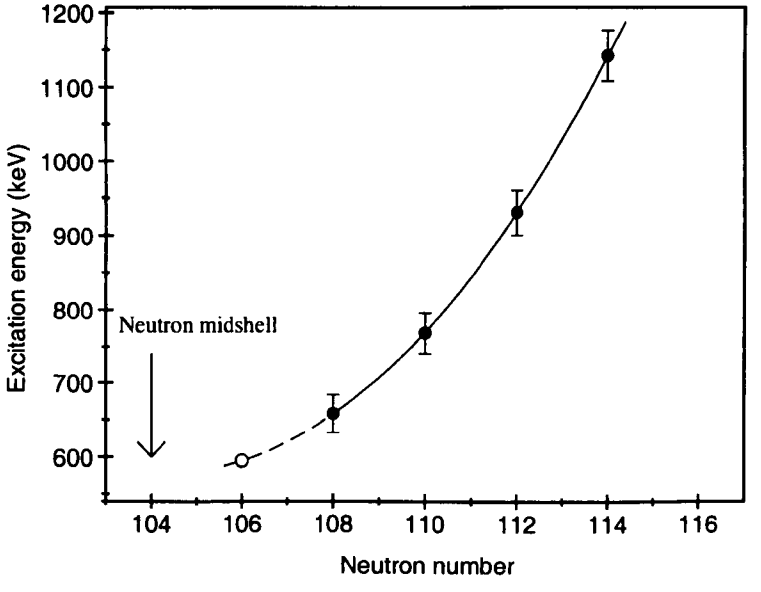

Figure 2.3: Systematics for the excitation energy of the oblate $J^\pi = 0^+$ states observed in the lead nuclei. The solid circles are the observed states and the open circle represents the value extrapolated to ^{188}Pb from the data.

2.2.2 Observation of the Prolate Band in ^{188}Pb

Gamma-ray spectroscopy studies by Heese *et al.* [He93] have shown the existence of prolate bands in ^{186}Pb and ^{188}Pb similar to those seen in the mercury isotones.

The structure of these bands can be associated with 4p-4h and 6p-6h excitations in the lead isotopes [Na93]. The prolate bandhead is not observed due to decay out of these bands to the ground state. However, it is possible to fit the energy levels from the transitions of the prolate band in ^{188}Pb and extrapolate using a simple rotational model to gain an estimate of the energy of the unperturbed prolate bandhead. A convenient method to fit the unperturbed energy levels is using the variable moment of inertia (VMI) model described by Mariscotti *et al.* [Mar69]. In the VMI model, the excitation energy of a state with a spin I is given by

$$E_I = E_0 + \frac{I(I+1)}{2J_I}\left(1 + \frac{I(I+1)}{4CJ_I^3}\right) \tag{2.4}$$

where E_0 is an extra term for the excitation energy of the bandhead and C is a parameter specific to a given rotational structure. The moment of inertia J_I of the level with spin I is obtained as the single real root of the cubic equation:

$$J_I^3 - J_I^1 J_0 - \left[\frac{I(I+1)}{2C}\right] = 0 \tag{2.5}$$

where J_0 is the moment of inertia for the bandhead. Figure 2.4 shows the fit to the experimental energies of the 6^+ to 14^+ levels in ^{188}Pb from the work of Heese *et al.* The 4^+ level is displaced by ~15keV, due to mixing, while there is evidence for a backbend around the 16^+ level, so these levels were not included in the fit. Extrapolating this fit, one expects the prolate bandhead to be at an energy of ~710 keV.

The calculated level energy predictions for the oblate and prolate 0^+ states are summarised in table 2.1

Oblate			Prolate
Tl/Bi	N_pN_n	Systematics	Extrapolation
667	540	590	710

Table 2.1: Estimated energies (in keV) of the excited 0^+ levels in ^{188}Pb.

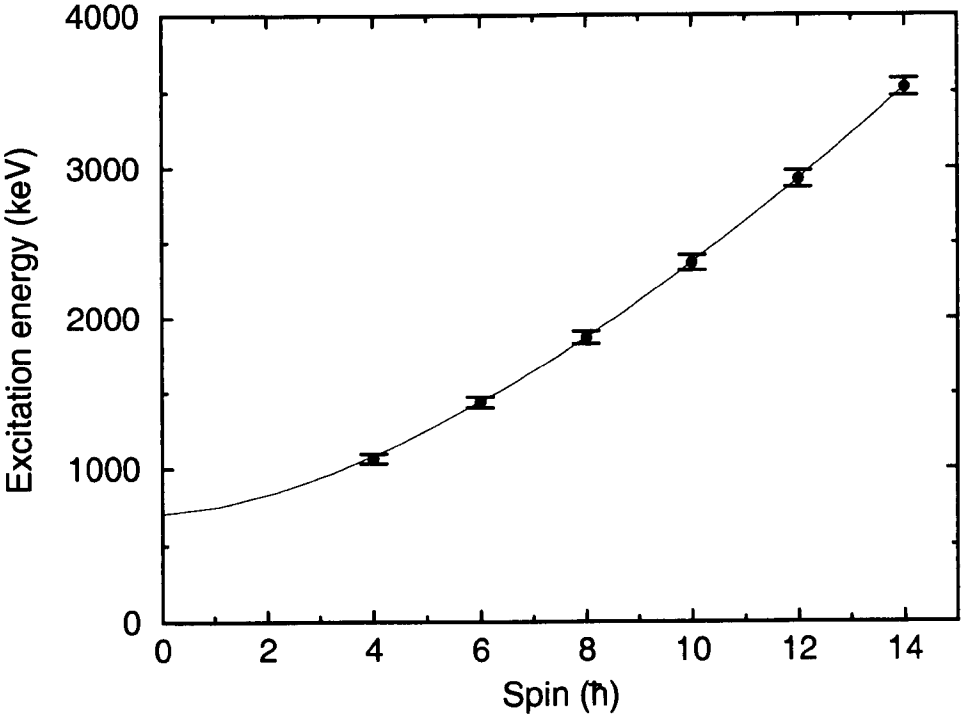

Figure 2.4: Level energies for the prolate band observed in ^{188}Pb.

Chapter 3

Experimental Details

In order to investigate shape coexistence in ^{188}Pb, an experiment has been performed at the University of Jyväskylä. The K130 cyclotron was used to produce a beam of ^{36}Ar with an ionic charge state of 8^+. The beam energy was set at 192 MeV and adjusted using a selection of nickel degrader foils, listed in table 3.1. The beam was pulsed with a period of 10 ms on and 10 ms off. The beam pulsing allowed decay events to be observed in the beam off period when there was no background from recoiling nuclei. The average beam intensity was 38 pnA.

The ^{192}Po nuclei were produced in a heavy-ion fusion-evaporation reaction with a thin (0.5 mg cm^{-2}) isotopically enriched target comprising 67.1% ^{160}Dy, 20.9% ^{161}Dy, 6.3% ^{162}Dy, 3.4% ^{163}Dy and 2.3% ^{164}Dy, through the 4n evaporation channel. The recoiling evaporation residues were separated from the beam using the gas-filled separator RITU and implanted into a position sensitive silicon strip detector. Alpha-particle spectra were monitored on-line in order to run at the optimum degraded beam energy for production of ^{192}Po nuclei. This information was subsequently used in a separate in-beam γ-ray study of ^{192}Po using the recoil-decay tagging technique [Hel96].

Ni degrader foils	
Thickness (mg cm^{-2})	Energy loss (MeV)
2.70	24
2.25	20
1.80	16
1.35	12
0.90	8
0.45	4

Table 3.1: Beam energy loss through the available degrader foils.

3.1 The Gas-filled Recoil Separator RITU

In order to be sensitive to the fusion-evaporation residues produced at low cross-sections a recoil separator has been used to suppress other reaction products and the unreacted beam. The Recoil Ion Transport Unit (RITU) was used, which is a gas-filled device that separates recoiling ions, from the beam, in-flight through the presence of a magnetic field. RITU consists of a QDQQ (Q = quadrupole; D = dipole) arrangement and is schematically represented in figure 3.1. The bending dipole magnet separates out the evaporation residues from the beam, whilst the quadrupole magnets are for improving the angular acceptance and for focusing.

3.1.1 Principle of Operation

The idea of the gas-filled separator was initially developed by Cohen and Fulmer [CF58] and the first separator to employ this method in heavy element studies was SASSY [Gh88] at the Lawrence Berkeley National Laboratory, U.S.A. It was using this separator that the α decay of ^{192}Po was first observed [Le81]. In a gas-filled separator, recoiling products undergo a large number of charge-changing collisions with the gas atoms leading to ions of the same species following a trajectory defined

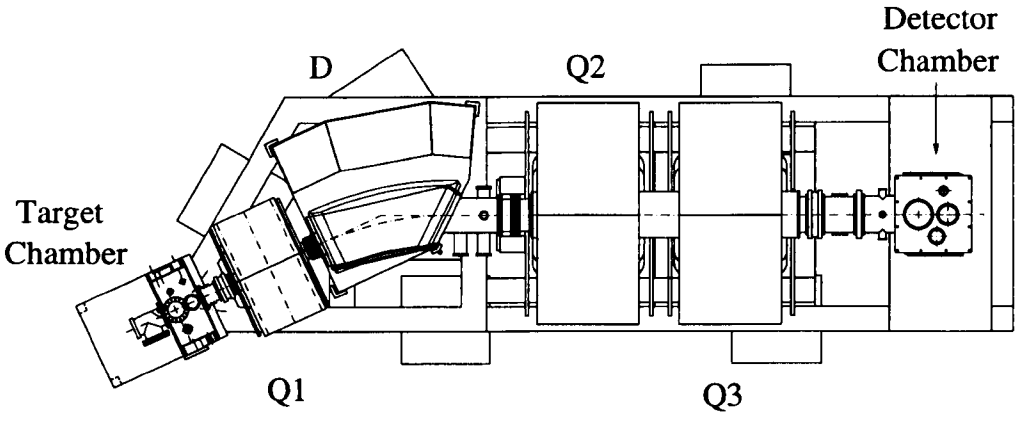

Figure 3.1: A schematic diagram of the recoil separator, RITU.

by their average charge state (q_{ave}) in the gas. Considering an ion with momentum mv following a trajectory of radius ρ the separation can be described in terms of the magnetic rigidity $B\rho$ by the formula

$$B\rho = \frac{mv}{eq_{ave}}. \tag{3.1}$$

Using the Thomas-Fermi model of the atom [Th27][Fe28] to approximate an expression for the average charge state then gives

$$B\rho = \frac{mv}{\left(\frac{ev}{v_0}Z^{1/3}\right)} = \frac{0.0227A}{Z^{1/3}}\ \text{Tm} \tag{3.2}$$

where A and Z are the atomic mass and atomic number of the ion respectively and v_0 (= 2.19 x 10^6 m/s) is the Bohr velocity. Equation 3.2 summarises an important property of the gas-filled separator; $B\rho$ is independent of the velocity and the initial charge state distribution of the ions. The separation efficiency of RITU is very good because of this charge state focusing.

As an example, a comparison can be drawn between RITU and the Fragment Mass Analyzer (FMA) [Da92] at Argonne. The FMA operates at high vacuum, but it uses a combination of two electric dipoles and a single magnetic dipole to separate reaction products, according to their mass-to-charge (m/q) ratio. Although this allows a

definite mass assignment to be made it has a lower efficiency than RITU. In the case of ^{192}Po the separation efficiency of the FMA was measured as 5% [Fo97] compared with 20% for that of RITU [Le95].

3.1.2 Properties of the Separator

RITU has an advantage over other gas-filled separators in that the first quadrupole magnet is positioned in front of the dipole magnet in order to achieve better matching to the dipole acceptance. The acceptance is estimated to be approximately 30% higher than for the normal DQQ design [Le95].

The dipole separates the evaporation residues from the beam which is then dumped to an electrode "ski" housed inside the dipole chamber. The residues are then transported to the focal plane detector via the two horizontally and vertically focusing quadrupole magnets. The magnet settings are optimised by examining the position distribution of evaporation residues implanted into the silicon detector mounted at the focal plane of RITU. RITU is filled with helium at a pressure of around 1 mbar, the helium pressure being maintained by continuous gas flow which is extracted at the detector chamber. The specifications of the separator are given in table 3.2. Within the target chamber a target wheel is used so that a target can be changed by means of an external feedthrough, without breaking the vacuum. Up to twelve targets can be mounted on the target wheel.

3.2 Silicon Strip Detectors

This section outlines silicon semiconductor devices as charged particle detectors. The process of constructing detectors suitable for the purposes of the experiment is also discussed.

RITU parameter values	
Magnetic configuration	$Q_1DQ_2Q_3$
Maximum beam rigidity	2.2 Tm
Bending radius	1.85 m
Acceptance	10 msr
Dispersion	10 mm/%
Mass resolving power(vacuum mode)	100
Dipole bending angle	25°
Dipole entrance angle	0°
Dipole exit angle	-25°
Pole gap(D)	100 mm
Q_1 maximum gradient	13.5 T/m
Q_1 effective length	350 mm
Q_1 aperture diameter	105 mm
$Q_{2,3}$ maximum gradient	6.0 T/m
$Q_{2,3}$ effective length	600 mm
$Q_{2,3}$ aperture diameter	200 mm
Total weight	17500 kg
Total length	4.8 m

Table 3.2: Specifications of the RITU spectrometer.

3.2.1 Semiconducting Materials

Semiconducting materials can be used as an effective medium for detecting nuclear radiation. The high density of such materials means that the dimensions of the detector can be kept very small in comparison with, for example, gas-filled detectors.

Silicon is a valence-4 atom and will form covalent bonds with its neighbouring atoms. Valence electrons participating in covalent bonds form a low-energy valence band. A higher energy conduction band also exists corresponding to free electrons being able to migrate through the material. These two regions are separated by a band gap. Without thermal excitation the valence band is completely full. However, at non-zero temperature it is possible for an electron to be promoted across the band gap creating an electron-hole pair. The presence of an electric field allows electrons and holes to migrate through the material.

3.2.2 Doped Semiconductors

To improve the properties of semiconducting materials impurities, known as dopants, are added. Valence-3 atoms inserted into the silicon crystal attempt to form covalent bonds with neighbouring atoms producing an excess of holes. These form acceptor levels in the band gap just above the valence band. Due to the excess of holes these materials are called p-type semiconductors. Similarly, valence-5 atoms doped into the silicon creates an excess of electrons, forming donor levels just below the conduction band; these are known as n-type semiconductors. The effects of adding dopants to semiconductors effectively reduces the band gap, as shown schematically in figure 3.2.

3.2.3 The Semiconductor Junction

If n-type and p-type materials are brought into good electrical contact then a p-n junction is formed. Charge carriers diffuse across the junction creating a region, where electrons and holes combine, known as the depletion region. Electrons migrating from the n-type region leave behind fixed positively-charged donor sites and holes from the

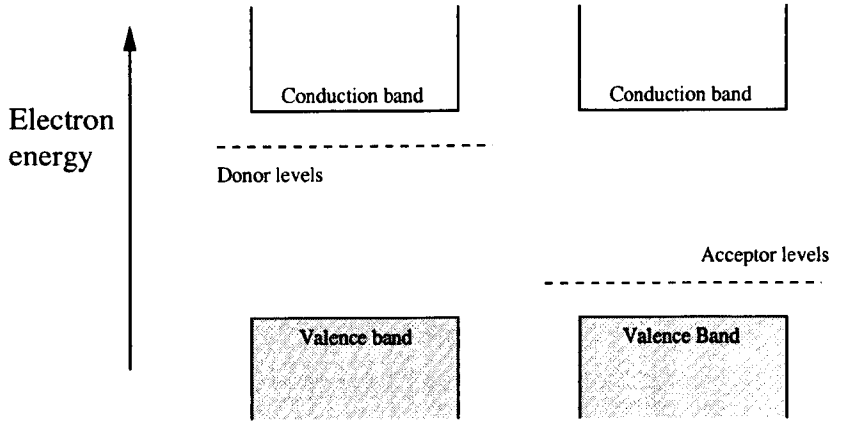

Figure 3.2: (Left) Silicon doped with valence-5 atoms. (Right) Silicon doped with valence-3 atoms

p-type region leave behind fixed negatively-charged acceptor sites. The resulting electric field eventually stops further migration.

If a reverse bias is applied across the junction, that is the p-side is made negative with respect to the n-side, the potential difference across the junction is enhanced as shown in figure 3.3. In this case, minority carriers (holes on the n side and electrons on the p side) flow across the junction. As the number of minority carriers is low the reverse current across the diode is small. Hence, there is free flow of current in one direction, but there is a large resistance to its flow in the other. As the applied bias increases the potential difference across the junction, Poisson's equation

$$\nabla^2\phi = \frac{\rho}{\epsilon} \tag{3.3}$$

(where ϕ is the potential, ρ the net charge density and ϵ the dielectric constant in the medium) dictates that the space charge must increase, extending the dimensions of the depletion region [Kn89]. Applying a large enough bias can lead to the detector being fully depleted. In such a scenario the depletion region covers the whole of the semiconductor wafer, on which the junction is formed. This has the following advantages over partially depleted detectors;

- it reduces Johnson noise, which can be associated with poor electrical contacts, if the depletion region is extended all the way to the contacts

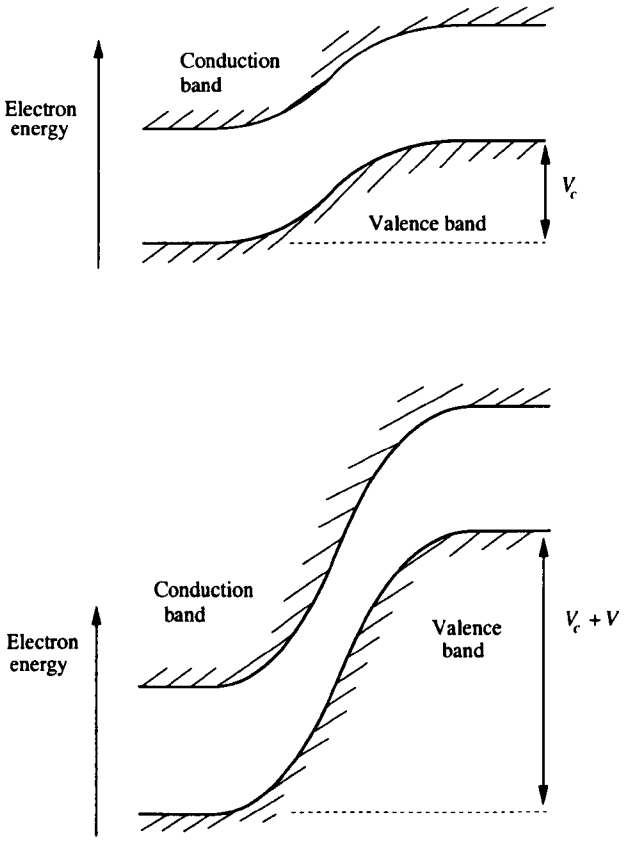

Figure 3.3: Effect of applying a reverse bias, V, across the junction.

- it reduces charge capacitor noise in the preamplifiers.

Incident ionizing radiation entering the depletion region will create many electron-hole pairs with the number of pairs created being proportional to the incident energy of the particle. The applied reverse bias then makes the charge collection more efficient.

3.2.4 Passivated Implanted Planar Silicon Detectors

Mildy n-type silicon is *passivated* by forming an oxide layer through heating the silicon wafer. Photoligraphy techniques, described by Kemmer [Ke84], are used to remove areas of the oxide to create entrance windows. The p-n junction is formed when acceptor ions are implanted, so that a thin layer of silicon within the windows is

converted to p-type material. The other surface of the silicon is implanted with donor ions, producing a layer of n^+ material to serve as a blocking electrical contact. At this point the wafer is annealed to remove radiation damage to the implanted layers. Aluminium contacts are added at the front and rear surfaces.

This oxide passivation process allows extremely low leakage currents, hence reducing noise to around 1 keV or less at room temperature and the very thin p^+ *dead layer* gives excellent energy resolution of around 30 keV full width half maximum (FWHM) for α particles of approximately 7 MeV.

3.2.5 Detector Characteristics

Leakage Current

When a reverse bias is applied across the p-n junction a small leakage current is observed, even in the absence of ionizing radiation. The source of this current can be classified in two areas. Bulk leakage occurs within the volume of the detector and is caused by;

- minority carriers being conducted across the junction
- the thermal generation of electron-hole pairs within the depletion region.

Minority carriers will always be attracted towards the junction but this rarely contributes significantly to the overall leakage current. Cooling of the detector allows the thermal generation of electron-hole pairs to be minimized.

The second source of leakage is mainly due to contamination in the surface of the detector. To reduce surface leakage, clean encapsulation techniques are employed. The method described in section 3.2.4 of keeping the junction edges within the silicon wafer keeps this source of current within tolerable levels. A fairly constant leakage current is an indicator of good detector performance. An increase may degrade the resolution of the detector [Kn89].

Pulse Height Defect

Not all of the incident particle energy will contribute to the production of electron-hole pairs, as some energy is lost due to nuclear stopping. Consequently, the observed pulse height will be smaller than if all the particle energy was lost by pair creation. Nuclear stopping is a relatively small fraction of the total energy loss and in the case where α-particle energies are being measured from a calibration with α particles of approximately the same energy, the effect is negligible. However, the effect becomes larger when heavier ions, such as recoiling nuclei, are being measured.

Radiation Damage

The most common mechanism for radiation damage is known as the *Frenkel defect.* If an atom in the silicon lattice becomes displaced from its normal site, a vacancy is left and the atom positions itself at an interstitial site. These now act as trapping sites for the charge carriers allowing the recombination of electrons and holes. If enough of these traps are formed the energy resolution of the detector will be degraded, due to fluctuations in the amount of charge lost and the timing properties will also be affected. Although the effects are permanent they can be lessened by annealing the detector.

3.2.6 Position Sensitivity

The position-sensitive silicon detector used in the present work was an 80 mm $\times$ 35 mm $\times$ 300 μm wafer. Position sensitivity is achieved in the x-direction by sub-dividing the surface area of the silicon into independent strips, the number of strips giving the number of co-ordinates in that direction. The use of a resistive back layer for each separate strip enables y-position information to be obtained. The resistive layer acts as a charge divider, so that if signals are taken from both ends of each strip

the ratio of one of these signals to the sum will be proportional to the position of implantation along the strip. Each strip has a position resolution of about 0.4 mm [Hel96].

3.3 Silicon Detector Array

In order to detect the conversion electron emitted in the decay of the excited 0^+ state, an array of silicon detectors is mounted around the existing position sensitive implantation detector. The implanted recoils and their subsequent α decays are detected in the implantation detector (thickness 300 μm), whilst the emitted electrons are detected in the surrounding array, as these have a much longer range than the α particles. These detectors also measure α and β particles which escaped from the implantation detector without depositing their full energy. The array consists of six individual silicon detectors each of which is divided into four quadrants, shown in figure 3.4. The thickness of each detector was approximately 465 μm, which is deep enough to stop fully normally incident electrons with energies of up to approximately 300 keV [Be69].

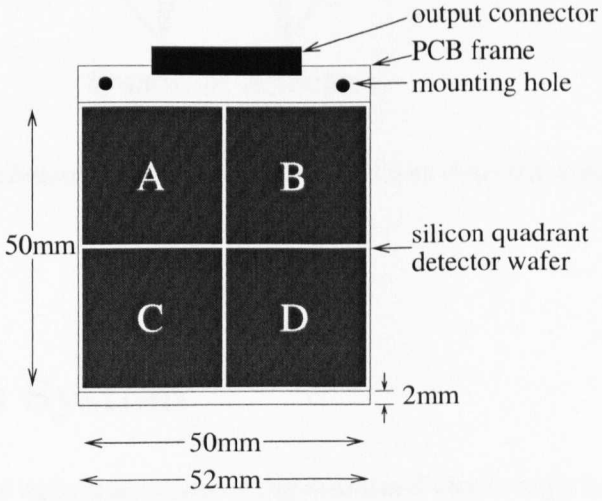

Figure 3.4: Front view of the quadrant detector.

3.3.1 Geometry of the Array

A mount has been constructed so that the six quadrant detectors could be housed in a box shape surrounding the implantation detector (also referred to as the PAD detector). Figure 3.5 shows a 3-D schematic of the array, the beam direction being perpendicular to the plane of the implantation detector (into the page). The main criterion for the position of the quadrant detectors is that they are mounted as close as possible to the PAD detector for maximum efficiency. The geometry of the detector array allows for a range of angles of incidence, which serves to increase the effective detector thickness. The physical dimensions of the array are indicated in figure 3.6.

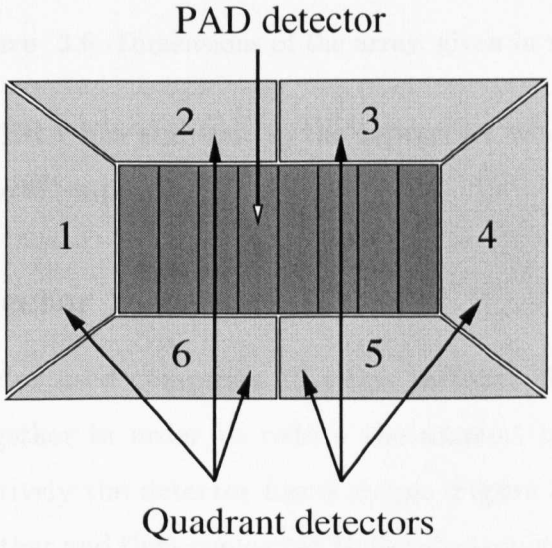

Figure 3.5: Schematic of the PAD and quadrant detector array.

3.4 Electronics System

The electronics system is an amalgamation of the standard electronics for the implantation detector and the quadrant array. The signals were recorded using the TARDIS data acquisition system, developed at the University of Liverpool. Coincidence data

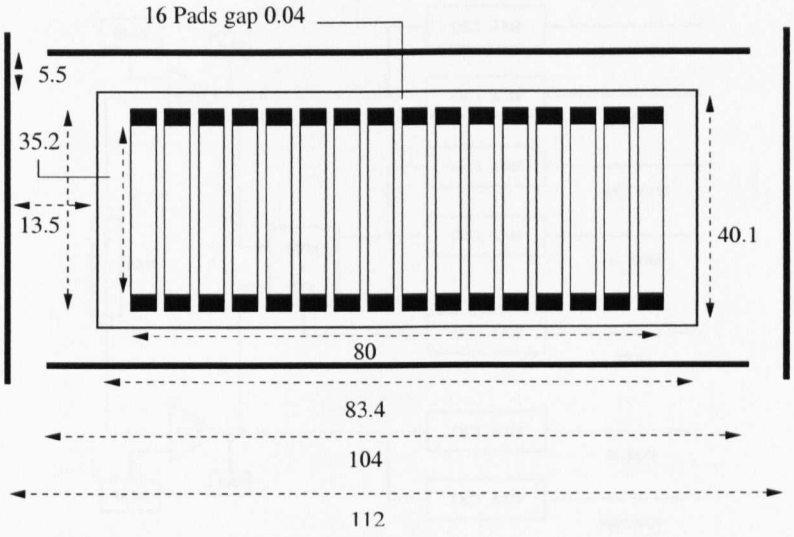

Figure 3.6: Dimensions of the array, given in mm.

are read out via the FERA bus and sent to the tapeserver where they are stored on 8 mm magnetic "Exabyte" tape.

3.4.1 PAD Detector System

The silicon PAD detector used comprises 16 strips in total. Each pair of adjacent strips are coupled together in order to reduce the amount of electronics modules required, so that effectively the detector has 8 strips. Figure 3.7 indicates how two strips are coupled together and then connected to the electronics. The PAD detector is operated at a bias of approximately -60V (fully depleted). An impedance adjustment is employed to each signal on each strip to allow corrections to be made for position dependence on energy, for which fine adjustments can be added in the offline analysis. In total there are 7 amplifying channels for each strip. A high-gain channel is used for α particles (top, bottom and sum) and a low-gain channel for recoiling nuclei (top, bottom and sum). The sum signal is achieved by adding the top and bottom signals using a sum and inverting amplifier. The seventh channel is used for a trigger.

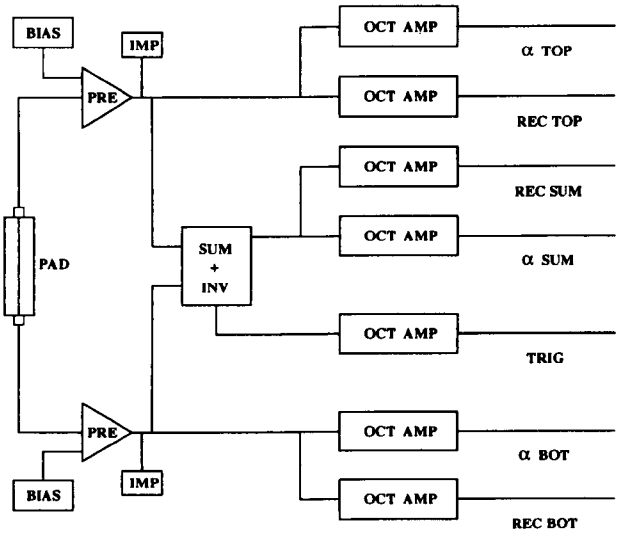

Figure 3.7: Electronics set up for one PAD detector strip.

3.4.2 Quadrant Array Detector System

Each quadrant detector was operated at a bias voltage of -30V. Each individual quadrant energy signal is fed through a preamplifier to a spectroscopy amplifier. The signals for the four quadrants comprising one quadrant detector are summed, using a sum and inverting amplifier before being delivered to the ADCs. In total six ADCs are required for the quadrant detectors. Timing signals are taken both from the implantation and quadrant detectors. After going through a fast timing filter amplifier (TFA) the analogue pulses that are above the noise threshold are processed by a constant fraction discriminator (CFD) so they may be inputted to a fan in/fan out unit. There are 24 quadrant logic signals in total and 8 PAD signals at this point. The quadrant signals are grouped according to the sector of the quadrant they belong to. That is, all sectors of each quadrant detector marked A, indicated as in figure 3.4, are fed to the same fan in/fan out unit. This is then repeated for sectors B, C and D of the quadrant detectors. This effectively gives an "OR" signal for the four sectors of the quadrant detectors. A similar set-up is used for the 8 strips of the implantation detector to give an any "PAD" trigger. An event in any of the four sectors of any of the six quadrant detectorsgives an any "quadrant" trigger. These two signals are sent

to the TAC to give the timing difference between an event in the implantation and an event in any of the quadrant detectors. A coincidence between these two triggers gives the master trigger. This is schematically represented by the block diagram in figure 3.8. The six energy signals from each strip of the implantation detector are

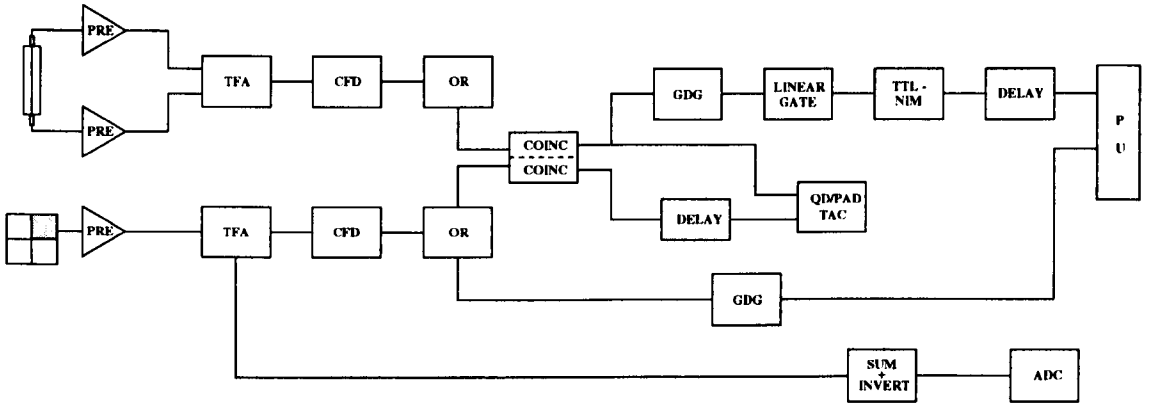

Figure 3.8: Block diagram indicating how the master trigger is produced.

sent to six individual multiplexers. The multiplexers are triggered by a pulse from the pattern trigger, so that only one PAD event is recorded by the ADCs at any one time. The pattern unit records which strip of the implantation detector was hit, as well as which sector of the quadrant detector was hit. This is shown schematically in figure 3.9. Energy spectra for each individual detector could then be produced in the offline sorting.

3.4.3 Data Acquisition

Data converted by the ADCs are collected through the TARDIS data acquisition system. The system can collect data in either singles or coincidence mode, where the ADC signal must be accompanied by a master trigger. Each ADC is connected to an ADC interface card contained within the VME crate. In singles mode, data is read out when an ADC receives a signal, for coincidence data the readout control (ROCO) unit must receive a master trigger. In the context of the experiment, coincidence events are of more importance than singles. Upon a coincident event, the ROCO stops

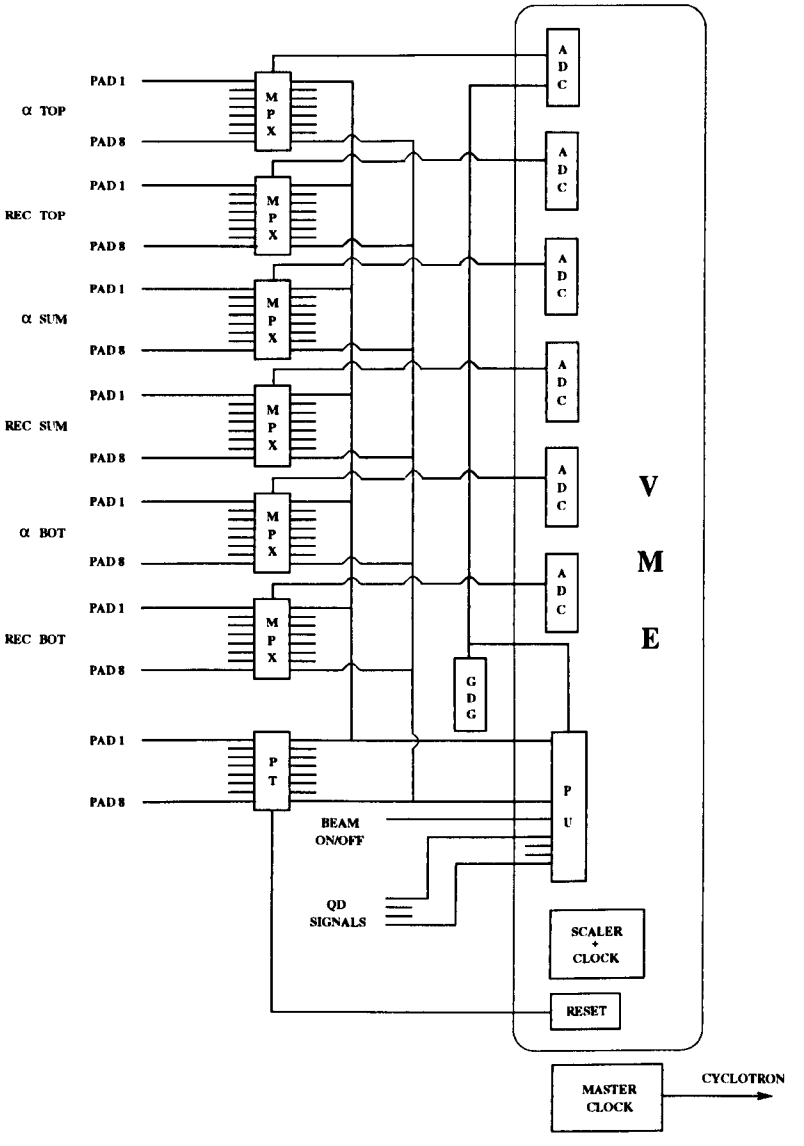

Figure 3.9: Processing of the individual energy signals from the PAD and quadrant detectors to the VME system.

singles collection. Signals from the ADCs are read out by the FERA ADC interface manager and stored in memory. The Event Builder CPU converts the FERA events to EUROGAM format and the data is sent to the tapeserver via an ethernet link.

Chapter 4

Data Analysis

In order to be able to distinguish the weak α decays of interest from all the other α-decaying nuclei produced a new method of identification had to be devised. Theoretical predictions [Na93] for the excitation energy of the excited 0^+ states in ^{188}Pb suggest that the α-decay energies to these states would be similar to the energies of several α decays from nuclei also produced in the reaction. As the production cross sections for these nuclei are greater than that for ^{192}Po and given the weakness of the decay to the excited states, the fine structure of interest would be swamped by the ground-state to ground-state α decay of the other reaction products.

The array described in section 3.3 is used to detect the conversion electron emitted in the decay of the excited 0^+ state to the ground state. By taking a coincident measurement between an electron in these quadrant detectors with an α-decay event in the PAD detector it is possible to select the events of interest out of the background arising from ground-state to ground-state decay events.

Firstly, however, corrections need to be applied to the recorded detector signals in order to achieve the best possible energy and position resolution.

4.1 PAD Detector Matching

4.1.1 Correcting for Position Dependence

The energy signal recorded in hardware will have some dependence on the position of implantation/decay as the top and bottom PAD energy signals use different amplifiers and preamplifiers, implying the use of different impedances and gains. There may also be a variation due to slight non-uniformity in the resistance along each strip of the implantation detector. It is possible to correct for this dependence by adding back a fraction of either the top or bottom energy signals to the sum signal. In effect, a corrected sum energy signal E_{corr} is defined;

$$E_{corr} = E_{sum} + nE_{top} \tag{4.1}$$

where E_{sum} is the total energy signal from a single strip, E_{top} the energy signal from one end of a single strip and n is a correction factor. In some cases it was also necessary to add a quadratic correction factor. An example of an uncorrected and corrected energy spectrum is given in figure 4.1. The values of n typically ranged between ± 0.01. By taking a 1D-projection onto the energy axis, it can be seen (figure 4.2) that this correction greatly improves the energy resolution of the detector.

4.1.2 Gain Matching

Once each individual strip of the PAD detector has been corrected ensuring there is no y-position difference with energy, each strip then has to be matched so that the α lines in each are all aligned. Three peaks were fitted for each strip and then a linear fit was performed for each strip against one other strip, which was chosen as a reference. This gave a *gain* and an *offset* value for each strip, allowing them to be aligned in the offline sorting by defining a new energy for each, which was of the form

$$E_{strip} = (E_{corr} \times gain) + offset + \text{RANDOM} - 0.5 \tag{4.2}$$

where E_{strip} is now the gain matched energy in each strip of the implantation detector and RANDOM is a randomly generated number between 0 and 1, which ensures that

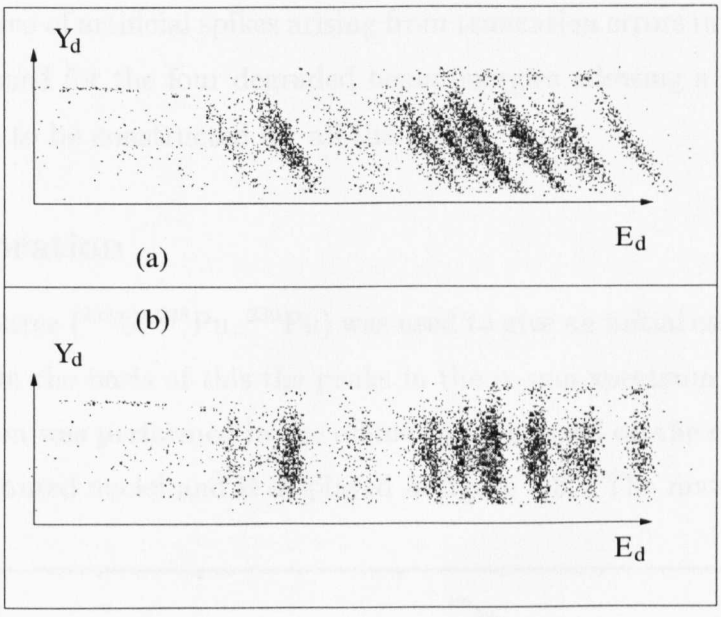

Figure 4.1: (a) Uncorrected positon against decay energy spectrum and (b) corrected by adding back a linear and quadratic fraction of the top energy signal.

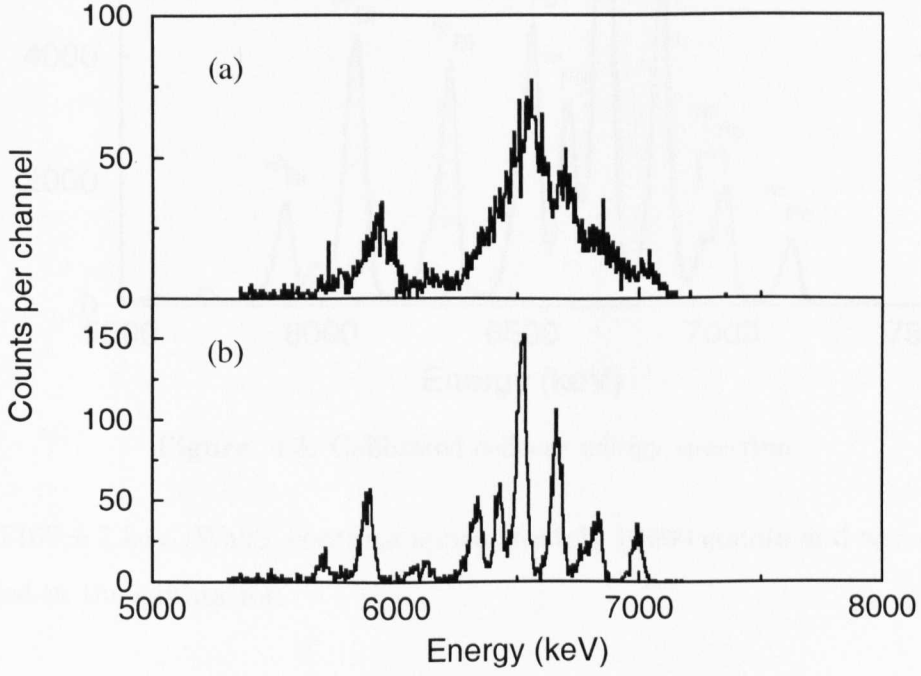

Figure 4.2: Corresponding 1D-projections onto the energy axis from figure 4.1.

the spectra are free of artificial spikes arising from truncation errors in the calculation. This was performed for the four degraded beam energies allowing a summed-energy (E_{pad}) spectrum to be constructed for all the data.

4.1.3 Calibration

A three-line α source (^{233}U, ^{238}Pu, ^{239}Pu) was used to give an initial calibration for the PAD detector. On the basis of this the peaks in the α-sum spectrum were identified. A final calibration was performed in the offline sorting based on the energies of the α lines of the implanted nuclei and is displayed in figure 4.3. The main ^{192}Po α decay

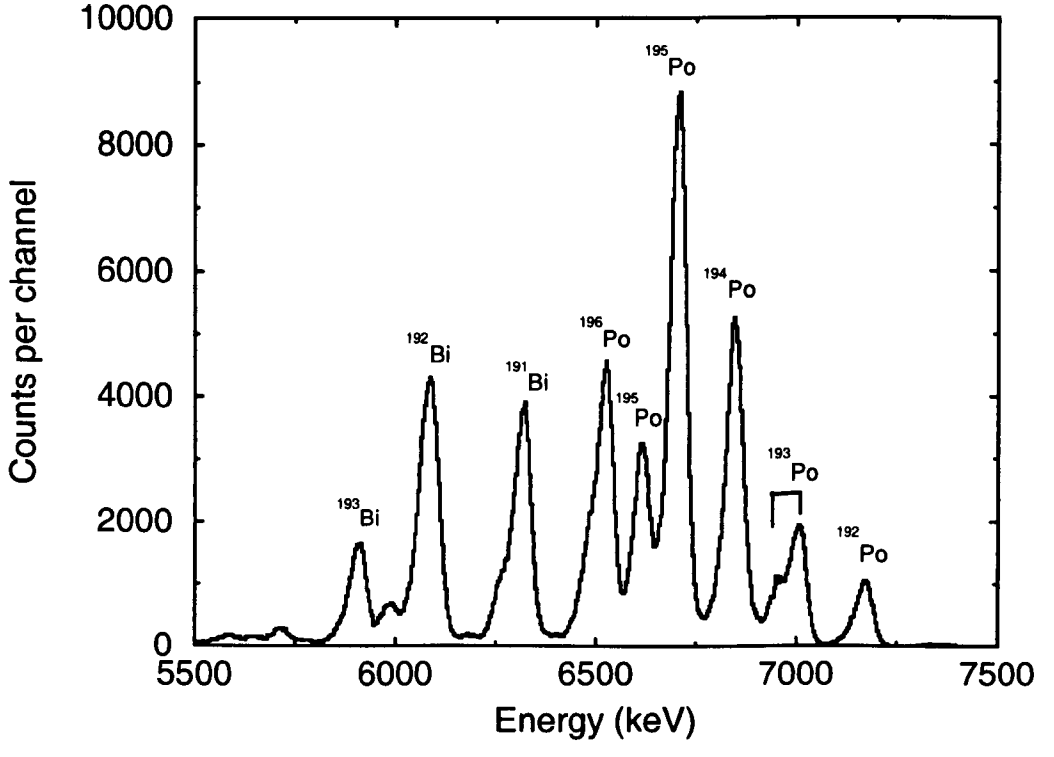

Figure 4.3: Calibrated α-decay energy spectrum.

line at 7167 ± 7 keV [Wa93] contains approximately 12000 counts and was one of the lines used in the calibration.

4.1.4 Position Corrections

Background can be reduced further by selecting only decay events that are correlated with the parent nucleus, provided the half-life of the decay is short enough. The energy, position and time information for each recoil event are stored in individual arrays, each array effectively being an 8 × 256 channel matrix. For each individual decay event a sort program searches back through the previously stored recoil events until it can correlate a recoil event that occurs within a specified position and time difference with the decay event. Up to 256 recoil events are stored for each of the 8 strips of the PAD detector.

In order to perform position correlations, it had to be ensured that the position difference between the recoil and observed decay event had no dependence on the position of implantation along any given strip of the silicon detector. The position difference is defined as

$$\mathrm{ydf} = \mathrm{yd} - \mathrm{yr} = \frac{256\mathrm{E_d(top)}}{\mathrm{E_d(sum)}} - \frac{256\mathrm{nE_r(top)}}{\mathrm{E_r(sum)}} \tag{4.3}$$

where n is a correction factor, yd and yr are the decay and recoil positions and E_d and E_r are the decay and recoil energies respectively. By incrementing 2-D spectra of ydf against yd (and yr) within the correlation loop and adjusting the correction factor in the definition of the recoil position, the gradient of these plots can be made equal to zero. In this scenario yd is approximately equal to yr for the correlated events. The gradient is measured as accurately as possible from the plot and the necessary adjustment is made to the value of n. Fine adjustments can be made by projecting the plot and measuring the FWHM of the position difference peak until its value reaches a minimum. Figures 4.4 and 4.5 show plots of the decay and recoil positions respectively against the position difference, before and after the corrections have been made to the value of yr. It was also required that there was no position dependence on the energy of the implanted recoil. Figure 4.6 shows the uncorrected and corrected 2-D plots of recoil energy against position difference.

Once these corrections have been made it is possible to observe a narrow position

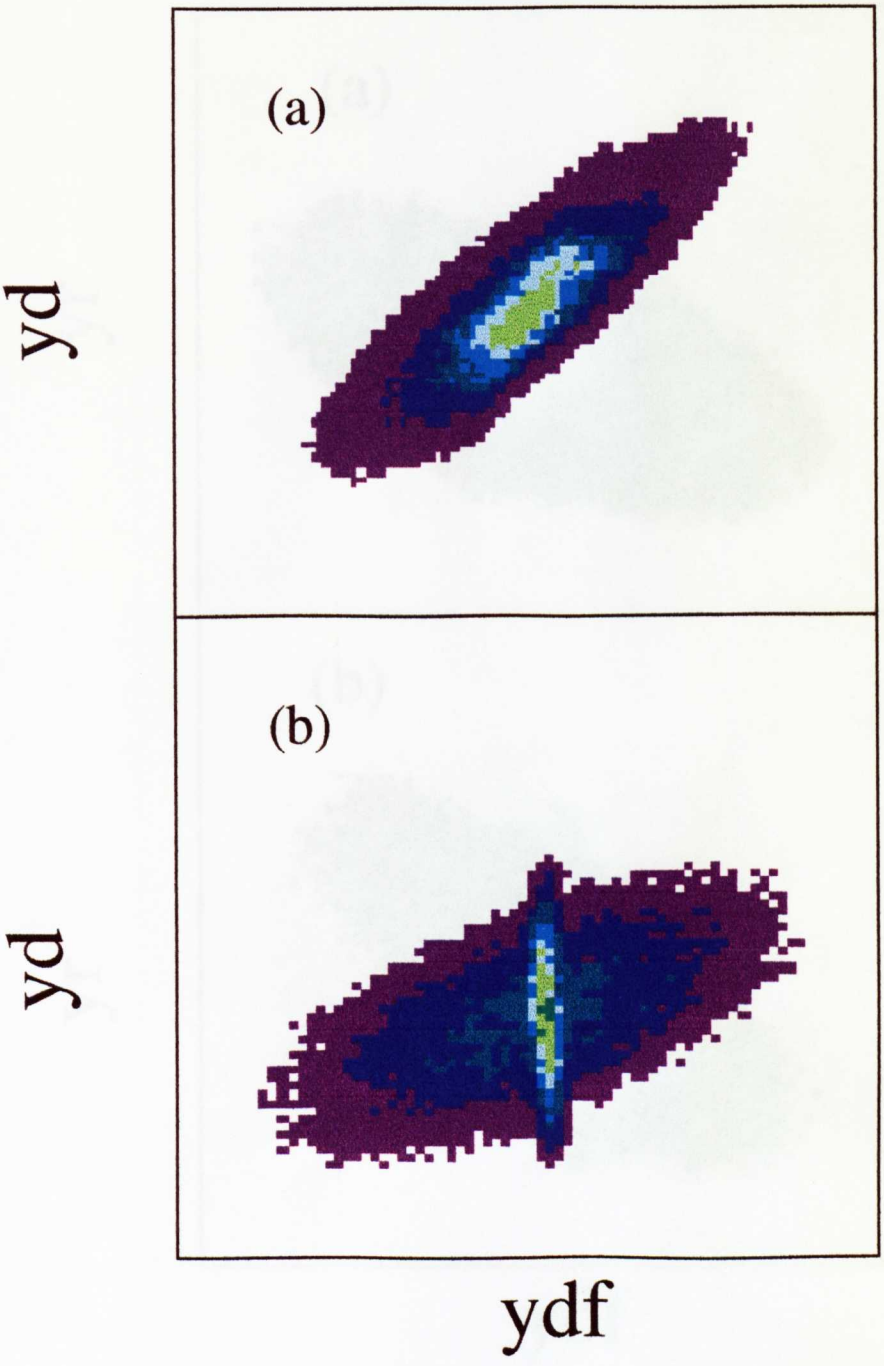

Figure 4.4: Uncorrected (a) and corrected (b) spectra of ydf against yd.

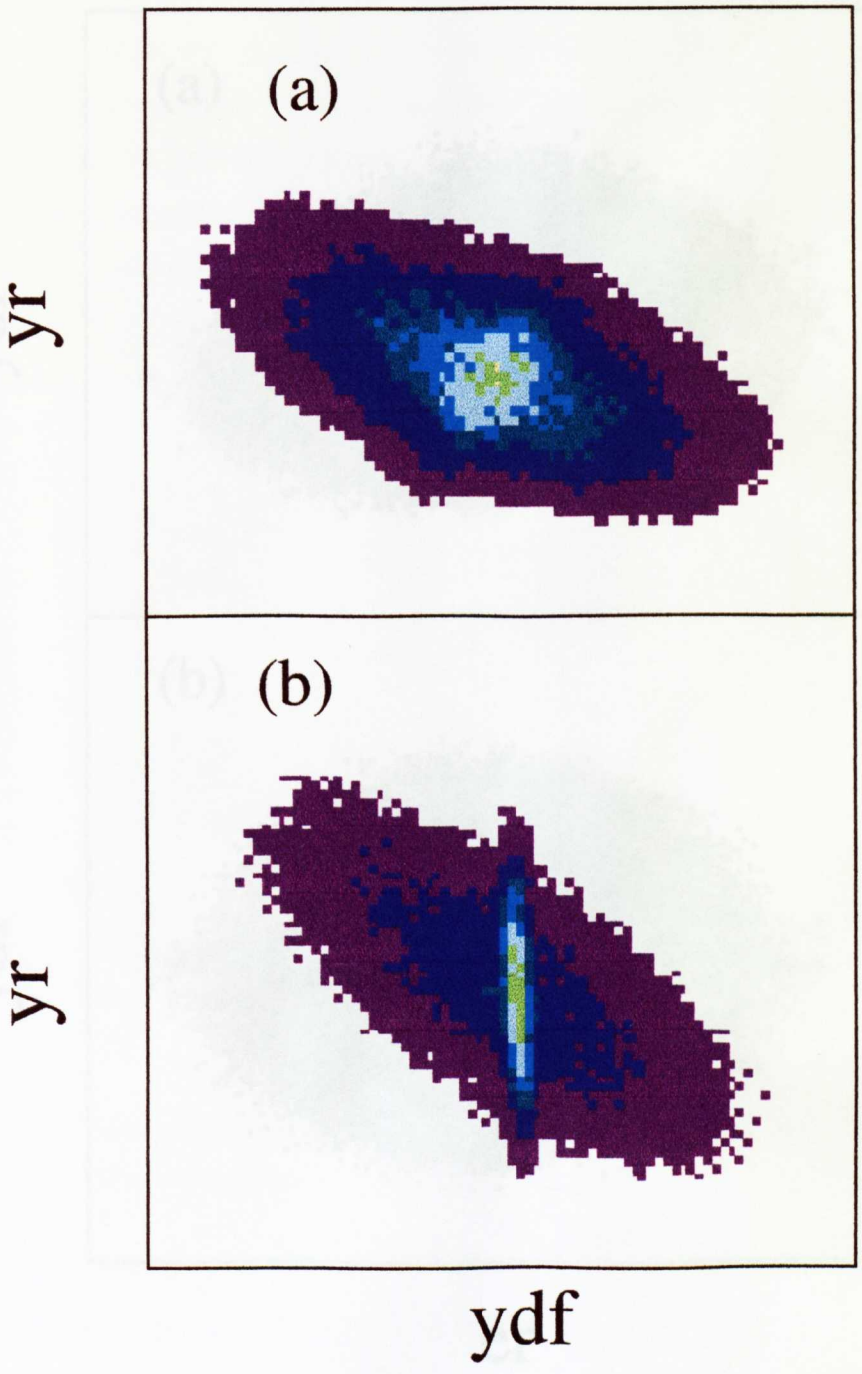

Figure 4.5: Uncorrected (a) and corrected (b) spectra of ydf against yr.

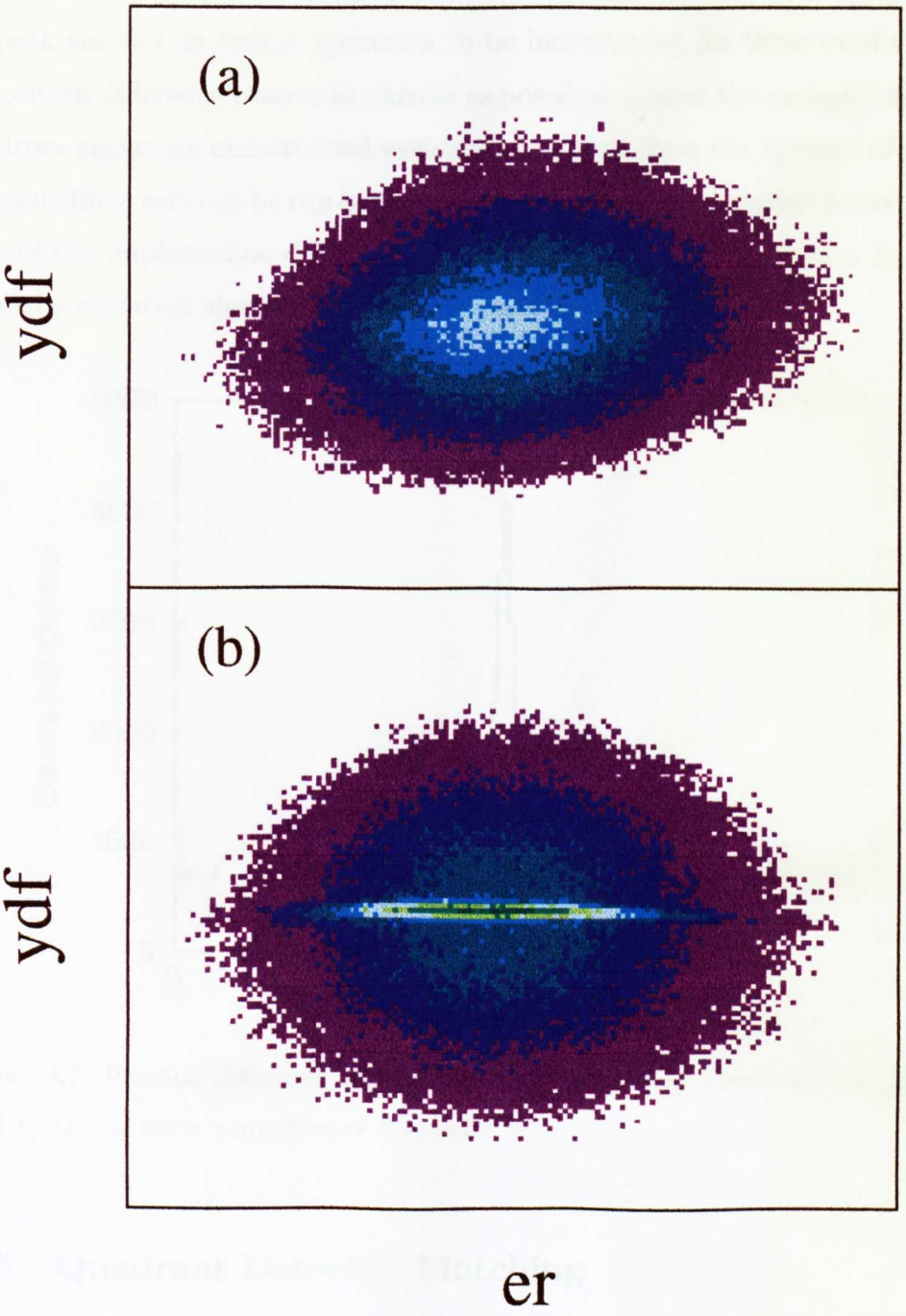

Figure 4.6: Uncorrected (a) and corrected (b) spectra of ydf against recoil energy (er).

LIVERPOOL

difference peak (figure 4.7) for the correlated events. The position resolution was measured to be around 0.31 mm (FWHM). Placing a narrow position gate around this peak enables an energy spectrum to be incremented for these events. Ensuring the position difference peak is as narrow as possible reduces the background that may arise from gating on uncorrelated events. In order to show the method of correlation works an offline sort can be run in which one searches for a correation between different strips of the implantation detector. Incrementing an energy spectrum from such an artificial correlation should produce only random events.

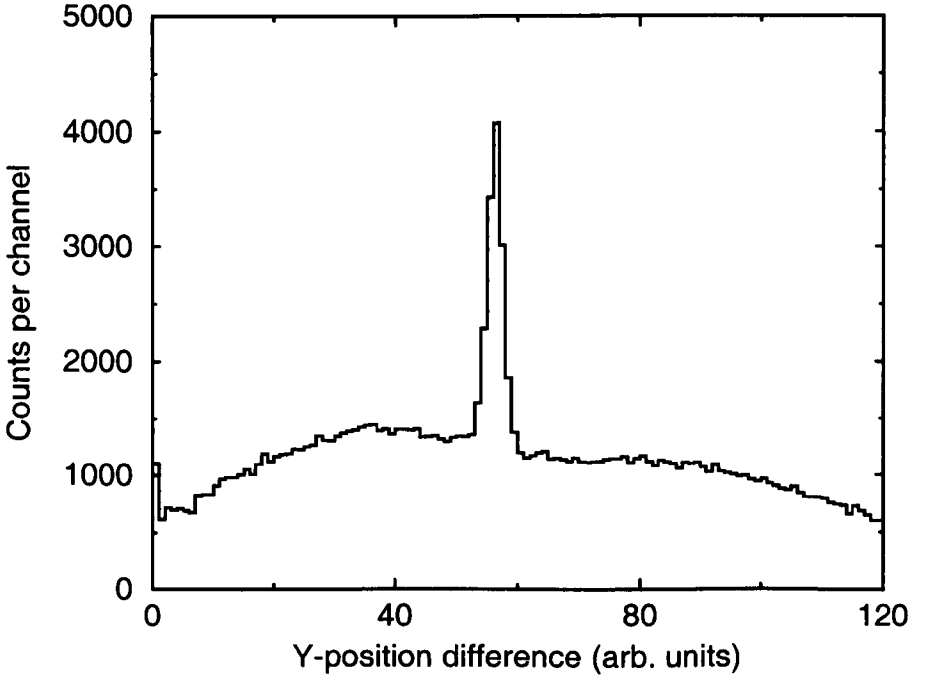

Figure 4.7: Position difference spectrum between correlated recoil and decay events obtained by taking the y-projection of figure 4.4.

4.1.5 Quadrant Detector Matching

Once again the three-line α source was used for the initial calibration. Each individual quadrant was matched to the PAD α-spectrum. In the case of a coincidence between

the PAD and quadrant detectors an *addback* sum energy of the form

$$E_{addback} = (m \times E_{quadrant}) + E_{pad} + \text{RANDOM} - 0.5 \tag{4.4}$$

is constructed. $E_{quadrant}$ refers to the matched quadrant energy and the multiplicative factor m is a correction factor used to obtain the best resolution possible for these addback spectra. Typically m varied between 0.94 and 1.02. A two-peak fit was then performed, in a similar fashion as that for the PAD detector, so that each quadrant could be matched to a chosen reference and a summed-energy spectrum created, as shown in figure 4.8. A summary of the detector resolutions is given in table 4.1.

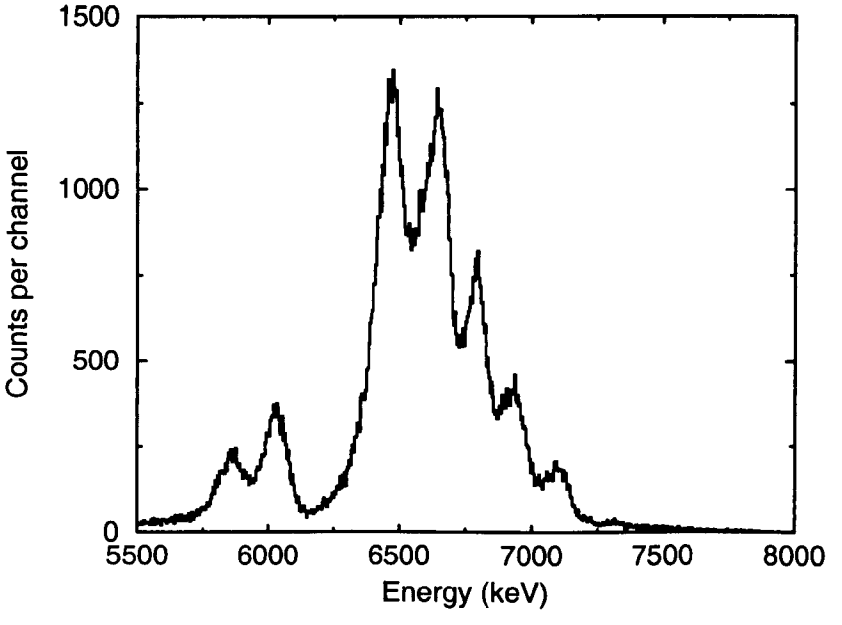

Figure 4.8: An example of a matched addback sum spectrum.

After the signals have been corrected it is possible to look at energy spectra from the implantation detector in coincidence with electron events in the surrounding quadrant detectors. This method allows the weak α decays of interest to be distinguished from the ground-state to ground-state α decays that are produced with similar energies and at a much larger cross section.

Detector	FWHM (keV)
PAD (measured)	48
PAD and quadrant coincidence (measured)	124
quadrant (calculated)	114

Table 4.1: Detector resolutions from single beam energy (172 MeV).

4.2 Cross Section Determination

To determine the optimum energy for the production of ^{192}Po four different beam energies were used. During the experiment the yields of ^{192}Po nuclei were monitored on-line at each energy so that for the majority of the experiment the beam energy used produced the optimum cross section for ^{192}Po. The measured yield, Y, in the beam off periods is related to the cross section by the formula

$$Y = \frac{3759}{M_T} I\ t\ \tau\ \epsilon\ \sigma\ \alpha \tag{4.5}$$

where M_T is the target mass number (=160), I the beam intensity in particle nanoamps, t the time in seconds, τ the target thickness in mg cm^{-2}, ϵ the total efficiency, σ the cross section in mb and α (=67%) is the target purity. The total efficiency is defined as the product

$$\epsilon = \epsilon_D\ \epsilon_R\ \epsilon_C\ \epsilon_P \tag{4.6}$$

where ϵ_D is the full-energy detection efficiency (55%), ϵ_R the transmission efficiency of RITU (20%), ϵ_C the collection efficiency (70%) which takes into account the focal plane coverage and ϵ_P a factor used to account for the beam pulsing (ϵ_P = 50%). This gives a total efficiency of 3.9%. Inputting the known values into equation 4.5 and rewriting gives

$$\sigma = \frac{3.26\ Y}{I\ t}. \tag{4.7}$$

The cross sections at each energy are summarised in table 4.2.

Theoretical 0^+ excitation energy levels			
Beam energy (MeV)	Beam intensity (pnA)	Yield	Cross section (μb)
172	37.5	4716	8.0
176	30	3897	7.3
180	38	2851	6.2
184	40	1595	3.4

Table 4.2: Cross sections at front of target.

Chapter 5

Observation and Properties of the Fine Structure

5.1 PAD-quadrant Coincidences

A raw implantation energy spectrum, as shown in figure 5.1, requires that only a single coincidence be observed between the implantation detector and any of the quadrant detectors. The background is high due to α-particle escapes from the implantation detector and the presence of low energy β particles. However, even in this spectrum there appears to be a peak. The following sections will discuss how the high background shown in figure 5.1 can be reduced by applying energy and time conditions.

5.1.1 Time Gating

Isotopic contaminants of the ^{160}Dy target give rise to large yields of the heavier α-emitting polonium isotopes (see figure 4.3). Enhancing the ratio of the yield of ^{192}Po decays relative to those of the heavier isotopes will help to suppress the background when looking for the fine structure lines by the coincidence technique. This may be achieved by applying restrictions on the recorded time difference between the clock

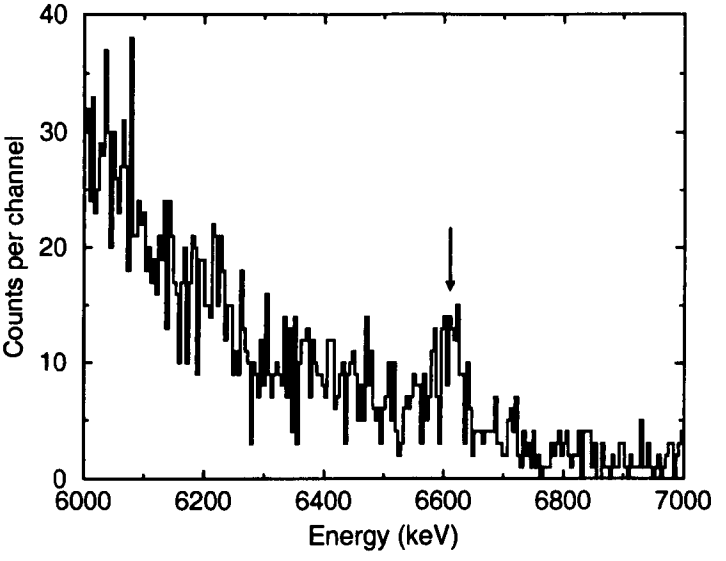

Figure 5.1: On-line coincidence spectrum between the implantation and quadrant detectors, with no gating conditions. The α line corresponding to α decay to the lowest excited state in ^{188}Pb is marked with an arrow.

reading of the time of occurrence of a decay event and its correlated recoil partner. Isotopes furthest from stability will have shorter half-lives than their more stable counterparts. As an example the half-life of ^{194}Po, which is produced with much higher yields than ^{192}Po in the reaction, has a half-life of 392 ± 4 ms [Wa93]. The half-life of the ^{192}Po ground state line has been previously measured as 33.2 ± 1.4 ms [Bi96], so statistically it would be less likely to observe decay events with time intervals longer than 200 ms, relative to ^{194}Po. However, in this scenario only a fraction of ^{194}Po events would be observed. This effect can be seen in figure 5.2, for events in beam off periods only.

The production of the long-lived bismuth isotopes is reduced by a factor of approximately four. More importantly, however, is the relative production of ^{192}Po to the heavier polonium isotopes. The measured yield of ^{192}Po remains fairly constant after introducing the 200 ms time gate. However the yield of ^{194}Po falls to 46% of its original value, similarly the yields of ^{195,196}Po fall to 30% and 27% respectively

of their original values. Hence, the time gate reduces the background from escaping α-particles in the region of the fine structure peaks.

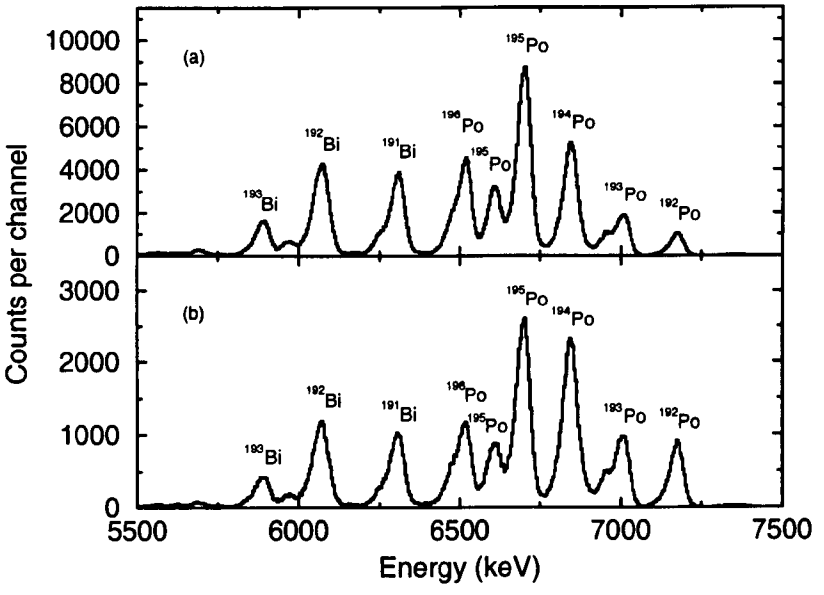

Figure 5.2: Alpha-energy spectra in beam off periods only (a) with no time condition applied and (b) with a 200 ms time gate applied.

5.1.2 Quadrant and Addback Gating

Most of the α particles that escape from the implantation detector have higher energies than the conversion electrons of interest, so it is possible to gate them out. Figure 5.3 shows the α-particle escapes and β particles observed in the quadrant array. Selecting a low-energy gate greatly reduces the number of α-particle escapes and the low energy β particles can be suppressed with a time gate. The electron energy gate of 0 to 1 MeV was set according to half-life calculations [Ra59] which indicate that any 0^+ levels emitting electrons with energy above 1 MeV would not be populated with measurable intensity in the experiment. An additional gating condition is applied when the summed addback of the α particle and conversion electron energies approximately equals that of the ^{192}Po ground state line, in order to reduce the background further. The broad energy gate is necessary for various reasons

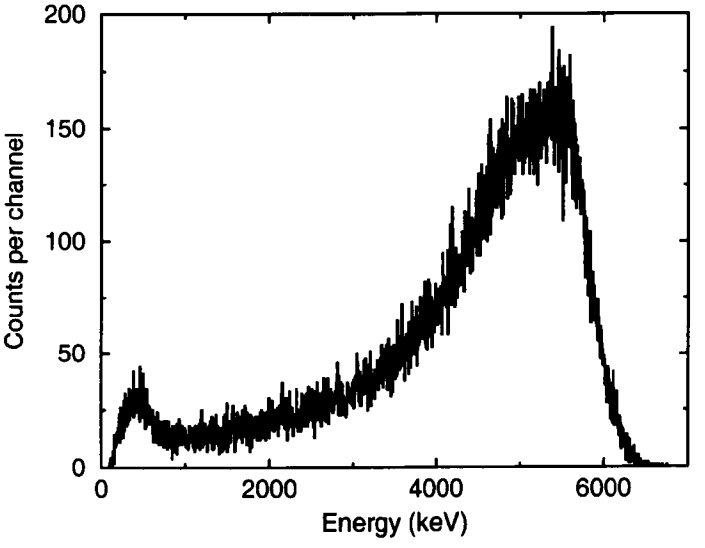

Figure 5.3: Energy spectrum for the summed segments of the quadrant array.

- there is a significant probability that the electrons will either penetrate through the detector or be scattered backwards out of the detector, both resulting in a reduced energy signal in the detector array
- one has to allow for the initial atomic binding energy of the emitted electron, which is not usually registered and also the possibility of electron emission from different shells
- the poor resolution of the electron detectors.

A quadrant and addback gated spectrum is shown in figure 5.4. No beam phase condition has been applied because the α-particle/electron coincidence requirement is sufficient to remove the beam related background.

5.1.3 Identification of the 0_2^+ Oblate State

Incorporating the electron energy gating conditions a clear line can now be observed in figure 5.4. A least-squares skewed Gaussian peak fit was performed for the ground-state to ground-state ^{192}Po α decay. The shape parameters from this fit were then

used to fit this new line by means of the maximum likelihood fitting technique [Me75] [Sc84], as displayed in figure 5.5. The centroid was determined at an energy of 6613 ± 7 keV, the area of the peak being 68 ± 9 counts after an allowance is made for background. The measured energy has been corrected to take into account pulse height defects, but an allowance also has to be made for electron energy summing, which is described in more detail in section 5.2.2.

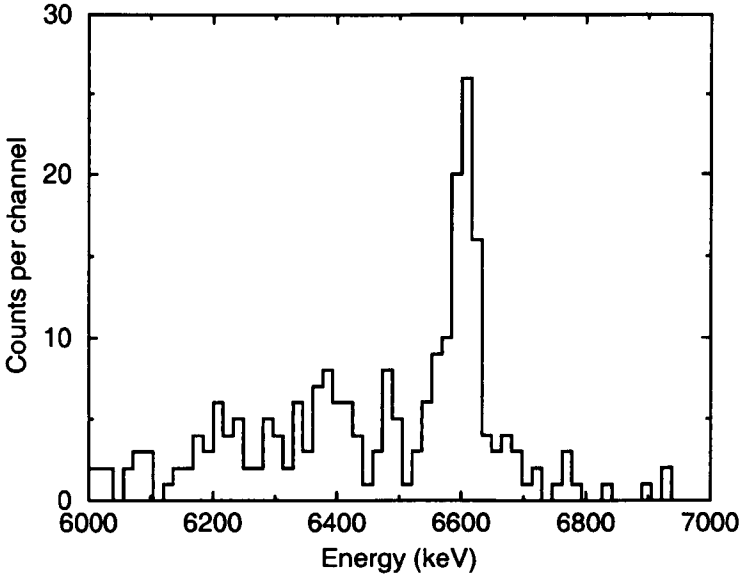

Figure 5.4: Energy spectrum of α-decay events observed in the implantation detector in coincidence with an event in the surrounding array of quadrant detectors. Additional gates have been placed on events that occur in the energy region where electrons accompanying decay to the fine structure of interest would occur.

The excitation energy of the level is therefore deduced to be 570 ± 4 keV relative to the ground state. This is in reasonable agreement with the value of 590 keV extrapolated from the level energies of previously observed 0^+ oblate states in the heavier lead nuclei. The half-life of this line has been measured by fitting a time difference spectrum of the correlated recoil and decay events, as shown in figure 5.6. A maximum likelihood fit [Me75] [Sc84] has once again been performed.

The shape of the exponential decay can be seen despite the low number of counts and the measured value of 31 ± 4 ms is in good agreement with the literature value

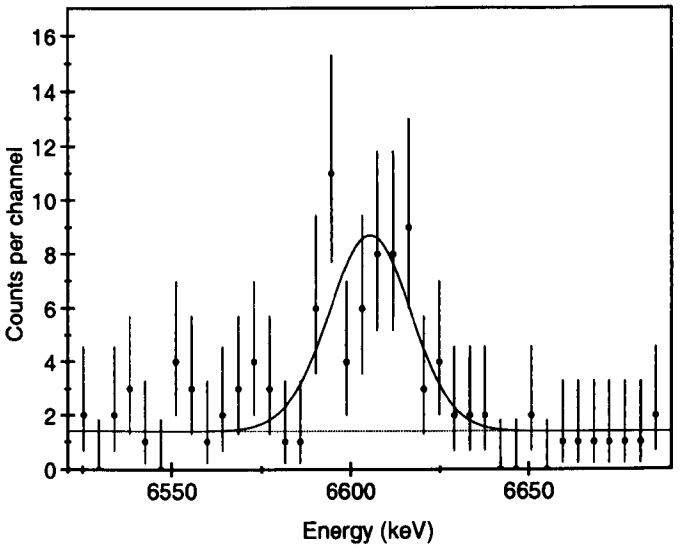

Figure 5.5: Maximum likelihood fit performed for the proposed 0_2^+ oblate α-line.

of 33.2 ± 1.4 ms for the ground state ^{192}Po line [Bi96]. On the basis of the good agreement of the half-life with the previously measured value and with the energy systematics of the heavier lead isotopes, this line has, therefore, been assigned as the decay to the 0^+ oblate state in ^{188}Pb.

In the time since the experiment was performed Bijnens *et al.* have reported the observation of 5 events at an energy of 6610 ± 30 keV produced in the same reaction [Bi96]. In their experiment the FMA at the Argonne National Laboratory was used to separate A=192 reaction products and they similarly interpreted the decay as α decay to the oblate state in ^{188}Pb.

5.1.4 Granularity of the Electron Detectors

It is hard to see any evidence from figure 5.4 for an α-peak at an energy of around 6.4 MeV, representing decay to the expected prolate 0^+ bandhead. However, the background arising from escaping α particles in this energy region is significant and could swamp a small peak. Decay to the prolate state would be less favourable than to the oblate state because it is higher in excitation energy. The segmentation of

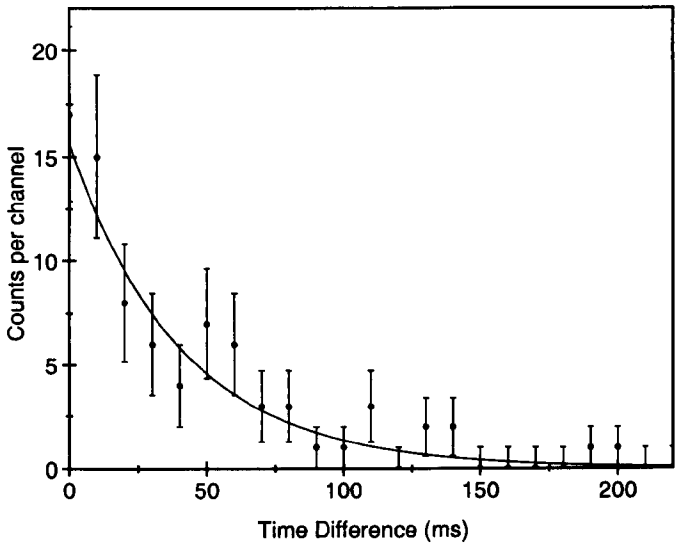

Figure 5.6: Time difference spectrum between recoil and decay events associated with ^{192}Po α-decay events, shown in the time interval 0 to 220ms. The maximum likelihood fit was performed over a much larger time interval.

the quadrant detector array becomes important when attempting to reduce further the background arising from α-particle escapes. The quadrant detector array can be split into 2 rings, according to the height of the individual elements above the implantation detector: a lower ring comprising 12 elements closest to the surface of the implantation detector covering height 0 to 25mm and an upper ring comprising the remaining 12 elements covering 25 to 50mm. The segmentation of the detector is represented schematically in figure 5.7.

The shallower angle of α-particle emission required to detect the escaping α particle in the lower ring of quadrants implies that the α particle will lose more energy as it travels through a larger effective thickness of silicon, compared to an α particle detected in the upper ring of quadrants. These α particles will therefore emerge from the implantation detector with low energies, thereby satisfying the energy condition applied in software to the electron detector signals. This will lead to a background that increases with decreasing energy in the implantation detector, in the energy range of interest, as is observed in figure 5.1. Since ^{192}Po α decays contribute

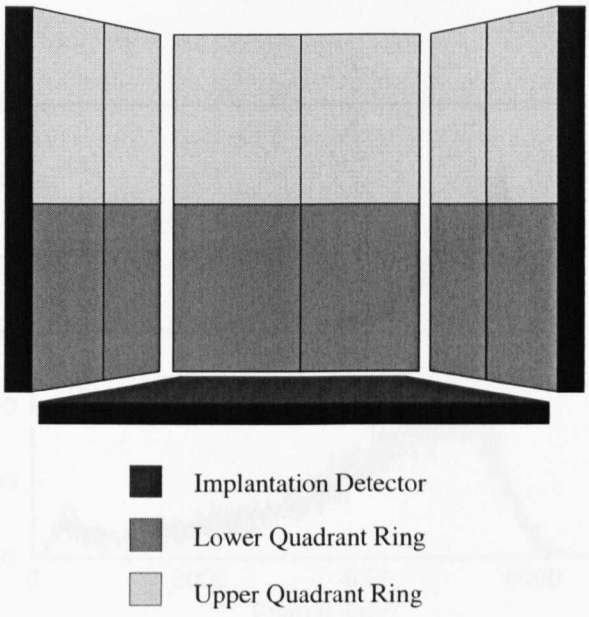

Figure 5.7: Slice through the quadrant detector array showing the segmentation of the array into the upper and lower rings.

strongly to this background, more stringent time gating does not significantly improve this spectrum. Figure 5.8 shows the energy spectra recorded separately for the two rings in coincidence with events occurring in the implantation detector within 200 ms of the arrival of an ion at the same (x, y) position. It is evident that the distribution of α-particle energies extends to much lower values for the lower ring than for the upper ring.

Since the condition applied to the electron detector signals requires that the energy is $\lesssim 1$ MeV, this suggests that the α-particle escapes detected in the lower ring are mainly responsible for the background observed in the corresponding coincident α-decay spectra. However, the reduction in background associated with taking upper ring coincidences only is accompanied by a loss in electron collection efficiency and hence a loss of yield in the α peaks.

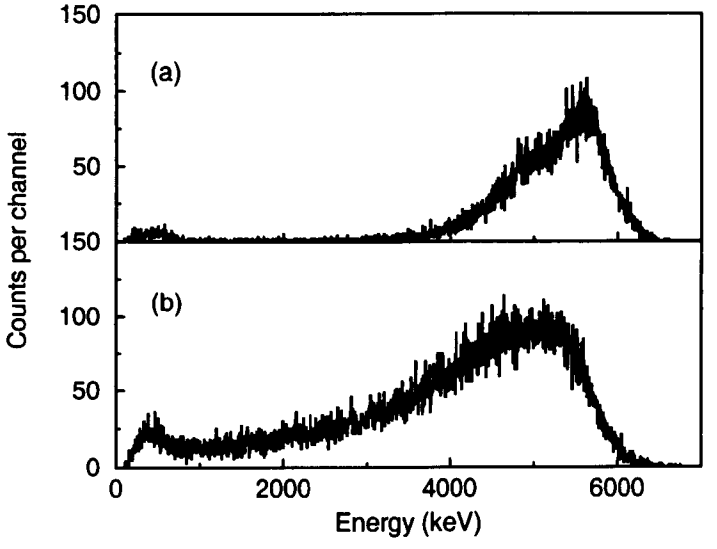

Figure 5.8: Distribution of escaping α particles recorded in the upper (a) and lower (b) rings of the silicon detector array.

5.1.5 Identification of the 0_3^+ Prolate State

The spectrum shown in figure 5.9(c) has the same gating conditions as previously described, but now additionally requires that the electron coincidence should be recorded in only the upper ring of the electron detector array. This spectrum is shown in comparison with the beam off, time-gated spectrum with no quadrant coincidence (a) and also the coincidence spectrum with both quadrant rings used (b).

A second α peak, containing 13 counts, is now clearly evident at an energy of 6418 ± 13 keV with a greatly reduced background (the maximum likelihood fit is displayed in figure 5.10). The excitation energy of this level is then 765 ± 12 keV and is consistent with the extrapolated position of the prolate bandhead in the rotational band observed by Heese *et al.* [He93], so this line is therefore assigned as the α decay to the prolate 0_3^+ state. Performing a maximum likelihood fit to the time difference spectra, in a similar fashion as for the previously assigned oblate state, a half-life of 59 ± 17 ms was recorded. This is still consistent with the known half-life for ^{192}Po.

There is no evidence for the existence of an α line at an energy of 6.46 MeV which

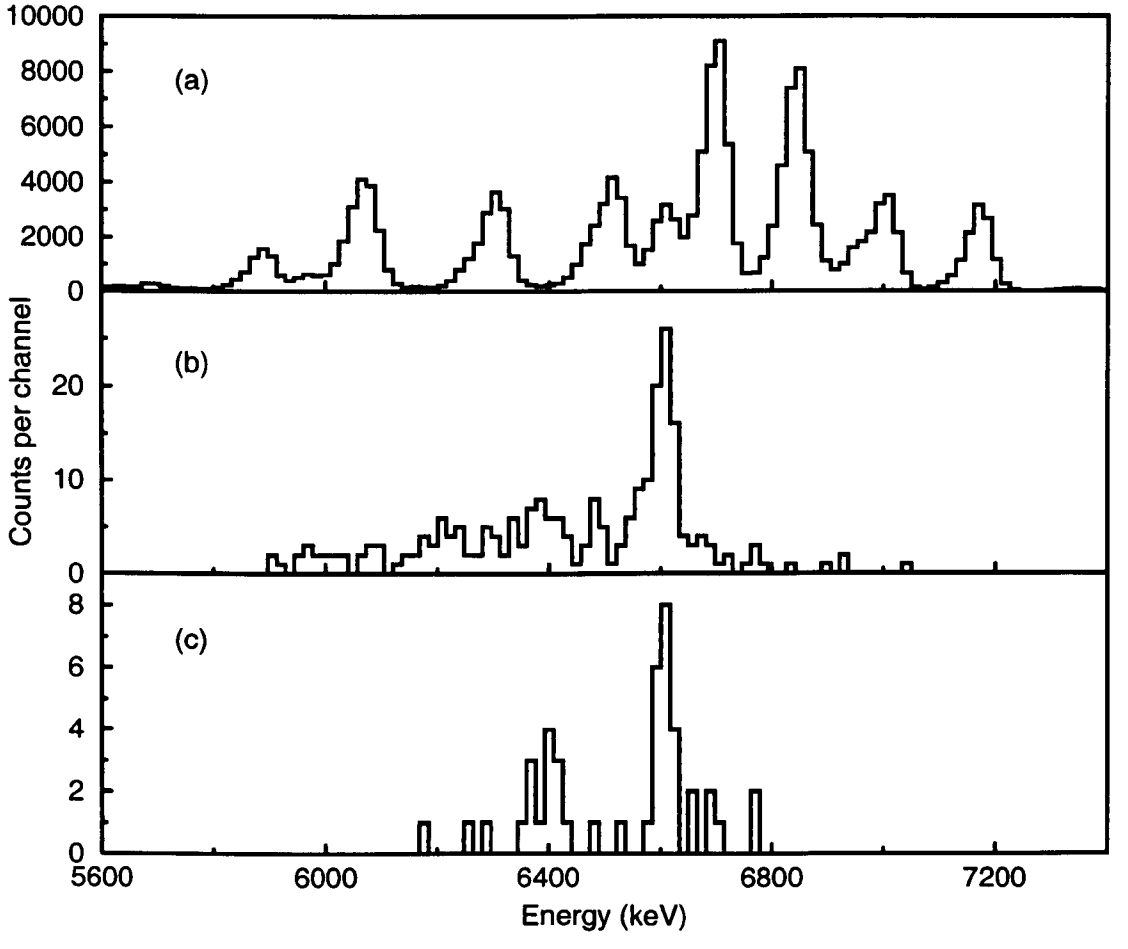

Figure 5.9: Alpha-decay energy spectra with progressive gating conditions applied. Spectrum (a) shows the full energy α lines observed in beam off periods. Spectrum (b) has no beam phase condition, but requires an electron coincidence with energy gates applied. Additionally, spectrum (c) requires that the electron coincidence must be observed in the upper ring of the electron detector array. All spectra have a 200 ms time-gate applied.

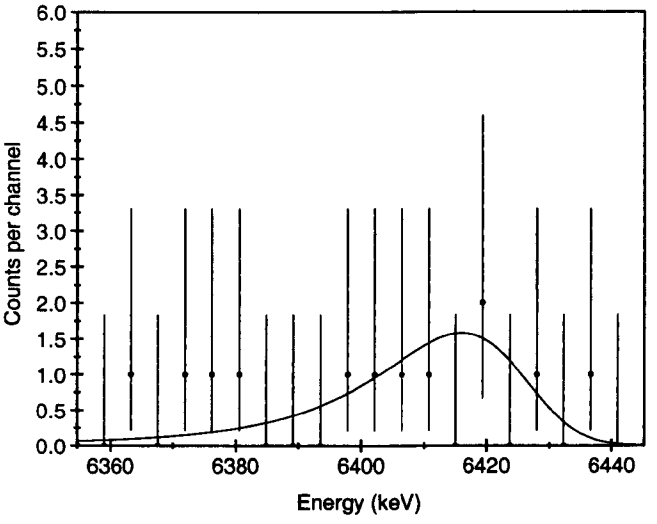

Figure 5.10: Maximum likelihood fit performed for the proposed 0_3^+ prolate α line.

would correspond to decays to the previously observed 2^+ level at 724 keV in ^{188}Pb. Although from α-decay calculations it may have been expected to observe around 20 counts in this peak, its absence can be explained due to the inability of the electron detectors to record the high-energy γ rays that the state would predominantly decay by. This supports the assignment of the 6.4 MeV and 6.6 MeV lines as the decays to 0^+ states which decay by conversion electron emission.

5.2 Monte Carlo Simulations

In general a Monte Carlo technique is any technique that makes use of random numbers to solve a problem. More specifically, it represents the solution of a problem as a parameter of a hypothetical population. Using a random sequence of numbers to construct a sample of the population, statistical estimates of the parameter can then be obtained. The Monte Carlo method may be applied wherever it is possible to establish equivalence between the required result and the expected behaviour of a stochastic system. In this instance it is used to model an initial distribution of electrons in the surrounding detector array.

MCNP (Monte Carlo N-Particle) [Br97] is a general code that can be used to model particle transport. The precise geometry of the detector array was defined in three-dimensional space and programmed into the calculations. An electron source distribution was defined over the implantation detector and was determined from the ^{192}Po ground-state to ground-state α-decay position distribution, shown in figure 5.11. The distribution over the x-direction (the eight strips) was taken to be flat, which is a reasonable approximation (one of the contacts on strip number two was faulty which meant half of the data from that strip were lost). In the y-direction a Gaussian distribution was fitted to the data and the probability of an event occurring at a certain position was defined in discrete bin intervals along each strip in the MCNP code. The energy resolution of the implantation detector (48 keV) was also set in the code. A typical MCNP input file is given in Appendix A.

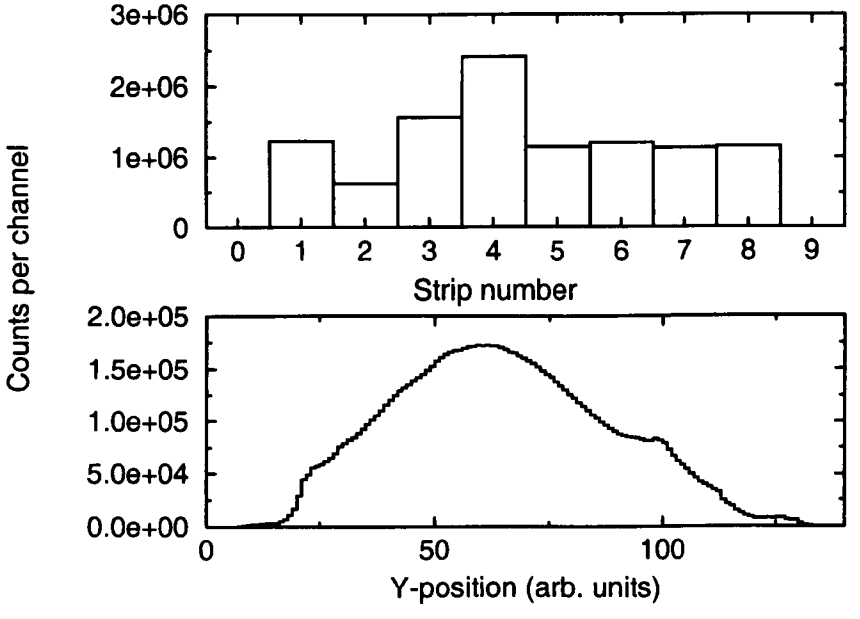

Figure 5.11: The upper section reflects the x-distribution of α particles detected in the implantation detector whilst the lower section gives the y-position information of the α particles in the implantation detector.

5.2.1 Electron Detector Efficiency Measurement

In order to calculate the electron detector efficiencies it is necessary to model the electron transport; this was done using the MCNP code. The geometrical efficiency of the electron detector array can be determined from the ratio of the number of α-particle escapes detected in each segment of the electron detectors to the total that deposit their full energy in the implantation detector, with the same conditions applied. This would give a value for the geometrical efficiency of each segment, enabling a value to be determined easily for the upper and lower rings separately. However, the threshold above noise was set experimentally and determined to be around 200 keV on average. So, to obtain the total collection efficiency MCNP was used to model the electron energy distribution in each of the individual elements. In this way the ratio above threshold to the total could be obtained.

The average implantation depth was calculated from the number of α particles that escaped without depositing their full energy, using the equation

$$\epsilon = \frac{1}{2}\left(1 - \frac{Z}{R}\right) \tag{5.1}$$

where ϵ is the efficiency for full energy collection (55%), Z the implantation depth and R the average α-particle range in silicon (for the nuclei produced in the reaction $\sim$ 37 microns). The value of Z was determined to be 5.8 ± 0.5 μm, which is consistent with the value estimated using the code TRIM [Zi85]. The uncertainty on the depth also includes a contribution from the calculated longitudinal straggling. The resolution of the electron detectors also had to be inputted into the calculations. A value of 114 keV was inferred by measuring the FWHM of the ^{192}Po ground-state to ground-state line in the addback spectra, with the resolution of the implantation detector already known.

MCNP was run with the electron distribution in each strip of the implantation detector separately. For each run the total number of histories was kept at a constant value of 50,000. The spectra for each of the eight strips were then summed to produce electron energy spectra in each quadrant of the array and this was done separately for

both conversion electron energies corresponding to both the decays from the prolate and oblate states. In both cases it was assumed that the decays directly populate the ground state. One also has to take into account the atomic electron binding energies which would not be recorded by the electron detectors. Emission is assumed to come from the lowest orbital K shell, which is ~5.5 times more probable than emission from the next lowest-lying L shell [Ka95]. The values for the decays from the prolate and oblate states were 679 keV and 480 keV respectively and were inferred from the observed corresponding α-particle energies. Example spectra produced by MCNP are shown in figures 5.12 and 5.13. These illustrate the two cases of all strips summed for one quadrant (upper ring (a), lower ring(b)) of the electron detector array, for the 480 keV and 679 keV conversion electrons respectively.

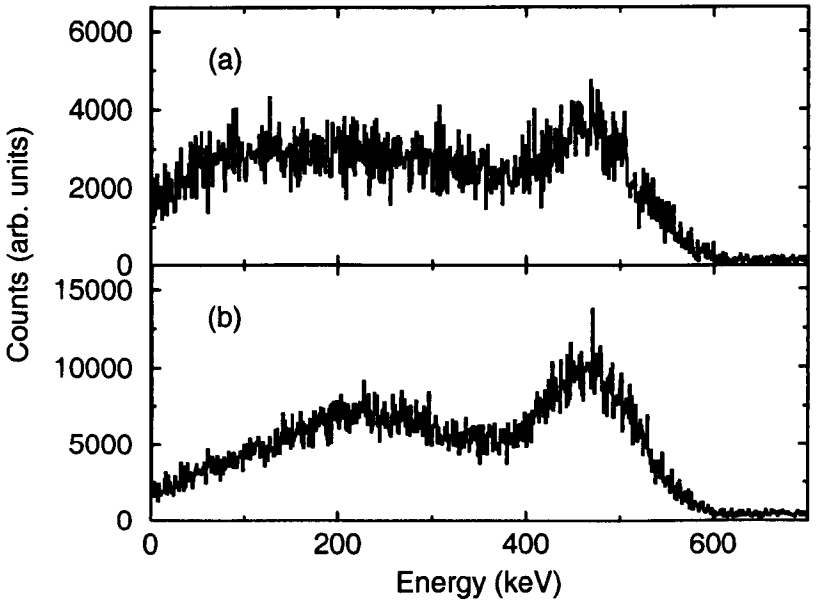

Figure 5.12: Predicted electron energy spectra in (a) an upper ring segment of the quadrant array and (b) a lower ring segment of the quadrant array, for an initial distribution of 480 keV electrons in the implantation detector.

Both of these cases indicate that only a small percentage of the full electron energy will be deposited in the quadrant detector array. Therefore it is difficult to set tight energy gates on the electron in these detectors. This augments the case for taking

upper ring coincidences only, as it has already been discussed that the background from α escapes is lower gating on this energy range in the upper rather than the lower ring.

The quadrant detector efficiencies were calculated by taking the product of the geometrical efficiencies (from the α escapes) and the threshold efficiencies (calculated from the MCNP data). The overall efficiency of the electron detector array was calculated to be 18.0% (lower ring 12.2%, upper ring 5.7%). Therefore any reduction in the level of background by taking upper ring coincidences only will be accompanied by a loss of approximately a factor of 3 in the total yield.

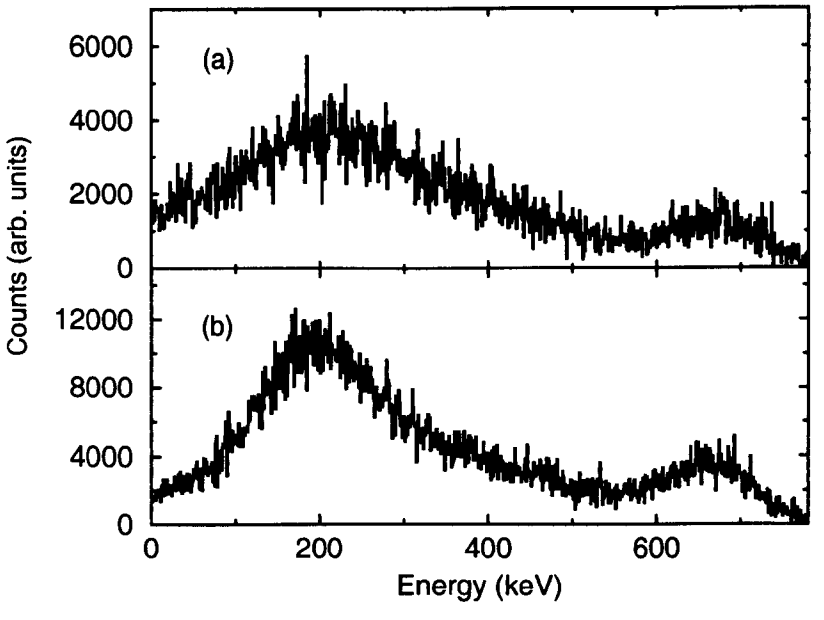

Figure 5.13: Predicted electron energy spectra in (a) an upper ring segment of the quadrant array and (b) a lower ring segment of the quadrant array, for an initial distribution of 679 keV electrons in the implantation detector.

5.2.2 Electron Energy Considerations

The energies measured for the α-decay fine structure lines need to be corrected for the energy deposited in the implantation detector by the electrons as they proceed along

their path to the electron detectors. Once again the MCNP program is used, defined with the same initial parameters as previously described, except in this case the electron detectors are designated an infinite detector resolution. The energy detected by them will be the full energy minus that which is lost in the implantation detector, which can therefore be deduced. MCNP did not allow this to be done directly. The spectra shown in figure 5.14 are for a source of 679 keV electrons defined over strip 1 of the implantation detector.

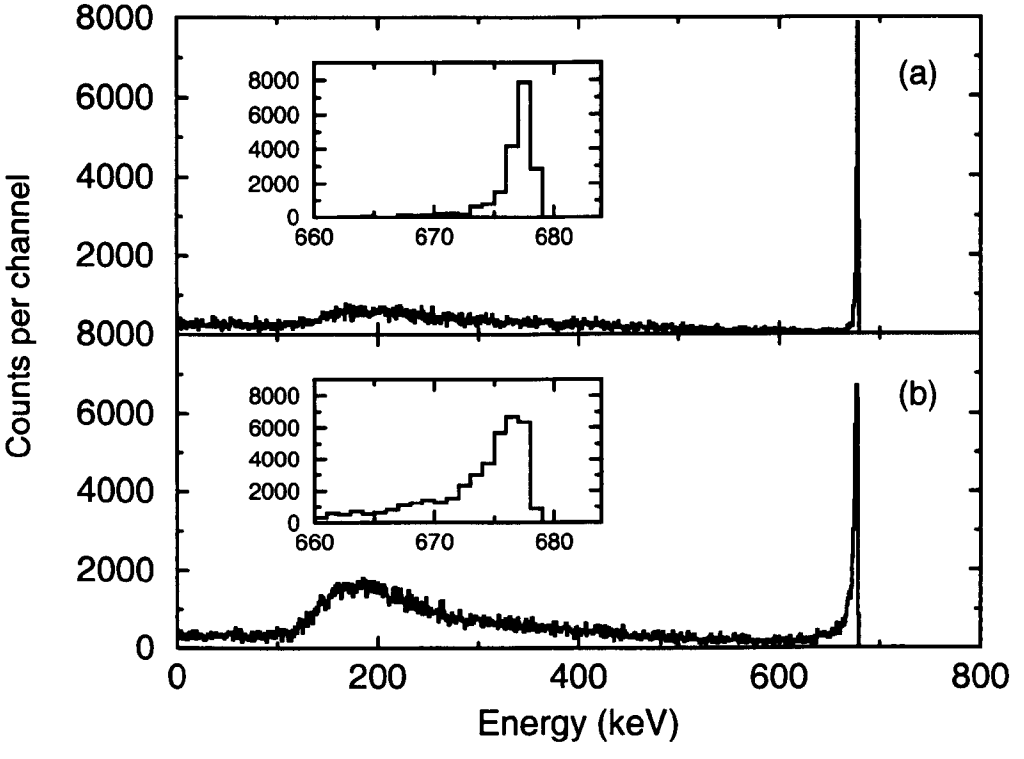

Figure 5.14: An example of energy spectra produced in the quadrant detector array, calculated by MCNP for a distribution of 679 keV electrons within the surface of an implantation detector with infinite resolution. Section (a) shows the results in the upper ring of the detector array and (b) for the lower ring. The inserts show the peaks on an expanded scale, highlighting a larger energy loss (broader distribution) for the lower ring only.

The Monte Carlo simulations were performed for both electron energies (upper and lower rings for the 480 keV electrons, upper ring only for the 679 keV electrons) and

the corresponding energy losses were found to be 1.8 keV and 2.6 keV, respectively. Two important deductions can be made from the spectra in figure 5.14; the observed distribution in the lower ring of the detector array contains a higher background at lower energies than observed in the upper ring and it is also important to note the broader distribution of the full energy peak in the lower ring implying a larger energy loss on average than for the upper ring.

In the case of decay from the prolate state more careful consideration is required because there is a possibility that this state could decay via the lower-lying oblate state rather than directly to the ground state. In this scenario a cascade of ~110 keV and 480 ± 4 keV electrons would accompany the α particle, again assuming K shell emission. However, any electron-electron coincidence method to resolve this is impossible due to the low level of statistics and in any case the electron detector threshold of ~200 keV is above the value of 110 keV for electrons emitted in the decay between the two excited 0^+ states. E2 γ decay to the lowest-lying 2^+ level at 724 keV would be expected to be insignificant compared with these E0 conversion electron decays and is neglected. The electron energy spectra incremented by gating on the fine structure peaks are shown in figure 5.15.

The form of the observed 480 keV electron energy spectrum (figure 5.15(a)) is in reasonable agreement with that observed in the Monte Carlo simulations shown in figure 5.12, when considering both the upper and lower rings of the quadrant detector. The MCNP simulations for the 679 keV electrons indicate that the majority of the electrons give rise to signals in the continuum region, rather than the full energy peak, resulting in an essentially flat electron energy spectrum. The spectrum of electron energies observed in coincidence with the 6.4 MeV line is shown in figure 5.15(c). This spectrum appears to have the same flat distribution although it is impossible to draw reliable conclusions because of a lack of statistics. Along with the given poor resolution of the electron detectors it is difficult to say whether the decay from the prolate state is a one or two-step process. However, in the case where two electrons are emitted and the 480 keV electron is detected there is a roughly equal probability the

110 keV electron partner will either be fully absorbed in the implantation detector and adding to the α-particle signal, or of escaping with a minimal energy loss. Thus one would expect to observe two α-particle groups, separated by approximately 110 keV in figure 5.9(c). There are two events around 6.5 MeV, which is consistent with the level of background from escaping α particles, suggesting the prolate level decays directly to the ground state. In this case applying the MCNP corrections to the measured α-lines the energies for the decays to the oblate and prolate 0^+ levels are now 6611 ± 7 keV and 6416 ± 13 keV respectively, corresponding to levels at excitation energies of 568 ± 4 keV and 767 ± 12 keV.

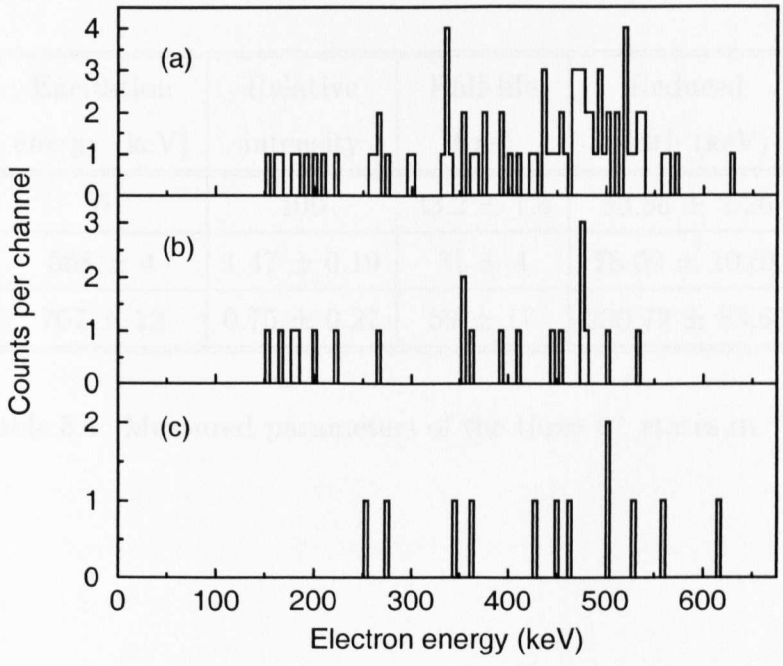

Figure 5.15: Observed electron energy spectra in coincidence with the α particles in (a) the 6.6 MeV line in figure 5.9(b), (b) the 6.6 MeV line in figure 5.9(c), the 6.4 MeV line in figure 5.9(c).

5.3 Branching Ratios and Hindrance Factors

The peak areas were obtained from the maximum likelihood fits [Me75] [Sc84] that were performed. Correcting for the electron and α-particle detection efficiencies it was then possible to obtain the expected yield in each of the α-decay peaks. The branching ratios can then be deduced by taking each yield relative to that of the ground state line. The FORTRAN program REDWID [Pa90] was used to calculate the reduced α-decay widths. The ratio of the width to the ground state to that of the decay to an excited 0^+ state then gives the reduced hindrance factor. The properties of the decays to each of the 0^+ states are summarised in table 5.1.

	Excitation energy (keV)	Relative intensity	Half-life (ms)	Reduced width (keV)	Hindrance factor
Spherical	0	100	33.2 ± 1.4	53.56 ± 2.26	1
Oblate	568 ± 4	1.47 ± 0.19	31 ± 4	78.02 ± 10.61	0.69 ± 0.10
Prolate	767 ± 12	0.75 ± 0.27	59 ± 17	230.72 ± 83.63	0.22 ± 0.08

Table 5.1: Measured parameters of the three 0^+ states in ^{188}Pb.

Chapter 6

Discussion

6.1 Band Mixing Calculations

6.1.1 Level Energies

The newly observed 0^+ levels of this work are shown along with the positive parity levels from Heese *et al.* [He93] in figure 6.1. These levels were then reproduced in band mixing calculations that have been performed in order to extract the mixing strengths between the observed levels and also the unmixed (pure) level energies. The procedure followed was that of Dracoulis [Dr94] who used mixing calculations to reproduce experimental level-energies and then to examine the properties of the unperturbed bands so deduced.

The energies of the pure oblate and prolate states were calculated within the variable moment of inertia (VMI) model, while the energies of the spherical states, which do not follow a rotational pattern, were allowed to vary freely. The states from all three structures were allowed to mix [Hey94] assuming spin independent interactions. The parameters were then adjusted using a least-squares procedure until the mixed level energies so calculated reproduced the experimental level scheme. The unmixed and the as yet unobserved levels are shown by the dotted and dashed lines respectively in figure 6.1.

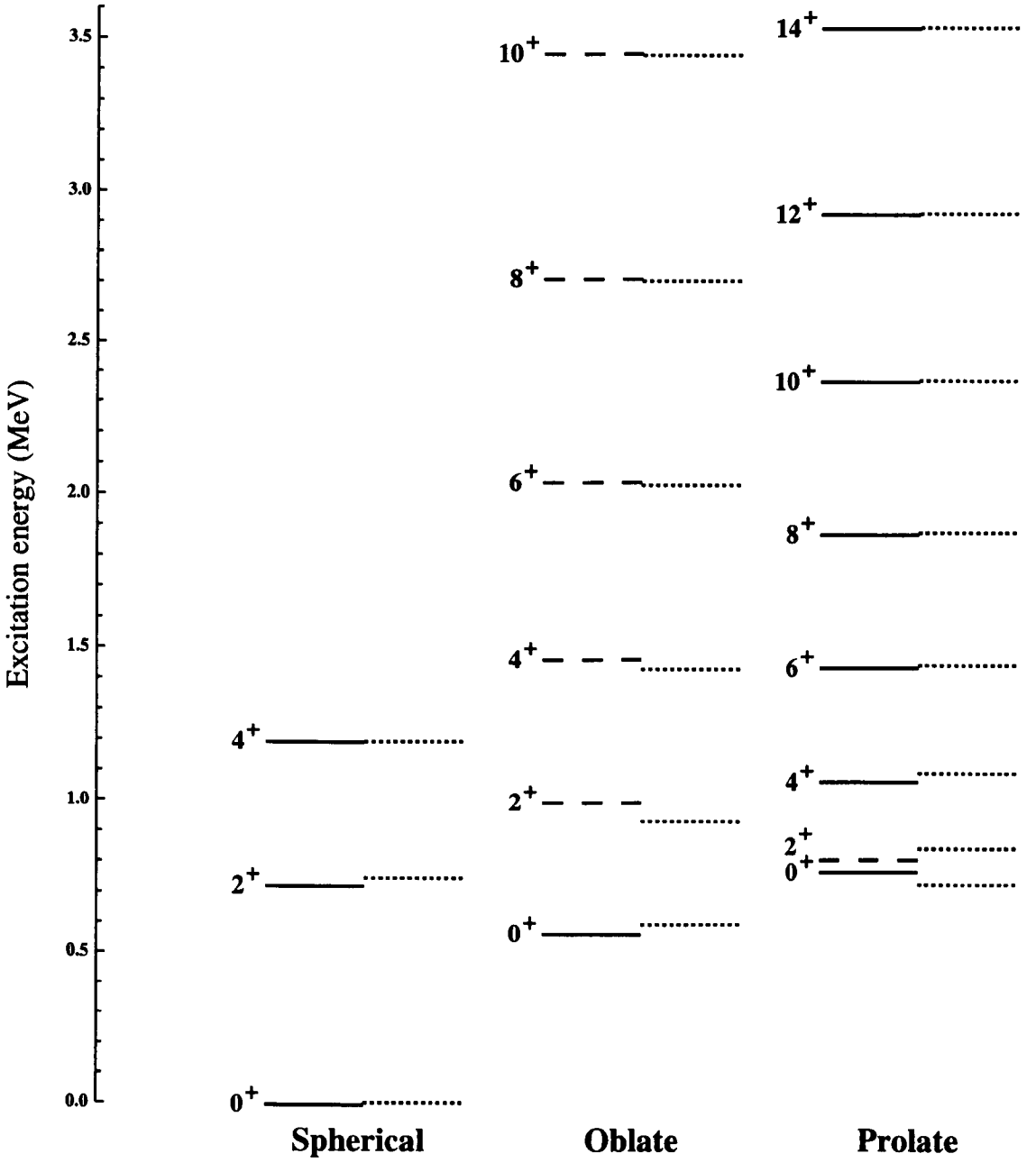

Figure 6.1: Partial level scheme for ^{188}Pb showing levels up to spin $14\hbar$. The solid lines represent the levels observed in this work and also those from ref. [He93]. The estimated energy of unknown levels (dashed lines) and the unmixed level energies (dotted lines) are extracted from the band mixing calculations. The levels have been separated according to their shape configuration.

Table 6.1 summarises all the level energies outputted from the band mixing calculations, the values in bold indicating the observed levels.

	Mixed			Pure		
Spin	Spherical	Oblate	Prolate	Spherical	Oblate	Prolate
0	**0.0**	**568.0**	**766.9**	7.7	600.3	726.9
2	**723.9**	997.8	808.0	749.5	936.1	844.1
4	**1196.1**	1462.9	**1064.7**	1198.0	1432.5	1093.2
6		2039.7	**1435.0**		2030.7	1444.0
8		2713.1	**1869.3**		2706.7	1875.7
10		3451.8	**2369.2**		3446.8	2374.2
12		4246.2	**2926.0**		4242.1	2930.1
14		5089.7	**3532.8**		5086.2	3536.3
16		5977.3	**4184.5**		5974.3	4187.5

Table 6.1: Level energies extracted from the band mixing calculations. Observed levels are shown in bold.

It can be seen from figure 6.1 that all the levels observed by Heese *et al.* [He93] are yrast except for the weakly populated 4_2^+ (spherical) level. Another interesting feature that can be inferred from the level scheme is that in the absence of any mixing the three states lowest in energy would all be 0^+ states, with the lowest lying 2^+ state approximately 20 keV higher in energy than the prolate 0^+ bandhead. The mixing calculations also predict that the mixed prolate 2^+ state is almost degenerate with this bandhead.

The spherical 0^+ state is only slightly displaced by mixing with the other two 0^+ states, whilst the results for the unmixed bandheads agree well with the extrapolations described in section 2.2. The unmixed prolate bandhead has been calculated at an excitation energy of 727 keV compared to the extrapolated value from the prolate rotational band of ~710 keV. Similarly, the pure 0^+ oblate level is calculated at

600 keV compared to ~590 keV from extrapolating the systematics of the same states in the heavier lead isotopes.

In section 2.2.1 two empirical methods were described in which the energy of the 2p-2h oblate 0^+ state can be estimated by reproducing the systematic behaviour of previously observed oblate 2p-2h states. The first prescription described was based on the observation that the energy of the 2p-2h level for a given lead nuclide shadowed the sum of the intruder $\pi s_{1/2}$ and $\pi h_{9/2}$ levels in the bismuth and thallium isotopes. The resulting value of ~667 keV is significantly larger than predicted by the current calculations, but it is interesting to note that the intruder energy systematics for bismuth and thallium diverge at N=106 [Co85] [Ba95] indicating that this scheme may indeed fail in the case of ^{188}Pb.

The second scheme exploited the linear dependence of the excitation energy on a factor related to the number of valence protons and neutrons. Here, a predicted value of ~540 keV is in reasonable agreement with the measured excitation energy of the oblate level. However, a corresponding fit for the unmixed level energies gives a similar result which deviates further from the unmixed energy deduced in this work.

6.1.2 Mixing Strengths

The mixing calculations can also provide estimates of the strength of the mixing between the three levels. Essentially the eigenvalue equation defined in equation 1.30 has been solved, the results of which yielded the following values

$$V_{op} = 73 \pm 13 \text{ keV}$$
$$V_{sp} = 52 \pm 3 \text{ keV}$$
$$V_{so} = 54 \pm 9 \text{ keV}$$

for the mixing between the oblate and prolate (V_{op}), spherical and prolate (V_{sp}), spherical and oblate (V_{so}) levels, respectively. The error bars on the mixing strengths were deduced by running the band mixing calculations for energy levels that had been shifted to the upper and lower limits of the errors on the prolate and oblate 0^+ level

energies. Applying the VMI description and assuming spin-independent interactions implies that these error bars are only applicable within the model.

The results achieved are in good agreement with the neighbouring lead isotopes. The prolate-spherical mixing strength has previously been extracted from the level scheme of ^{186}Pb [Dr94], yielding a value of 44 keV, while lifetime measurements of E0 transitions in ^{192,194}Pb gave oblate-spherical mixing matrix elements of 51 keV and 52 keV respectively [Den89]. However, in the case of ^{190}Pb only a lower limit of 80 keV was deduced for the corresponding matrix element, so it would be of interest to investigate this value further. Extending the comparison to the corresponding configurations in the mercury and platinum nuclei [Dr94] [VD90] the matrix elements are rather larger than the value of 80 keV for ^{190}Pb.

6.1.3 Mixing Amplitudes

The mixing amplitudes of different configurations are calculated from equation 1.28. Written in full the matrix equation to be solved is

$$\begin{vmatrix} H_{11} & H_{12} & H_{13} \\ H_{21} & H_{22} & H_{23} \\ H_{31} & H_{31} & H_{33} \end{vmatrix} \begin{vmatrix} a_m \\ b_m \\ c_m \end{vmatrix} = E_m \begin{vmatrix} a_m \\ b_m \\ c_m \end{vmatrix} \tag{6.1}$$

where a_m, b_m and c_m are the amplitudes in the spherical, oblate and prolate 0^+ levels respectively, the subscript $m = \mathrm{s, o, p}$ defining the amplitude of each configuration in each specific level. The admixtures easily follow as the squares of the amplitudes for each configuration in each state and the sum of the wavefunction admixtures for the spherical, oblate and prolate configurations for each state should be equal to 1. The admixtures calculated from the band mixing are given in table 6.2.

The extracted mixing amplitudes for the 0^+ states can be combined with measured α-decay hindrance factors, in order to infer the degree of mixing in the parent and daughter nuclides. Extending the formalism described in section 1.3.1, the two-level model can now be extended to encompass the mixing of the three levels in ^{188}Pb.

	Spherical |0p-0h>	Oblate |2p-2h>	Prolate |4p-4h>
0_1^+	98.9%	0.7%	0.4%
0_2^+	0.2%	78.6%	21.2%
0_3^+	0.9%	20.7%	78.4%

Table 6.2: Admixtures of each configuration in each of the three 0^+ states.

The wavefunction amplitudes for the levels defined in ^{192}Po, ^{188}Pb and ^{184}Hg are now illustrated in figure 6.2. In the case of ^{192}Po the total ground-state wavefunction is described as the sum of a certain admixture **d** of the normal state wavefunction $|\mathbf{u}>$ and an admixture **e** of the intruder wavefunction $|\mathbf{v}>$. The intruder level wavefunction is then described by interchanging the admixtures to the opposite wavefunctions for each unmixed level. In a similar fashion the two levels in ^{184}Hg are described by the normal and intruder wavefunctions $|\mathbf{x}>$ and $|\mathbf{y}>$ and admixtures **l** and **m** respectively.

Each level in ^{188}Pb is a sum of three terms. The spherical 0_1^+ level comprises normal wavefunction $|\mathbf{s}>$ with admixture $\mathbf{a_s}$ and the two intruder wavefunctions corresponding to oblate $|\mathbf{o}>$ (admixture $\mathbf{a_o}$) and prolate $|\mathbf{p}>$ (admixture $\mathbf{a_p}$) shapes. The other two levels are described similarly, as shown in the figure 6.2.

Figure 6.3 illustrates the α-decay transition probabilities for the decay between (a) ^{192}Po and ^{188}Pb and (b) ^{188}Pb and ^{184}Hg. The additional transitions T_5 and T_6 now represent decays involving the third excited state in ^{188}Pb.

6.1.4 Alpha Decay from ^{188}Pb to ^{184}Hg

The possible transitions in the decay of ^{188}Pb to ^{184}Hg are described in figure 6.3 (b). Here, transitions T_2 and T_5 are regarded as two-step processes and can be understood in terms of the particle-hole components of the mother and daughter nuclei as shown in figure 6.4 b). T_2 (the transition amplitude between the 0p-0h component of the

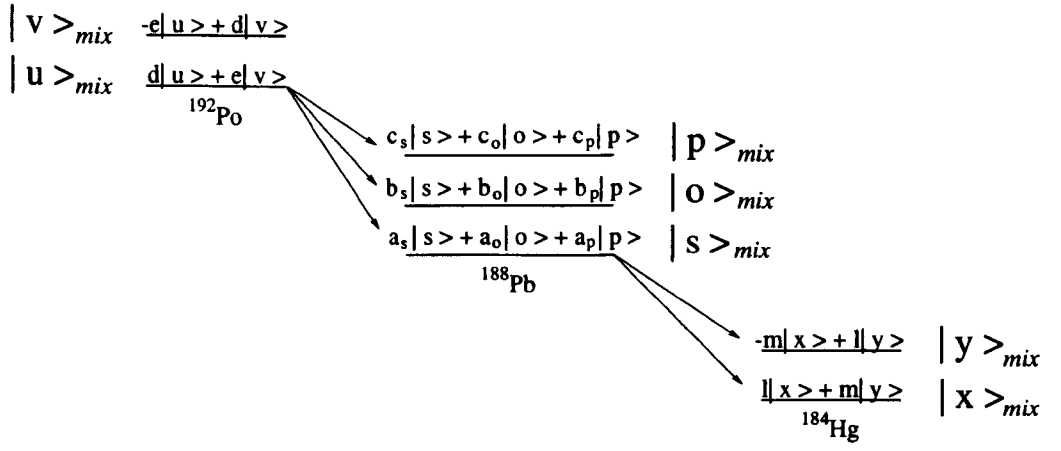

Figure 6.2: Quantum mechanical description of the configuration mixing between the three nuclei of interest.

ground state of ^{188}Pb and the 2p-4h component of the excited 0^+ state in ^{184}Hg) would involve the removal of two protons from below the Z=82 shell gap and the promotion of two protons above the Z=82 shell gap. Similarly, T_5 (the transition amplitude between the 4p-4h component of the excited 0_3^+ prolate state in ^{188}Pb and the 0p-2h component of the ground state) would involve the removal of two protons from above Z=82 and the de-excitation of two protons to below the Z=82 shell gap. In the description of model A (section 1.3.1), T_2 and T_5 would be assumed to equal zero, so in this scenario one would have T_1=T_3=T_4=T_6. However, in the second treatment (model B) involving α decay between 0^+ levels (given by Delion *et al.* [De96]) it is noted that transitions T_1 and T_4 involve the emission of α-particles formed from protons of the Z=82 core, whereas transitions T_3 and T_6 require that the protons are taken from intruder levels above Z=82. Comparing the experimental values for the reduced α-decay widths [Wa93] allows one to estimate that T_1=T_4=$T_3/\sqrt{3}$=$T_6/\sqrt{3}$. The hindrance factor for the α decay of ^{188}Pb to the intruder 0^+ state in ^{184}Hg relative to the decay to the ground state has been measured as 21±3 [Wa94]. This hindrance factor can now be expressed in terms of the transition probabilities and amplitudes of the various configurations for each state as described previously. The 0^+ states in ^{184}Hg can be described as admixtures of the unmixed 0p-2h and 2p-4h configurations,

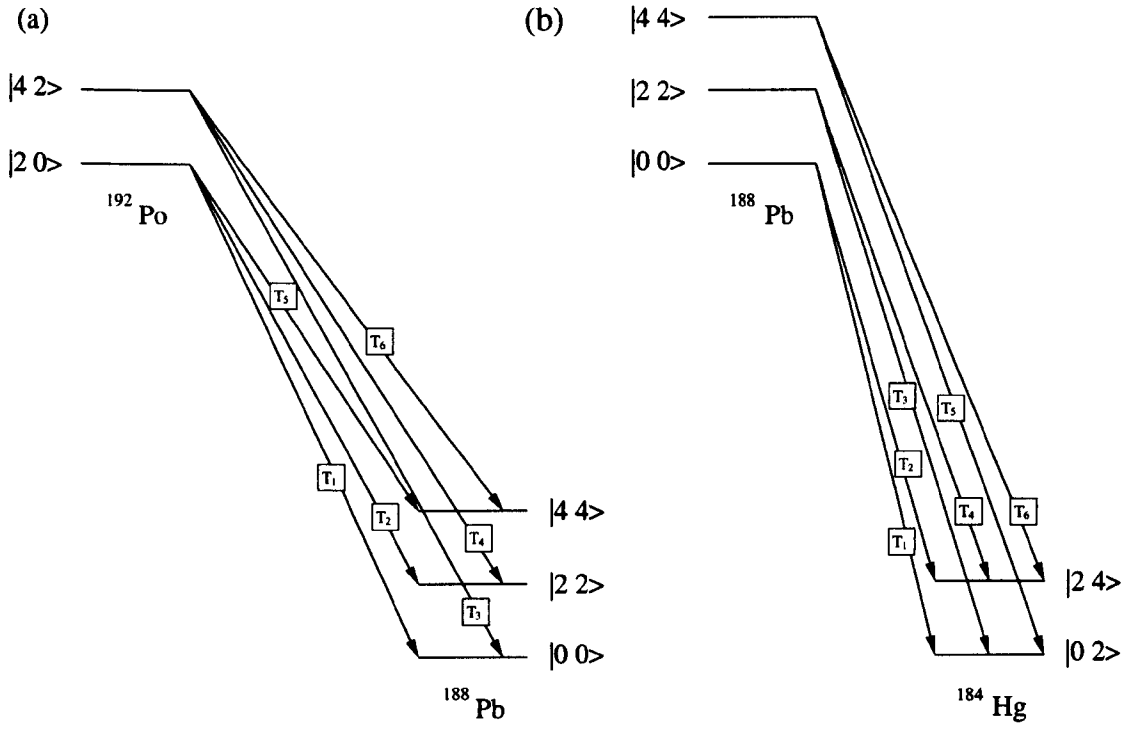

Figure 6.3: Three-level mixing in terms of transition probabilities between (a) ^{192}Po and ^{188}Pb and (b) ^{188}Pb and ^{184}Hg. The states are labelled according to their predominant particle-hole configurations in the absence of mixing.

see figure 6.2. Using a normalization condition [VD90] allows the hindrance factor to be written in terms of the intruder mixing amplitude in the ground state of ^{184}Hg and the mixing amplitudes for the ground state of ^{188}Pb deduced from the 3 level mixing calculation:

$$\mathrm{HF}(^{184}\mathrm{Hg}(0_2^+)) = {}_{mix}\!<\mathbf{s}|\mathbf{x}>_{mix} = \left|\frac{\mathrm{la_sT_1+la_oT_3+la_pT_5+ma_sT_2+ma_oT_4+ma_pT_6}}{\mathrm{-ma_sT_1-ma_oT_3-ma_pT_5+la_sT_2+la_oT_4+la_pT_6}}\right|^2 \qquad (6.2)$$

The resulting admixtures calculated from both model A and model B are 12% and 14% of the intruder configuration in the ground state of ^{184}Hg, respectively. Both of these values are in good agreement with the value of 18% [Bi96] deduced from the hindrance factor measured for ^{184}Hg α decay to 0^+ states in ^{180}Pt [Wa94] and the mixing amplitude extracted from the level scheme of ^{180}Pt [Dr86].

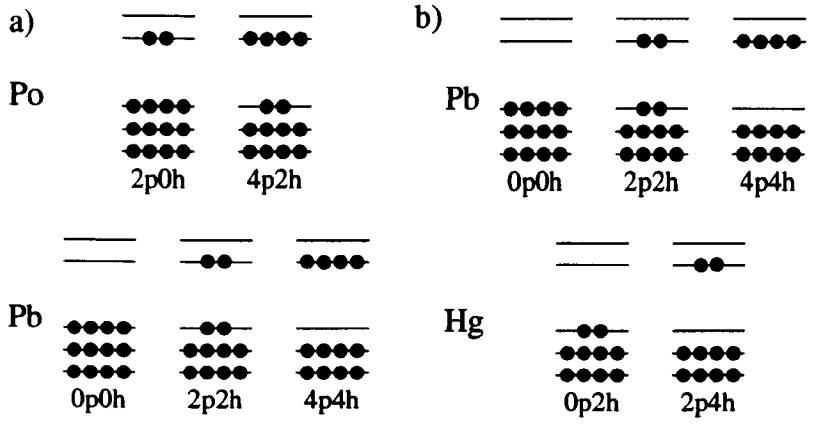

Figure 6.4: Alpha-decay from a) ^{192}Po to ^{188}Pb and b) ^{188}Pb to ^{184}Hg expressed in terms of their corresponding particle-hole components above and below the Z=82 shell closure.

6.1.5 Alpha Decay from ^{192}Po to ^{188}Pb

Here the decay is again represented in terms of the particle-hole components in figure 6.4 a) and transition probabilities in figure 6.3. Transitions T_2 and T_5 once again both involve two-step transitions and are neglected as they would be greatly retarded. Considering the α-decay of the 4p-2h component of the ground state of ^{192}Po to the 0p-0h component of the first excited state in ^{188}Pb (T_3), this process would involve the removal of two protons from above the Z=82 shell gap and the demotion of two protons to below the Z=82 shell gap. Similarly the α decay of the 2p-0h component of the ground state in ^{192}Po to the 4p-4h component of the second excited state in ^{188}Pb (T_5) would involve the removal of two protons from below the Z=82 shell gap and the promotion of two protons above the Z=82 shell gap. All other transitions are allowed, however. Hence, T_3=T_5=0 and T_1=T_2=T_4=T_6 in model A, whereas in the model B, T_3=T_5=0 and T_1=T_4=$T_2\sqrt{3}$=$T_6\sqrt{3}$. The reduced hindrance factors can now be expressed in terms of the transition probabilities and mixing amplitudes of the various configurations for each state, thus:

$$HF(^{188}Pb(0_2^+)) = {}_{mix}\langle \mathbf{u}|\mathbf{o}\rangle_{mix} = \left|\frac{da_sT_1+da_oT_2+da_pT_5+ea_sT_3+ea_oT_4+ea_pT_6}{db_sT_1+db_oT_2+db_pT_5+eb_sT_3+eb_oT_4+eb_pT_6}\right|^2 \qquad (6.3)$$

$$\mathrm{HF}(^{188}\mathrm{Pb}(0_3^+)) = {}_{mix}\!<\mathbf{u}|\mathbf{p}>_{mix} = \left|\frac{da_s T_1 + da_o T_2 + da_p T_5 + ea_s T_3 + ea_o T_4 + ea_p T_6}{dc_s T_1 + dc_o T_2 + dc_p T_5 + ec_s T_3 + ec_o T_4 + ec_p T_6}\right|^2 \qquad (6.4)$$

In the case of the α-decay of ^{192}Po, the ground state of ^{192}Po is assumed to be an admixture of the 'normal' 2p-0h and 'intruder' 4p-2h configurations. The hindrance factors measured for the decays to the two excited 0^+ states can be expressed separately in terms of these transition matrix elements and the mixing amplitudes in both nuclides. For the oblate 2p-2h state, the measured hindrance factor of 0.66±0.12 combined with the extracted mixing amplitudes for ^{188}Pb (section 6.1.3) yields admixtures of 63% and 59% of the intruder 4p-2h configuration in the ground state of ^{192}Po, for models A and B, respectively. This remarkable observation is in agreement with the systematics of reduced α-decay widths of neutron deficient polonium isotopes where the saturation of the ground-state reduced widths has been attributed to an increasing intruder configuration admixture [Wa93] [An97] and with the band structure observed in the in-beam γ-ray spectroscopy of ^{192}Po [Hel96].

Using the hindrance factors already deduced it is possible to estimate the hindrance factor for the α decay to the prolate 0^+ state, by calculating the admixtures of the intruder and normal components in the parent ground state; these values are 0.33±0.09 and 0.53±0.09 for models A and B, respectively (the error bars representing the uncertainties of the level energies through all stages of the the calculation). The measured value of 0.22±0.08 is in good agreement with the former model, but deviates from the supposedly more refined treatment of Delion *et al.* [De96] (model B).

6.2 Second Component of Fine Structure?

An interesting possible explanation for the discrepancy in the reduced hindrance factor is that the prolate fine structure peak may comprise more than one component. In such a scenario the true 0^+ peak intensity would be lower than the value used in the analysis, leading to an increase in the measured hindrance factor.

The width of the prolate α line (FWHM $\sim$ 75keV) is greater than that of the oblate α line (FWHM $\sim$ 38keV) suggesting the presence of more than a single peak, but owing to the lack of counts it is hard to draw a definite conclusion about the possibility of two peaks overlapping. The proximity of the prolate 2^+ level to the 0_3^+ state would make this the obvious candidate for any second component. The identification of the state would rely on the γ decay or conversion electron emission to the prolate or oblate 0^+ state and then conversion electron emission to the ground state. A two peak fit for the α decay to the prolate 0_3^+ state, i.e the upper ring only spectrum of figure 5.9(c), is shown in figure 6.5.

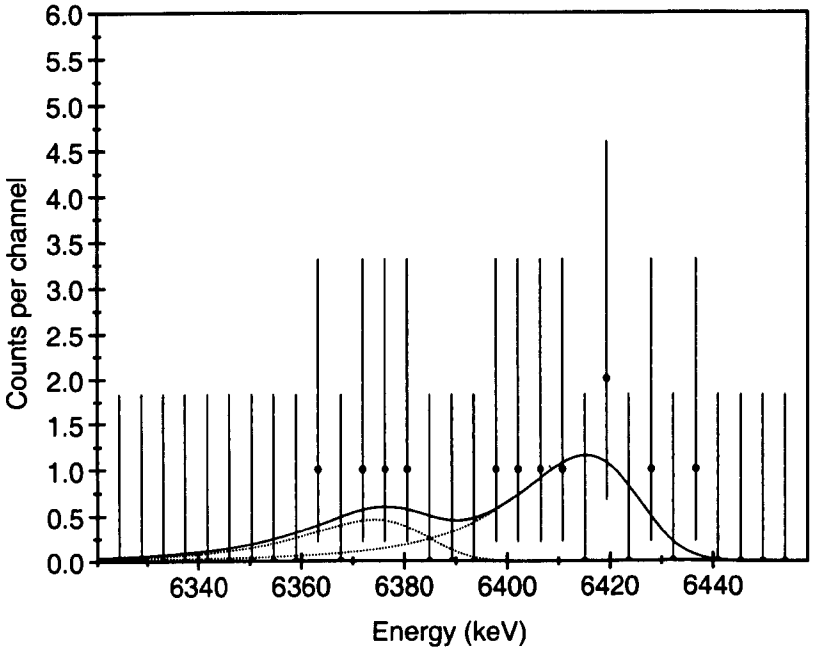

Figure 6.5: Two-peak fit, encompassing the possibility of the prolate assigned peak containing one more component of fine structure.

In this scenario, the energies for the two components would then be 6415$\pm$11 keV for the supposed 2^+ fine structure component and 6374$\pm$8 keV for the prolate 0^+ state. Repeating the band mixing calculations including both components leads to essentially the same conclusions already reached assuming a single component. However,

the fits predict that the component of the 0_3^+ state now contains only two-thirds of the yield of the single peak. Recalculating the hindrance factor increases its value to 0.32 which is in better agreement with the models A and B. A further experiment would be necessary to confirm whether this speculation is really correct.

6.3 Hindrance Factor Trend in the Polonium Isotopes

The calculated hindrance factor for decay to the observed oblate 0^+ state in ^{188}Pb is compared to those in the heavier lead isotopes [Bi95] in table 6.3. The measured value from the present work fits in well with the decreasing trend already observed in the lead isotopes as they become increasingly neutron deficient.

Transition	Excitation energy (keV)	E_α (MeV)	HF
^{198}Po $\rightarrow$ ^{194}Pb	931	5.273	2.8 $\pm$ 0.5
^{196}Po $\rightarrow$ ^{192}Pb	769	5.769	2.5 $\pm$ 0.1
^{194}Po $\rightarrow$ ^{190}Pb	658	6.194	1.1 $\pm$ 0.1
^{192}Po $\rightarrow$ ^{188}Pb	556	6.611	0.7 $\pm$ 0.1

Table 6.3: Calculated hindrance factors for decay to the excited (oblate) states in the lead nuclei. In each case decay from ground-state to ground-state is equal to 1.

The decrease occurs essentially because of a gradually larger admixture of the normal (spherical) state in the intruder levels further from stability. Simultaneously the larger mixing of the intruder level into the ground state of the lighter polonium isotopes further enhances the decay to the intruder levels in the lead nuclei. In the case of ^{188}Pb the value is now less than one indicating that it is now more favourable for the α decay to populate the excited (oblate) 0^+ state than it is the ground state, once the strong energy dependance is removed.

Chapter 7

Conclusion

Alpha-decay transitions have been assigned to excited 0^+ states in ^{188}Pb, identified by conversion electron coincidences in a surrounding array of silicon detectors. The α-decay transition to the lowest-lying level above the ground state is identified as the decay to the oblate 0^+ state, interpreted as a 2p-2h structure analogous to those observed in the heavier even-even lead isotopes. The α-decay transition to the 0^+ level at higher excitation energy is assigned as the α decay to the bandhead of the prolate deformed 4p-4h/6p-6h structure observed in-beam by Heese *et al.* The energies of these states fit in well with the systematics of both the prolate band previously observed in ^{188}Pb and the energies of the 0^+ oblate states in the heavier lead isotopes. The measured half-lives are also consistent with the previously measured ground-state to ground-state value. The nuclide ^{188}Pb is quite remarkable in that three of its four lowest-lying levels have been identified as 0^+ states, all below 1 MeV in excitation energy.

The level scheme has been interpreted in terms of a configuration mixing calculation between the spherical, prolate and oblate bands. Mixing coefficients between the coexisting structures were therefore deduced. The spherical 0p-0h ground state is found to be essentially unmixed, while the excited 0^+ states contain $\sim$20% admixtures of the other configuration. The major component of the ground-state wavefunction has closed shell (0p-0h) configuration implying spherical shape and the persistence of

the Z=82 shell gap for the neutron-deficient lead isotopes.

The degree of mixing in ^{184}Hg and ^{192}Po has been calculated using the mixing amplitudes measured in ^{188}Pb together with the measured α-decay hindrance factors. The results imply that the ground state of ^{192}Po comprises a strong ($\sim$61%) admixture of the 4p-2h intruder configuration and the value for ^{184}Hg ($\sim$13%) compares well with the estimate based on the α decay of ^{184}Hg to ^{180}Pt.

Extending the work in this thesis, it is important to try and establish experimental evidence for the non-yrast states built upon the oblate 0^+ bandhead and also to identify the prolate 2^+ state. This will then provide a stringent test for the results of the band mixing calculations carried out in this work. An experiment has been performed at Jyväskylä during the time of writing this thesis, using an electron spectrometer to select the conversion electron energies of interest in coincidence with in-beam γ rays. The electron could provide a crucial experimental signature that these non-yrast states have been populated. Lifetime and branching ratio measurements of the excited 0^+ levels would also provide an independent estimate of the degree of mixing of the different configurations.

A further experiment to study ^{190}Po using the same technique as described in this thesis is proposed for GSI, Darmstadt.

Appendix A

- **Example MCNP Input File**

```
C
C Lines 30 to 35 inclusive define the six quadrant detectors of the
C array in three-dimensional space.
C Lines 1 to 24 then divide each quadrant detector into its 4 single
C component detectors.
C
C
C Define Cells
C
C Detector elements
C
1 1 -2.3296 -3 1 12 -32 29 -17 imp:e 1 $ Si element 1
2 1 -2.3296 -3 1 32 -10 29 -17 imp:e 1 $ Si element 2
3 1 -2.3296 -3 1 32 -10 16 -29 imp:e 1 $ Si element 3
4 1 -2.3296 -3 1 12 -32 16 -29 imp:e 1 $ Si element 4
5 1 -2.3296 -3 1 9 -31 29 -17 imp:e 1 $ Si element 5
6 1 -2.3296 -3 1 31 -11 29 -17 imp:e 1 $ Si element 6
7 1 -2.3296 -3 1 31 -11 16 -29 imp:e 1 $ Si element 7
8 1 -2.3296 -3 1 9 -31 16 -29 imp:e 1 $ Si element 8
9 1 -2.3296 -2 4 12 -32 29 -17 imp:e 1 $ Si element 9
10 1 -2.3296 -2 4 32 -10 29 -17 imp:e 1 $ Si element 10
11 1 -2.3296 -2 4 32 -10 16 -29 imp:e 1 $ Si element 11
12 1 -2.3296 -2 4 12 -32 16 -29 imp:e 1 $ Si element 12
13 1 -2.3296 -2 4 9 -31 29 -17 imp:e 1 $ Si element 13
```

```
14 1 -2.3296 -2 4 31 -11 29 -17 imp:e 1 $ Si element 14
15 1 -2.3296 -2 4 31 -11 16 -29 imp:e 1 $ Si element 15
16 1 -2.3296 -2 4 9 -31 16 -29 imp:e 1 $ Si element 16
17 1 -2.3296 5 -7 -19 30 29 -17 imp:e 1 $ Si element 17
18 1 -2.3296 5 -7 -30 20 29 -17 imp:e 1 $ Si element 18
19 1 -2.3296 5 -7 -30 20 16 -29 imp:e 1 $ Si element 19
20 1 -2.3296 5 -7 -19 30 16 -29 imp:e 1 $ Si element 20
21 1 -2.3296 -6 8 -19 30 29 -17 imp:e 1 $ Si element 21
22 1 -2.3296 -6 8 -30 20 29 -17 imp:e 1 $ Si element 22
23 1 -2.3296 -6 8 -30 20 16 -29 imp:e 1 $ Si element 23
24 1 -2.3296 -6 8 -19 30 16 -29 imp:e 1 $ Si element 24
30 1 -2.3296 -3 1 14 -21 15 -18 #(-3 1 12 -10 16 -17) imp:e 1 $ element
1
31 1 -2.3296 -3 1 21 -13 15 -18 #(-3 1 9 -11 16 -17) imp:e 1 $ element
2
32 1 -2.3296 -2 4 14 -21 15 -18 #(-2 4 12 -10 16 -17) imp:e 1 $ element
3
33 1 -2.3296 -2 4 21 -13 15 -18 #(-2 4 9 -11 16 -17) imp:e 1 $ element
4
34 1 -2.3296 5 -7 -22 23 15 -18 #(5 -7 -19 20 16 -17) imp:e 1 $ element
5
35 1 -2.3296 -6 8 -22 23 15 -18 #(-6 8 -19 20 16 -17) imp:e 1 $ element
6
C
C Source Cell
C
60 1 -2.3296 -24 25 -26 27 15 -28 imp:e 1 $ si source element
C
C Define world - defines a large area in which the detector array
```

```
C is contained.
C
200 0 200 imp:e 0
201 0 -200 #(-3 1 14 -21 15 -18) #(-3 1 21 -13 15 -18)
             #(-2 4 14 -21 15 -18) #(-2 4 21 -13 15 -18)
             #(5 -7 -22 23 15 -18) #(-6 8 -22 23 15 -18)
             #(-24 25 -26 27 15 -28) imp:e 1
C
C Define Surfaces
C
1 py 2.2
2 py -2.2
3 py 2.246
4 py -2.246
5 px 5.6
6 px -5.6
7 px 5.646
8 px -5.646
9 px 0.1
10 px -0.1
11 px 5.1
12 px -5.1
13 px 5.2
14 px -5.2
15 pz 0
16 pz 0.1
17 pz 5.1
18 pz 5.2
19 py 2.5
```

```
20 py -2.5
21 px 0
22 py 2.6
23 py -2.6
24 px 4.0 $ source cell surfaces
25 px -4.0
26 py 1.75
27 py -1.75
28 pz 0.03 $ depth of source
29 pz 2.6
30 py 0
31 px 2.6
32 px -2.6
200 so 10 $ define world
C
C The next two lines assign MCNP to run in electron mode.
C
mode e
phys:e 1
C
C Source Definition electron
C
C
C A Gaussian source is defined over a single strip of implantation detector.
C The y-distribution is described by the α-decay position spectrum
C for that strip.
C The implantation depth is also calculated from the experimental data.
C
C Average implantation depth = 5.8microns
```

```
C which defines the z co-ordinate below.
C The electron energy is 480 keV
C
C
sdef x=-3.5 y=d1 z=0.029420 ERG=0.484
C
C "si1" is a source information card for the y-distribution d1.
C The "h" following the "si1" tells the card the following information
C should be interpreted as bin boundaries for a histogram distribution.
C
si1 h -1.75 -1.640625 -1.421875 -1.2031250 -0.9843750 -0.7656250
-0.5468750 -0.3281250 -0.1093750 0.1093750 0.3281250
0.5468750 0.7656250 0.9843750 1.2031250 1.421875 1.640625
C
C "sp1" is a source probability card for distribution d1.  The "d"
C defines the following values as probabilities for each bin of
C the distribution.
C
sp1 d 0 0.00014 0.00288 0.03122 0.09322 0.15681 0.19307 0.18242
0.14156 0.09236 0.05697 0.02762 0.0177 0.00374 0.00029 0 0
C
C Tallies 1 kev/channel energy deposition.
C
f18:e 1 22i 24 ( 1 22i 24)
e18 0.00000E+00 0.10000E-02 0.20000E-02 0.30000E-02 0.40000E-02 0.50000E-02
0.60000E-02 0.70000E-02 0.80000E-02 0.90000E-02 0.10000E-01 0.11000E-01
0.12000E-01 0.13000E-01 0.14000E-01 0.15000E-01 0.16000E-01 0.17000E-01
0.18000E-01 0.19000E-01 0.20000E-01 0.21000E-01 0.22000E-01 0.23000E-01
0.24000E-01 0.25000E-01 0.26000E-01 0.27000E-01 0.28000E-01 0.29000E-01
```

0.30000E-01 0.31000E-01 0.32000E-01 0.33000E-01 0.34000E-01 0.35000E-01
0.36000E-01 0.37000E-01 0.38000E-01 0.39000E-01 0.40000E-01 0.41000E-01
0.42000E-01 0.43000E-01 0.44000E-01 0.45000E-01 0.46000E-01 0.47000E-01
0.48000E-01 0.49000E-01 0.50000E-01 0.51000E-01 0.52000E-01 0.53000E-01
0.54000E-01 0.55000E-01 0.56000E-01 0.57000E-01 0.58000E-01 0.59000E-01
0.60000E-01 0.61000E-01 0.62000E-01 0.63000E-01 0.64000E-01 0.65000E-01
0.66000E-01 0.67000E-01 0.68000E-01 0.69000E-01 0.70000E-01 0.71000E-01
0.72000E-01 0.73000E-01 0.74000E-01 0.75000E-01 0.76000E-01 0.77000E-01
0.78000E-01 0.79000E-01 0.80000E-01 0.81000E-01 0.82000E-01 0.83000E-01
0.84000E-01 0.85000E-01 0.86000E-01 0.87000E-01 0.88000E-01 0.89000E-01
0.90000E-01 0.91000E-01 0.92000E-01 0.93000E-01 0.94000E-01 0.95000E-01
0.96000E-01 0.97000E-01 0.98000E-01 0.99000E-01 0.10000E+00 0.10100E+00
0.10200E+00 0.10300E+00 0.10400E+00 0.10500E+00 0.10600E+00 0.10700E+00
0.10800E+00 0.10900E+00 0.11000E+00 0.11100E+00 0.11200E+00 0.11300E+00
0.11400E+00 0.11500E+00 0.11600E+00 0.11700E+00 0.11800E+00 0.11900E+00
0.12000E+00 0.12100E+00 0.12200E+00 0.12300E+00 0.12400E+00 0.12500E+00
0.12600E+00 0.12700E+00 0.12800E+00 0.12900E+00 0.13000E+00 0.13100E+00
0.13200E+00 0.13300E+00 0.13400E+00 0.13500E+00 0.13600E+00 0.13700E+00
0.13800E+00 0.13900E+00 0.14000E+00 0.14100E+00 0.14200E+00 0.14300E+00
0.14400E+00 0.14500E+00 0.14600E+00 0.14700E+00 0.14800E+00 0.14900E+00
0.15000E+00 0.15100E+00 0.15200E+00 0.15300E+00 0.15400E+00 0.15500E+00
0.15600E+00 0.15700E+00 0.15800E+00 0.15900E+00 0.16000E+00 0.16100E+00
0.16200E+00 0.16300E+00 0.16400E+00 0.16500E+00 0.16600E+00 0.16700E+00
0.16800E+00 0.16900E+00 0.17000E+00 0.17100E+00 0.17200E+00 0.17300E+00
0.17400E+00 0.17500E+00 0.17600E+00 0.17700E+00 0.17800E+00 0.17900E+00
0.18000E+00 0.18100E+00 0.18200E+00 0.18300E+00 0.18400E+00 0.18500E+00
0.18600E+00 0.18700E+00 0.18800E+00 0.18900E+00 0.19000E+00 0.19100E+00
0.19200E+00 0.19300E+00 0.19400E+00 0.19500E+00 0.19600E+00 0.19700E+00
0.19800E+00 0.19900E+00 0.20000E+00 0.20100E+00 0.20200E+00 0.20300E+00

0.20400E+00 0.20500E+00 0.20600E+00 0.20700E+00 0.20800E+00 0.20900E+00
0.21000E+00 0.21100E+00 0.21200E+00 0.21300E+00 0.21400E+00 0.21500E+00
0.21600E+00 0.21700E+00 0.21800E+00 0.21900E+00 0.22000E+00 0.22100E+00
0.22200E+00 0.22300E+00 0.22400E+00 0.22500E+00 0.22600E+00 0.22700E+00
0.22800E+00 0.22900E+00 0.23000E+00 0.23100E+00 0.23200E+00 0.23300E+00
0.23400E+00 0.23500E+00 0.23600E+00 0.23700E+00 0.23800E+00 0.23900E+00
0.24000E+00 0.24100E+00 0.24200E+00 0.24300E+00 0.24400E+00 0.24500E+00
0.24600E+00 0.24700E+00 0.24800E+00 0.24900E+00 0.25000E+00 0.25100E+00
0.25200E+00 0.25300E+00 0.25400E+00 0.25500E+00 0.25600E+00 0.25700E+00
0.25800E+00 0.25900E+00 0.26000E+00 0.26100E+00 0.26200E+00 0.26300E+00
0.26400E+00 0.26500E+00 0.26600E+00 0.26700E+00 0.26800E+00 0.26900E+00
0.27000E+00 0.27100E+00 0.27200E+00 0.27300E+00 0.27400E+00 0.27500E+00
0.27600E+00 0.27700E+00 0.27800E+00 0.27900E+00 0.28000E+00 0.28100E+00
0.28200E+00 0.28300E+00 0.28400E+00 0.28500E+00 0.28600E+00 0.28700E+00
0.28800E+00 0.28900E+00 0.29000E+00 0.29100E+00 0.29200E+00 0.29300E+00
0.29400E+00 0.29500E+00 0.29600E+00 0.29700E+00 0.29800E+00 0.29900E+00
0.30000E+00 0.30100E+00 0.30200E+00 0.30300E+00 0.30400E+00 0.30500E+00
0.30600E+00 0.30700E+00 0.30800E+00 0.30900E+00 0.31000E+00 0.31100E+00
0.31200E+00 0.31300E+00 0.31400E+00 0.31500E+00 0.31600E+00 0.31700E+00
0.31800E+00 0.31900E+00 0.32000E+00 0.32100E+00 0.32200E+00 0.32300E+00
0.32400E+00 0.32500E+00 0.32600E+00 0.32700E+00 0.32800E+00 0.32900E+00
0.33000E+00 0.33100E+00 0.33200E+00 0.33300E+00 0.33400E+00 0.33500E+00
0.33600E+00 0.33700E+00 0.33800E+00 0.33900E+00 0.34000E+00 0.34100E+00
0.34200E+00 0.34300E+00 0.34400E+00 0.34500E+00 0.34600E+00 0.34700E+00
0.34800E+00 0.34900E+00 0.35000E+00 0.35100E+00 0.35200E+00 0.35300E+00
0.35400E+00 0.35500E+00 0.35600E+00 0.35700E+00 0.35800E+00 0.35900E+00
0.36000E+00 0.36100E+00 0.36200E+00 0.36300E+00 0.36400E+00 0.36500E+00
0.36600E+00 0.36700E+00 0.36800E+00 0.36900E+00 0.37000E+00 0.37100E+00
0.37200E+00 0.37300E+00 0.37400E+00 0.37500E+00 0.37600E+00 0.37700E+00

0.37800E+00 0.37900E+00 0.38000E+00 0.38100E+00 0.38200E+00 0.38300E+00
0.38400E+00 0.38500E+00 0.38600E+00 0.38700E+00 0.38800E+00 0.38900E+00
0.39000E+00 0.39100E+00 0.39200E+00 0.39300E+00 0.39400E+00 0.39500E+00
0.39600E+00 0.39700E+00 0.39800E+00 0.39900E+00 0.40000E+00 0.40100E+00
0.40200E+00 0.40300E+00 0.40400E+00 0.40500E+00 0.40600E+00 0.40700E+00
0.40800E+00 0.40900E+00 0.41000E+00 0.41100E+00 0.41200E+00 0.41300E+00
0.41400E+00 0.41500E+00 0.41600E+00 0.41700E+00 0.41800E+00 0.41900E+00
0.42000E+00 0.42100E+00 0.42200E+00 0.42300E+00 0.42400E+00 0.42500E+00
0.42600E+00 0.42700E+00 0.42800E+00 0.42900E+00 0.43000E+00 0.43100E+00
0.43200E+00 0.43300E+00 0.43400E+00 0.43500E+00 0.43600E+00 0.43700E+00
0.43800E+00 0.43900E+00 0.44000E+00 0.44100E+00 0.44200E+00 0.44300E+00
0.44400E+00 0.44500E+00 0.44600E+00 0.44700E+00 0.44800E+00 0.44900E+00
0.45000E+00 0.45100E+00 0.45200E+00 0.45300E+00 0.45400E+00 0.45500E+00
0.45600E+00 0.45700E+00 0.45800E+00 0.45900E+00 0.46000E+00 0.46100E+00
0.46200E+00 0.46300E+00 0.46400E+00 0.46500E+00 0.46600E+00 0.46700E+00
0.46800E+00 0.46900E+00 0.47000E+00 0.47100E+00 0.47200E+00 0.47300E+00
0.47400E+00 0.47500E+00 0.47600E+00 0.47700E+00 0.47800E+00 0.47900E+00
0.48000E+00 0.48100E+00 0.48200E+00 0.48300E+00 0.48400E+00 0.48500E+00
0.48600E+00 0.48700E+00 0.48800E+00 0.48900E+00 0.49000E+00 0.49100E+00
0.49200E+00 0.49300E+00 0.49400E+00 0.49500E+00 0.49600E+00 0.49700E+00
0.49800E+00 0.49900E+00 0.50000E+00 0.50100E+00 0.50200E+00 0.50300E+00
0.50400E+00 0.50500E+00 0.50600E+00 0.50700E+00 0.50800E+00 0.50900E+00
0.51000E+00 0.51100E+00 0.51200E+00 0.51300E+00 0.51400E+00 0.51500E+00
0.51600E+00 0.51700E+00 0.51800E+00 0.51900E+00 0.52000E+00 0.52100E+00
0.52200E+00 0.52300E+00 0.52400E+00 0.52500E+00 0.52600E+00 0.52700E+00
0.52800E+00 0.52900E+00 0.53000E+00 0.53100E+00 0.53200E+00 0.53300E+00
0.53400E+00 0.53500E+00 0.53600E+00 0.53700E+00 0.53800E+00 0.53900E+00
0.54000E+00 0.54100E+00 0.54200E+00 0.54300E+00 0.54400E+00 0.54500E+00
0.54600E+00 0.54700E+00 0.54800E+00 0.54900E+00 0.55000E+00 0.55100E+00

0.55200E+00 0.55300E+00 0.55400E+00 0.55500E+00 0.55600E+00 0.55700E+00
0.55800E+00 0.55900E+00 0.56000E+00 0.56100E+00 0.56200E+00 0.56300E+00
0.56400E+00 0.56500E+00 0.56600E+00 0.56700E+00 0.56800E+00 0.56900E+00
0.57000E+00 0.57100E+00 0.57200E+00 0.57300E+00 0.57400E+00 0.57500E+00
0.57600E+00 0.57700E+00 0.57800E+00 0.57900E+00 0.58000E+00 0.58100E+00
0.58200E+00 0.58300E+00 0.58400E+00 0.58500E+00 0.58600E+00 0.58700E+00
0.58800E+00 0.58900E+00 0.59000E+00 0.59100E+00 0.59200E+00 0.59300E+00
0.59400E+00 0.59500E+00 0.59600E+00 0.59700E+00 0.59800E+00 0.59900E+00
0.60000E+00 0.60100E+00 0.60200E+00 0.60300E+00 0.60400E+00 0.60500E+00
0.60600E+00 0.60700E+00 0.60800E+00 0.60900E+00 0.61000E+00 0.61100E+00
0.61200E+00 0.61300E+00 0.61400E+00 0.61500E+00 0.61600E+00 0.61700E+00
0.61800E+00 0.61900E+00 0.62000E+00 0.62100E+00 0.62200E+00 0.62300E+00
0.62400E+00 0.62500E+00 0.62600E+00 0.62700E+00 0.62800E+00 0.62900E+00
0.63000E+00 0.63100E+00 0.63200E+00 0.63300E+00 0.63400E+00 0.63500E+00
0.63600E+00 0.63700E+00 0.63800E+00 0.63900E+00 0.64000E+00 0.64100E+00
0.64200E+00 0.64300E+00 0.64400E+00 0.64500E+00 0.64600E+00 0.64700E+00
0.64800E+00 0.64900E+00 0.65000E+00 0.65100E+00 0.65200E+00 0.65300E+00
0.65400E+00 0.65500E+00 0.65600E+00 0.65700E+00 0.65800E+00 0.65900E+00
0.66000E+00 0.66100E+00 0.66200E+00 0.66300E+00 0.66400E+00 0.66500E+00
0.66600E+00 0.66699E+00 0.66799E+00 0.66899E+00 0.66999E+00 0.67099E+00
0.67199E+00 0.67299E+00 0.67399E+00 0.67499E+00 0.67599E+00 0.67699E+00
0.67799E+00 0.67899E+00 0.67999E+00 0.68099E+00 0.68199E+00 0.68299E+00
0.68399E+00 0.68499E+00 0.68599E+00 0.68699E+00 0.68799E+00 0.68899E+00
0.68999E+00 0.69099E+00 0.69199E+00 0.69299E+00 0.69399E+00 0.69499E+00
0.69599E+00 0.69699E+00 0.69799E+00 0.69899E+00 0.69999E+00 0.70099E+00
0.70199E+00 0.70299E+00 0.70399E+00 0.70499E+00 0.70599E+00 0.70699E+00
0.70799E+00 0.70899E+00 0.70999E+00 0.71099E+00 0.71199E+00 0.71299E+00
0.71399E+00 0.71499E+00 0.71599E+00 0.71699E+00 0.71799E+00 0.71899E+00
0.71999E+00 0.72099E+00 0.72199E+00 0.72299E+00 0.72399E+00 0.72499E+00

```
0.72599E+00 0.72699E+00 0.72799E+00 0.72899E+00 0.72999E+00 0.73099E+00
0.73199E+00 0.73299E+00 0.73399E+00 0.73499E+00 0.73599E+00 0.73699E+00
0.73799E+00 0.73899E+00 0.73999E+00 0.74099E+00 0.74199E+00 0.74299E+00
0.74399E+00 0.74499E+00 0.74599E+00 0.74699E+00 0.74799E+00 0.74899E+00
0.74999E+00 0.75099E+00 0.75199E+00 0.75299E+00 0.75399E+00 0.75499E+00
0.75599E+00 0.75699E+00 0.75799E+00 0.75899E+00 0.75999E+00 0.76099E+00
0.76199E+00 0.76299E+00 0.76399E+00 0.76499E+00 0.76599E+00 0.76699E+00
0.76799E+00 0.76899E+00 0.76999E+00 0.77099E+00 0.77199E+00 0.77299E+00
0.77399E+00 0.77499E+00 0.77599E+00 0.77699E+00 0.77799E+00 0.77899E+00
0.77999E+00 0.78099E+00 0.78199E+00 0.78299E+00 0.78399E+00 0.78499E+00
0.78599E+00 0.78699E+00 0.78799E+00 0.78899E+00 0.78999E+00 0.79099E+00
0.79199E+00 0.79299E+00 0.79399E+00 0.79499E+00 0.79599E+00 0.79699E+00
0.79799E+00 0.79899E+00 0.79999E+00
C
C Define silicon detector with 114 keV resolution.
C
ft18 geb 0.114 0.0 0 $ si-detector
C
C Material Definitions
C
m1 14000 1 $ silicon
C
C Specify 50,000 particle hisories.
C
nps 50000
```

References

[Al98] R.G. Allatt *et al*, accepted for publication in Phys. Lett. B.

[An76] C.G. Andersson *et al*, Nucl. Phys. **A268** 205 (1976).

[And79] R.E. Anderson *et al*, Phys. Rev. C **19** 2138 (1979).

[An97] A.N. Andreyev *et al*, Z. Phys. A. **358** 63 (1997).

[Ba95] J.C. Batcheldor *et al*, Phys. Rev. C **52** 1807 (1995).

[Be69] M.J. Berger *et al*, Nucl. Instrum. Methods Phys. Res., Sect. B **69** 181 (1969).

[Bi95] N. Bijnens *et al*, Physica Scripta. T **56** 110 (1995).

[Bi96] N. Bijnens *et al*, Z Phys. A. **356** 3 (1996).

[BN89] R. Bengtsson and W. Nazarewicz, Z Phys. A. **334** 269 (1989).

[Br92] D.S. Brenner *et al* , Phys. Lett. B **293** 282 (1992).

[Br97] J.F. Briesmeister, Ed., "MCNP - A General Monte Carlo N-Particle Transport Code", version 4B, Los Alamos National Laboratory report, LA-126250-M, 1997.

[BG77] P.J. Brussaard and P.W.M. Glaudemans, "Shell-Model Applications in Nuclear Spectroscopy", North-Holland Publishing Company, Amsterdam, 1977.

[Co85] E. Coenen *et al*, Phys. Rev. Lett. **54** 1783 (1985).

[CF58] B.L. Cohen and C.B. Fulmer, Nucl. Phys. **6** 547 (1958).

[CG28] E.U. Condon and R.W. Gurney, Nature **122** 439 (1928).

[Da92] C.N. Davids *et al*, Nucl. Instrum. Methods Phys. Res., Sect. B **70** 358 (1992).

[Den89] P. Dendooven *et al*, Phys. Lett. **226** 27 (1989).

[De96] D.S. Delion *et al*, Phys. Rev. C **54** 1169 (1996).

[Dr86] G.D. Dracoulis *et al*, J. Phys. G **12** L97 (1986).

[Dr94] G.D. Dracoulis *et al*, Phys. Rev. C **49** 3324 (1994).

[DW78] J. Dudek and T. Werner, J. Phys. G **4** 1543 (1978).

[Fe28] E. Fermi, Z. Phys. **48** 73 (1928).

[Fo97] N. Fotiades *et al*, Phys. Rev. C **55** 1724 (1997).

[Ga28] G. Gamow, Z. Phys. **51** 204 (1928).

[Gh88] A. Ghiorso *et al*, Nucl. Instrum. Methods Phys. Res., Sect. A **269** 192 (1988).

[GN11] H. Geiger and J.M. Nutall, Phil. Mag. **22** 613 (1911).

[He93] J. Heese *et al*, Phys. Lett. B **302** 390 (1993).

[Hel96] K. Helariutta *et al*, Phys. Rev. C **54** R2799 (1996).

[Hey88] K. Heyde *et al*, Nucl. Phys. **A484** 275 (1988).

[Hey94] K. Heyde , "Basic Ideas and Concepts in Nuclear Physics", Institute of Physics Publishing, Bristol and Philadelphia, 1994.

[Heyd94] K. Heyde *et al*, Phys. Rev. C **49** 3329 (1994).

[Ig58] G. J. Igo, Phys. Rev. Lett. **1** 72 (1958).

[Ig70] G. J. Igo *et al*, Phys. Rev. Lett. **24** 470 (1970).

[Ja83] R.V.F Janssens *et al* , Phys. Lett. B **131** 35 (1983).

[Ka95] J.H. Kantele , "Handbook of Nuclear Spectrometry", Academic Press Limited, London, 1995.

[Ke84] J. Kemmer, Nucl. Instrum. Methods Phys. Res., **226** 89 (1984).

[Kn89] G.F. Knoll, "Radiation Detection and Measurement", Second Edition, Wiley (1989).

[Kr88] K.S. Krane, "Introductory Nuclear Physics", Second Edition, Wiley (1988).

[Le81] M. Leino *et al*, Phys. Rev. C **24** 2370 (1981).

[Le95] M. Leino *et al*, Nucl. Instrum. Methods Phys. Res., Sect. B **99** 653 (1995).

[Ma86] W.C. Ma *et al*, Phys. Lett. B **167** 277 (1986).

[Mar69] M.A.J. Mariscotti *et al*, Phys. Rev. **178** 1864 (1969).

[May77] F.R. May *et al*, Phys. Lett. B **68** 113 (1977).

[Me75] S. Meyer, "Data Analysis for Scientists and Engineers", Wiley, NewYork, 1975.

[MN88] P. Möller and J.R. Nix, Atomic Data and Nuclear Data Tables **39** 213 (1988).

[My69] W.D. Myres and W.J. Swiatecki, Ann. Phys. (N.Y) **55** 395 (1969).

[Na89] W. Nazarewicz, G. A. Leander, and A. Johnson, Nucl. Phys. **A503**, 285 (1989).

[Na93] W. Nazarewicz , Phys. Lett. B **305** 195 (1993).

[Ni69] S.G. Nilsson , Nucl. Phys. **A131** 1 (1969).

[NR95] S.G. Nilsson and I. Ragnarsson, "Shapes and Shells in Nuclear Structure", Cambridge University Press, 1995.

[Pa90] R.D. Page , Ph. D. Thesis, University of Birmingham, Unpublished (1990).

[Pe87] J. Peninga *et al*, Nucl. Phys. **A471** 535 (1987).

[Pr62] M.A. Preston, "Physics of the Nucleus", Addison-Wesley Publishing Company, Inc. (1962).

[Ra59] J.O. Rasmussen *et al*, Phys. Rev. **113** 1593 (1959).

[Ro30] S. Rosenblum, J. de Phys. et Rad. **1** 438 (1930).

[RS80] P. Ring and P. Schuck, "The Nuclear Many-body Problem", Springer-Verlag (1980).

[Sc84] K.H. Schmidt *et al*, Z. Phys. A. **316** 19 (1984).

[St67] V.M. Strutinsky, Nucl. Phys. **A95** 420 (1967).

[Ta93] N. Tajima *et al*, Nucl. Phys. **A551** 409 (1993).

[Th27] L.H. Thomas, Proc. Camb. Phil. Soc. **23** 542 (1927).

[VD85] P. Van Duppen *et al*, Phys. Lett. B **154** 354 (1985).

[VD84] P. Van Duppen *et al*, Phys. Rev. Lett. **52** 1974 (1984).

[VD87] P. Van Duppen *et al*, Phys. Rev. C **35** 1861 (1987).

[VD90] P. Van Duppen *et al*, J. Phys. G **16** 441 (1990).

[Wa93] J. Wauters *et al*, Phys. Rev. C **47** 1447 (1993).

[Wa94] J. Wauters *et al*, Phys. Rev. C **50** 2768 (1994).

[Wa97] J. Wauters *et al*, Phys. Rev. C **55** 1192 (1997).

[Wo92] J.L. Wood *et al*, Physics Reports **215** 101 (1992).

[WS54] R.D. Woods and D.S. Saxon , Phys. Rev. **95** 577 (1954).

[Wy89] R. Wyss, J. Nyberg, A. Johnson, R. Bengtsson, and W. Nazarewicz, Phys. Lett. B **215**, 211 (1989).

[Zi85] J.F. Ziegler, J.P. Biersack and U. Littmark, "The Stopping and Ranges of Ions in Matter", Pergamon Press, New York, 1985.